arXiv:2410.09023v2 [cond-mat.stat-mech] 10 Mar 2025

Gyromorphs: a new class of functional disordered materials

Mathias Casiulis,[1,2,*] Aaron Shih,[3,1,*] and Stefano Martiniani[3,1,2,†]

[1] *Center for Soft Matter Research, Department of Physics, New York University, New York 10003, USA*
[2] *Simons Center for Computational Physical Chemistry, Department of Chemistry, New York University, New York 10003, USA*
[3] *Courant Institute of Mathematical Sciences, New York University, New York 10003, USA*

(Dated: March 11, 2025)

We introduce a new class of functional correlated disordered materials, termed Gyromorphs, which uniquely combine liquid-like translational disorder with quasi-long-range rotational order, induced by a ring of G delta peaks in their structure factor. We generate gyromorphs in $2d$ and $3d$ by spectral optimization methods, verifying that they display strong discrete rotational order but no long-range translational order, while maintaining rotational isotropy at short range for sufficiently large G. We show that they are distinct from quasicrystals, which we argue are akin to Fourier "duals" of gyromorphs. Using a coupled dipoles approximation, we show that these structures outperform quasicrystals, stealthy hyperuniformity, and Vogel spirals in the formation of low-index-contrast isotropic bandgaps in $2d$, for both scalar and vector waves, and open complete isotropic bandgaps in $3d$. Finally, we introduce "polygyromorphs" with several rotational symmetries at different length scales (i.e., multiple rings of delta peaks), enabling the formation of multiple bandgaps in a single structure, thereby paving the way for fine control over optical properties.

A crucial aspect of the design and discovery of new materials is understanding the relationship between structure and properties. Crystals have proven to be a highly versatile platform for engineering functions, as the periodicity of their atomic arrangement greatly facilitates the prediction and optimization of their properties. However, not all properties can be realized with periodic structures. Aperiodic media can achieve transport properties unattainable in periodic systems, such as the formation of isotropic photonic bandgaps, which are highly desirable in optoelectronic applications such as freeform waveguides [1, 2] and tunable-reflectance coatings [3]. While isotropic bandgaps have been demonstrated in some deterministic aperiodic systems such as Vogel spirals [4–8], and near-isotropic bandgaps have been observed in quasicrystals [9–11], many recent works have sought this property in correlated disordered structures [12, 13], *i.e.* random point patterns that lack conventional long-range order but exhibit spatial correlations.

Unlike in periodic systems, the structural origins of photonic bandgaps – or more precisely, "pseudogaps", characterized by a depletion in the density of states relative to vacuum, leading to reduced transmission [14, 15] – remain poorly understood in aperiodic systems. Disordered stealthy hyperuniform (SHU) structures [16], which suppress density fluctuations over long distances, have been shown to exhibit isotropic bandgaps in both $2d$ and $3d$ [14, 15, 17–22], but only when strong short-range correlations are also present [14, 15, 17, 23–25]. Further complicating the picture, photonic bandgaps have also been observed in non-SHU disordered structures, such as jammed packings [26–28], and even in systems with only short-range correlations, like equilibrium hard spheres [29], which are not hyperuniform. The role of short range correlations in disordered systems is especially pronounced for vector waves, for which bandgaps have so far only been observed in networked materials, such as honeycomb or tetrahedrally bonded structures [10, 17, 27, 30, 31]. In these random networks, the emergence of bandgaps has been linked to the similarity of local geometry and topology across the network [23, 27, 30].

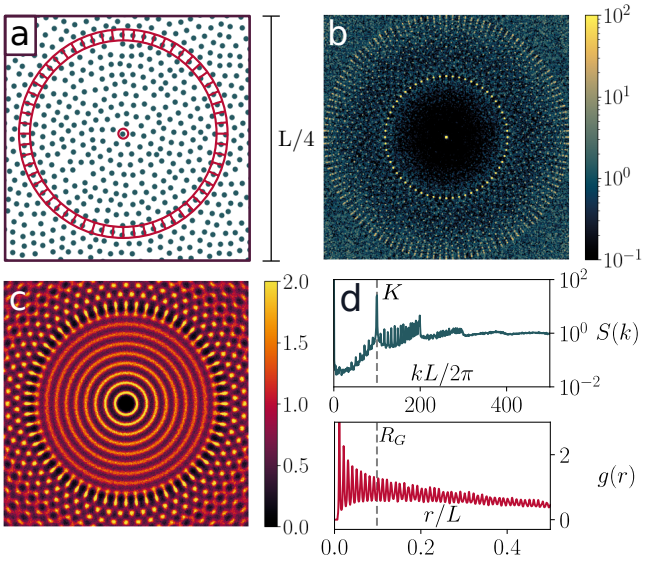


FIG. 1. **Introducing: Gyromorphs.** (a) Section of the point pattern of a 60-fold gyromorph. We show the shortest distance displaying 60-fold order. (b) Corresponding structure factor. (c) Corresponding pair correlation function $g(\boldsymbol{r})$ near the origin. (d) Radial structure factor $S(k)$ (top) and radial distribution function $g(r)$ (bottom) for the 60-fold gyromorph.

This raises the question: is there a unifying feature across these systems that promotes the formation of isotropic photonic bandgaps? In the single-scattering regime, the emergence of a bandgap can be attributed to the presence of strong scattering at some characteristic frequency, and of weaker scattering at neighboring

frequencies. This argument has been invoked to justify the appearance of bandgaps in quasicrystals [11, 32–34], and explains why bandgaps also arise in systems with short-range correlations, such as equilibrium hard sphere liquids [29, 35]. In fact, we observe that all previously cited aperiodic systems that exhibit isotropic bandgaps have an isotropic ring of high values in their structure factor, $S = |\hat{\rho}(\boldsymbol{k})|^2/N$, where $\rho(\boldsymbol{r})$ is the density field defining the system. This condition is also well approximated by quasicrystals, whose most intense structure factor peaks form regular polygons [36, 37].

Bravely adhering to this single-scattering rationale, an ideal bandgap material should exhibit a ring of high values in $S(k)$, contrasting with low values around it. Accordingly, we propose a correlated disordered structure of non-overlapping points whose structure factor displays one ring of $G \in 2\mathbb{N}^\star$ delta peaks with intensities $\mathcal{O}(N)$ on a circle with radius K, but as little order as possible elsewhere. In this work, we show that such hypothetical structures, which we call *gyromorphs*, are realizable, and we present a reliable algorithm for their generation in $2d$ and $3d$.

In gyromorphs, liquid-like isotropic neighborhoods coexist with a ring of extensive $S(k)$ peaks, resulting in quasi-long-range rotational order. These structures are thus fundamentally distinct from any previously known materials, as they reconcile seemingly contradictory features. We successfully generate finite gyromorphs with up to $G \sim 10^3$ peaks, whose heights surpass the peak intensities of finite quasicrystals obtained by usual deterministic methods [38, 39] (see Appendix). Remarkably, we uncover a duality between the structure factor and pair correlation functions of gyromorphs and quasicrystals, suggesting that, at high rotational symmetries, gyromorphs may outperform quasicrystals as bandgap materials. Using a coupled dipoles approximation [40–42], we thus demonstrate that gyromorphs outmatch previous candidate systems in $2d$ as low-index isotropic bandgap materials, for both vector and scalar waves [37]. Finally, we demonstrate that gyromorphs can be extended to $3d$ structures exhibiting *complete* isotropic bandgaps, as well as to "polygyromorphs" with multiple rings of peaks, resulting in multiple bandgaps in a single system.

Generating gyromorphs – To generate gyromorphs, we use the Fast Reciprocal-Space Correlator (FReSCo) [35]. We use the NUwNU (non-uniform real space with non-uniform k-space constraints) variant, which imposes constraints at continuous reciprocal space positions, assuming free boundary conditions for the point pattern. Starting from an initially uncorrelated random point pattern with N points, we optimize it to display G $\mathcal{O}(N)$-high peaks regularly spaced on a ring while forbidding overlaps, thereby creating a G-fold gyromorph (see SM [37]).

Structure of gyromorphs – At high G, although the point pattern appears isotropic at short length scales, gyromorphs still exhibit strong G-fold order at large length

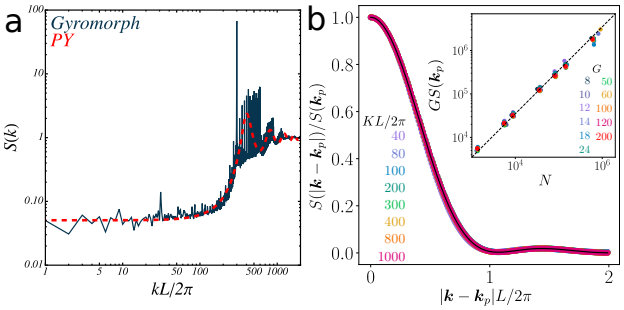


FIG. 2. **Order in gyromorphs.** (a) $S(k)$ of a 60-fold gyromorph (blue) with $N \sim 10^5$ ($KL/2\pi = 300$), compared to a Percus-Yevick $S(k)$ for $\phi = 0.57$ (dashed red line) in log scales. (b) Corresponding radially averaged profile of peaks across K values, rescaled by peak height (colored lines) a solid black line indicates the radial profile of $\mathrm{sinc}^2(k_xL/2)\mathrm{sinc}^2(k_yL/2)$. Inset: Rescaled peak height $GS(\boldsymbol{k}_p)$ against N, in log scales, across G (colored symbols). A dashed black line shows $GS(\boldsymbol{k}_p) = 3.5N$.

scales, as shown in Fig. 1. In Fig. 1(a), we show a portion of an $N \sim 10^4$, $G = 60$ gyromorph, highlighting in red the "gear" with radius $R_G \approx G/K$ [37] onto which 60-fold order is first achieved around an example point. Note that this is different from bond-orientational order [43], which describes nearest-neighbor ordering only; at high G, gyromorphs have no such order, unlike quasicrystals [37]. In Fig. 1(b), we show the corresponding structure factor, highlighting a strong 60-fold ring of peaks, that are intense enough to display a few echoes, and low-intensity regions around the peaks. In Fig. 1(c), we show the central part of the corresponding pair correlation function $g(\boldsymbol{r})$. This function illustrates that each particle is surrounded by the gear of Fig. 1(a), with the same orientation, at the smallest ring of neighbors capable of accommodating G-fold order [37]. Additionally, it reveals that, at shorter distances, the local neighborhoods are perfectly isotropic. The short-range "disorder" is highlighted in Fig. 1(d) by the radial plots of $S(k)$ (top) and $g(r)$ (bottom). While S is peaked at K and shows a few nearby echoes, it eventually decays to 1 at larger k, indicating the absence of short-range order. Similarly, g is notably less peaked than that of (quasi)crystalline structures, exhibiting no visible feature at R_G, and decaying with increasing distance. Overall, Fig. 1 highlights that $S - 1$ is essentially just a G-fold ring of Dirac deltas, so that the $g(r)$ is well approximated by a sum of cosines akin to "kaleidoscopic" optical fields obtained by holographic techniques [44, 45]. In contrast, quasicrystals display rings of peaked g corresponding to a discrete set of allowed neighbor positions [38, 39], so that S is well approximated by a sum of cosines at high G. This "Fourier duality" between gyromorphs and quasicrystals is illustrated in Appendix.

To further investigate the nature of order in gyro-

morphs, we replot a structure factor in log-log scales in Fig. 2(a). This panel shows that gyromorphs are *not* hyperuniform, as the low-k limit of S saturates at a level similar to that of a Percus-Yevick model for equilibrium hard disk liquids [46]. We further validate this observation by measuring local number fluctuations in real space over windows of increasing size [16, 35] (see Appendix), finding that the long-range density fluctuation scaling of gyromorphs is indistinguishable from that of hard disks. Furthermore, at large k, the decay of $S(k)$ is also similar to that of a liquid. These results suggest that, with respect to translational order, gyromorphs are more akin to liquids than to quasicrystals.

In Fig. 2(b), we analyze the peaks. In the main panel, we show the profile of the peak at $(KL/2\pi, 0)$, normalized by its height, as a function of the distance $kL/2\pi$ to the maximum, across system sizes for $G = 60$. As N grows, the profile converges to $\mathrm{sinc}^2(k_xL/2)\mathrm{sinc}^2(k_yL/2)$, implying that the linear width of the peaks in k-space decays like $1/L$. The inset shows that, for different values of G, the peak heights grow like $\mathcal{O}(GN)$, indicating that the peaks are extensive for any fixed order symmetry. Altogether, the peaks have extensive height while their area decays like $1/L^2 \sim 1/N$: they approach Dirac deltas as N increases, like in quasicrystals, so that gyromorphs display quasi-long-range rotational order (see Appendix).

Coupled Dipoles Method – We now turn our attention to the optical properties of gyromorphs. From an Ewald-sphere construction [47, 48] one expects a ring of many high peaks at radius K to generate strong backscattering at $K/2$ [33]. That is why quasicrystals were deemed good candidates for isotropic bandgaps. However, they display increasingly shallow bandgaps as their order of rotational symmetry grows [10], which can be attributed to weakening features in S in de Bruijn's construction [38, 39] as G increases. By contrast, gyromorphs are only constrained to display a finite set of high fine peaks, and they may retain a deep isotropic bandgap even at high G.

To verify this, we assume that each point in the gyromorph represents a non-magnetic scatterer with a dielectric contrast $\delta\varepsilon(\omega) \in \mathbb{C}$ from the surrounding medium at pulsation ω, corresponding to a refractive index $n = \sqrt{1+\delta\varepsilon}$, and a radius a. Limiting our analysis to wavevectors $k_0 = \omega/c$ (with c the celerity of waves in the host medium) such that $k_0 a \ll 1$ (Rayleigh scattering [42]), we employ a coupled dipoles approximation to describe the scattering of waves by the structure. This standard method [40–42] turns the problem of solving Maxwell's equations in the medium (a very strenuous task that involves a full discretization of space as well as very specific choices of boundary conditions [49, 50]) into a linear system, see Appendix. In short, setting only a and n for the scatterers, we measure transmitted intensities for any choice of monochromatic source field, as well as an integrated local density of optical states (LDOS). Throughout the main text, we present results for vector waves

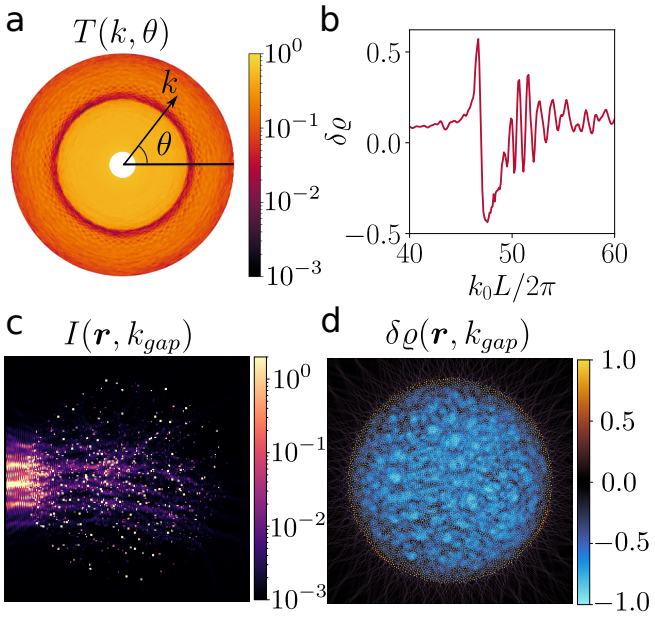


FIG. 3. **Optical properties of gyromorphs** We use an example 60-fold gyromorph and focus on TE polarization. (a) Intensity transmission for frequencies $40 \leq k_0L/2\pi \leq 60$ (radial direction) and 360 incident angles (orthoradial direction) of a source Gaussian beam. (b) Relative LDOS change with respect to vacuum, averaged over 1000 random points, highlighting a dip close to $k_0 = K/2$ (here $KL/2\pi = 100$). (c) Spatial map of the intensity at angle 0 and $k_0L/2\pi = 47.6$, which corresponds to the minimum of both transmission and LDOS. (d) Corresponding LDOS map.

(Transverse Electric, or TE, mode in $2d$, as opposed to the scalar-wave Transverse Magnetic, or TM, mode). We report the scalar-wave results in SM [37], as scalar-wave bandgaps are less challenging to obtain in point patterns [10, 15, 17, 23]. All optical properties are computed within the Materials Analysis via Green's Tensors (MAGreeTe) library, which we make publicly available [51].

Existence of a bandgap – First, in Fig. 3, we focus on a single $2d$ gyromorph with $G = 60$ and $N \sim 10^4$ to determine whether a bandgap is present. We first trim the system to a circular shape of radius $R = L/2$ to avoid any anisotropy due to the overall shape of the medium, like in many experimental tests [9, 17, 18]. We then set the radius a of scatterers such that the filling fraction $\phi \equiv Na^2/R^2$ equals 5% and the dielectric contrast $\delta\varepsilon = 8$ ($n = 3$ for scatterers in vacuum), a typical value for metal oxides used in experiments [22]. Following Refs. [9, 17, 18, 22], we first perform transmission measurements. We set the source to be a standard Gaussian beam with zero curvature focused at the center of the medium [42, 52, 53]. We solve the coupled dipoles system for 360 regularly spaced orientations θ of the beam and for several frequencies k_0. Then, following Refs. [52], we measure the transmitted intensity behind the system at a distance D from its nearest edge [54]. For each in-

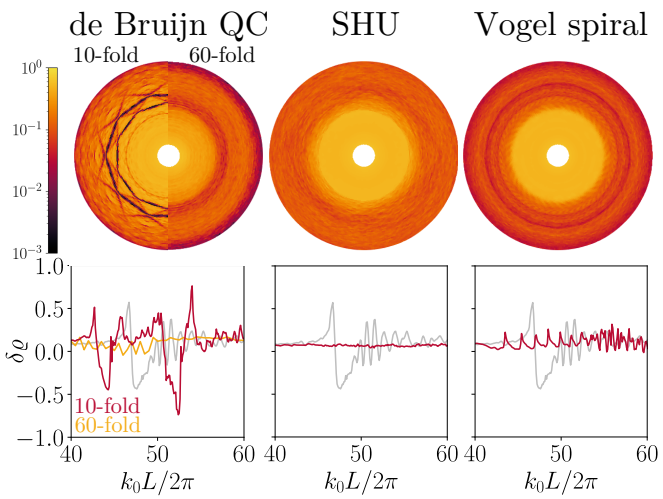


FIG. 4. **Comparison with other systems** Top row: TE intensity transmissions as a function of k_0 (radial) and beam orientation (orthoradial) for (from left to right) 10- and 60-fold de Bruijn quasicrystals, an SHU structure, and a Vogel spiral. Bottom row: Corresponding $\delta\varrho$ (red lines), with the 60-fold gyromorph shown as a light gray line. All results are obtained for $n = 3$, $\phi = 0.05$.

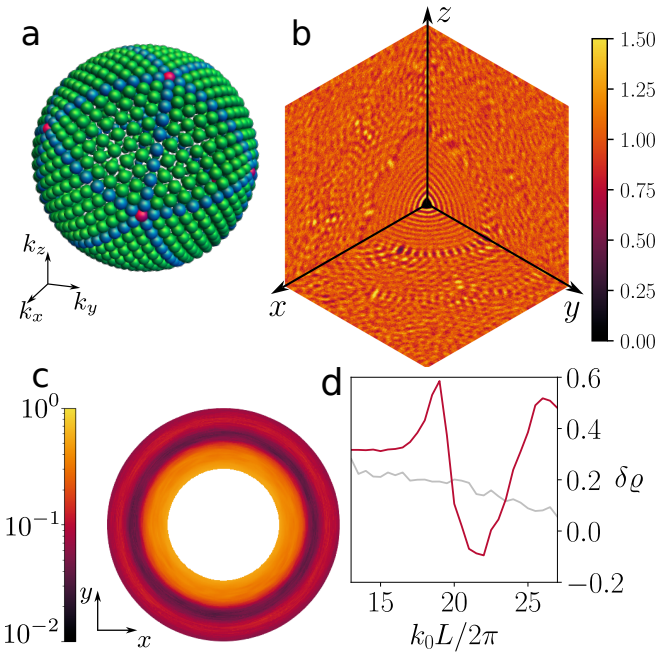


FIG. 5. **Three-dimensional gyromorphs.** (*a*) 3d-rendered orthographic view of the constrained peaks on the sphere. From an icosahedron (red), we subdivide edges (blue) and faces (green) so as to cover the whole sphere uniformly. (*b*) Cross-sections (in the $x = 0$, $y = 0$, and $z = 0$ planes) of the $g(\boldsymbol{r})$ of a gyromorph with $G = 1212$, $N = 83762$. (*c*) Vector-wave transmission averaged over the forward half-sphere, for a beam source rotating in the $z = 0$ plane. (*d*) Relative DOS change for the gyromorph (red line), compared to that of a Poisson point pattern (gray line). In (*c*), (*d*), we use a ball of $N \approx 15000$ points from the structure and set $\phi = 0.1$, $n = 6.5$.

coming beam orientation θ, we define the transmission as the average intensity over 180 angles in $[\theta - \pi/2; \theta + \pi/2]$ on the half-circle with radius D, normalized by the value of the incident field at these points in the absence of the medium. The results, shown in Fig. 3(*a*) in the plane of incident wave-vectors (k_0, θ), display a clear trough of low intensities at $k_{gap} \lesssim K/2$, as expected from single-scattering arguments [33, 35]. An intensity map for $\theta = 0$ and $k_0 = k_{gap}$ is shown in Fig. 3(*c*), confirming that the field is strongly backscattered. To confirm that this lower transmission is the sign of a bandgap, we measure the DOS of the system. In Fig. 3(*b*), we show $\delta\varrho$, the relative change of DOS compared to vacuum averaged over 1000 random points drawn randomly across the material but at least $2a$ away from scatterers, following Refs. [14, 55]. We show strong mode depletion at $k_{gap}L/2\pi = 47.6$. Finally, a map of the local $\delta\varrho$ across the system in Fig. 3(*d*) shows consistent mode depletion across the bulk. We show similar TM results in SM [37].

Comparison to other systems – We compare the results of Fig. 3 to classic bandgap candidates, namely 10- and 60-fold deterministic quasicrystals obtained by the de Bruijn's construction [38, 39, 56], a deterministic Vogel spiral [4], and a random SHU structure generated by FReSCo [35] with a degree of stealthiness such that it displays a TM bandgap [14, 15, 17, 18, 21, 29]. Structures are adjusted to contain $N \sim 10^4$ points and a ring of higher values at the same K as the gyromorphs, and we set all parameters to the same values as in Fig. 3 (see SM [37] for $S(k)$). We report transmission plots in the top row of Fig. 4, and DOS in the bottom row. We show that Vogel and SHU systems display much shallower transmission troughs than the gyromorphs, which we attribute to weaker features in $S(k)$, and very little DOS change. Furthermore, we show that quasicrystals may either display rather deep but anisotropic gaps at low symmetries, or isotropic but shallow gaps at high symmetry due to the broadening of their $S(k)$ features [10, 37]. In fact, the bandgaps of finite-size gyromorphs are as deep as in low-order quasicrystals but more isotropic than them at comparable $\delta\varepsilon$. We check [37] that the DOS dip in gyromorphs gets deeper with index contrast and system size (following a power law, like in defective crystals [57, 58]), but does not strongly depend on G.

Extension to 3d – We now extend the concept of gyromorphs to 3*d* structures. We optimize structures to display G regularly spaced peaks on a sphere with radius K in their structure factor. As there is no standardized way to populate points evenly spaced on a sphere while preserving centrosymmetry, we choose the location of peaks by building upon icosahedral geometry. Starting from an icosahedron of peaks, we subdivide each icosahedral face into multiple triangular faces and project those additional vertices onto the sphere. An example of such

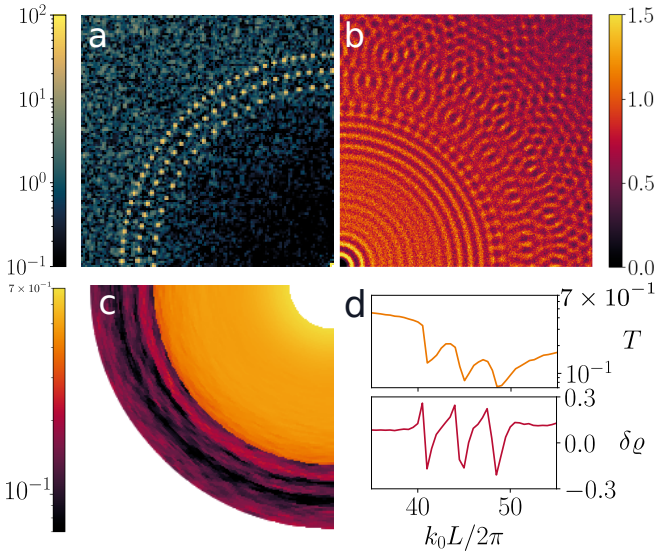


FIG. 6. **Polygyromorphs.** (a) Structure factor featuring 3 rings with 82, 106, and 134 peaks at $KL/2\pi$ equal to 85, 92.5, and 100 respectively. Corresponding (b) $g(\boldsymbol{r})$, (c) TE transmission, and (d) Radially averaged transmission T (top) and LDOS relative change (bottom).

a set of peaks is shown in Fig. 5(a). We show in Fig. 5(b) cross-sections of the $g(\boldsymbol{r})$ for a gyromorph thus obtained with $G \approx 10^3$. Finally, in Fig. 5(c) – (d), we show optical properties measured for this system, namely a transmission plot and the averaged relative change of LDOS for vector waves. We report an isotropic transmission gap, that is correlated to a depletion of DOS, which shows that 3d gyromorphs are promising bandgap formers.

Beyond one ring – Finally, we extend the concept of gyromorphs to disordered systems displaying several rings of peaks in $S(k)$. An example system is shown in Fig. 6, where we impose 3 rings of mutually prime (up to parity) rotational orders, at distances with irrational ratios to ensure that the structure is not trivially compatible with a single (quasi)crystal. The resulting structure factor and pair correlation function are shown in Fig. 6(a) and (b), respectively. This structure is expected to display 3 consecutive dips in transmission and DOS, which we indeed report in Fig. 6(c) and (d). This example highlights that gyromorphs are much more general than "dual quasicrystals" and can be used to obtain arbitrary transmission gaps in an aperiodic medium.

Conclusion – We introduced a novel class of disordered materials, termed gyromorphs, which are translationally disordered but exhibit one (or several) ring of delta peaks, resulting in quasi-long-range discrete rotational order. We showed that gyromorphs with high rotational order exhibit deeper isotropic bandgaps than systems previously considered in the literature, in both 2d and 3d, and that several such features can be imposed at once. This advance is significant both fundamentally and practically. Fundamentally, we conceived and verified the existence of a new class of structures that reconciles seemingly contradictory features and stands apart from all known material types. Practically, our numerical predictions indicate that gyromorphs outperform existing isotropic photonic bandgap materials. Gyromorphs thus show promise for applications such as freeform waveguides [1, 2] and lightweight coatings with strong backscattering, such as highly reflective "white" structures [59, 60].

Acknowledgments – The authors would like to thank Weining Man, Paul Chaikin, Dov Levine, Rémi Carminati, Luís Froufe-Pérez, Frank Scheffold, and Werner Krauth for insightful comments on this work. A.S., M.C., and S.M. acknowledge the Simons Center for Computational Physical Chemistry for financial support. This work was supported in part through the NYU IT High Performance Computing resources, services, and staff expertise. Parts of the results in this work make use of the colormaps in the CMasher package [61]. Correlations are computed using the rusted_core library. The FReSCo, MAGreeTe, and rusted-core libraries are publically available [51, 62, 63].

* Equal contribution.
† sm7683@nyu.edu

[1] W. Man, M. Florescu, E. P. Williamson, Y. He, S. R. Hashemizad, B. Y. Leung, D. R. Liner, S. Torquato, P. M. Chaikin, and P. J. Steinhardt, Isotropic band gaps and freeform waveguides observed in hyperuniform disordered photonic solids, Proceedings of the National Academy of Sciences of the United States of America **110**, 15886 (2013).
[2] M. M. Milošević, W. Man, G. Nahal, P. J. Steinhardt, S. Torquato, P. M. Chaikin, T. Amoah, B. Yu, R. A. Mullen, and M. Florescu, Hyperuniform disordered waveguides and devices for near infrared silicon photonics, Scientific Reports **9**, 20338 (2019).
[3] P. M. Piechulla, E. Slivina, D. Bätzner, I. Fernandez-Corbaton, P. Dhawan, R. B. Wehrspohn, A. N. Sprafke, and C. Rockstuhl, Antireflective Huygens' Metasurface with Correlated Disorder Made from High-Index Disks Implemented into Silicon Heterojunction Solar Cells, ACS Photonics **8**, 3476 (2021).
[4] H. Vogel, A Better Way to Construct the Sunflower Head, Mathematical Biosciences **44**, 179 (1979).
[5] M. E. Pollard and G. J. Parker, Low-contrast bandgaps of a planar parabolic spiral lattice, Optics Letters **34**, 2805 (2009).
[6] S. F. Liew, H. Noh, J. Trevino, L. D. Negro, and H. Cao, Localized photonic band edge modes and orbital angular momenta of light in a golden-angle spiral, Optics InfoBase Conference Papers **19**, 23631 (2012).
[7] J. Trevino, S. F. Liew, H. Noh, H. Cao, and L. Dal Negro, Geometrical structure, multifractal spectra and localized optical modes of aperiodic Vogel spirals, Optics Express **20**, 3015 (2012).
[8] L. A. Razo-López, G. J. Aubry, F. A. Pinheiro, and

F. Mortessagne, Strong localization of microwaves beyond two dimensions in aperiodic Vogel spirals, Physical Review B **109**, 014205 (2024).
[9] W. Man, M. Megens, P. J. Steinhardt, and P. M. Chaikin, Experimental measurement of the photonic properties of icosahedral quasicrystals, Nature **436**, 993 (2005).
[10] M. C. Rechtsman, H. C. Jeong, P. M. Chaikin, S. Torquato, and P. J. Steinhardt, Optimized structures for photonic quasicrystals, Physical Review Letters **101**, 073902 (2008).
[11] Z. V. Vardeny, A. Nahata, and A. Agrawal, Optics of photonic quasicrystals, Nature Photonics **7**, 177 (2013).
[12] S. Yu, C. W. Qiu, Y. Chong, S. Torquato, and N. Park, Engineered disorder in photonics, Nature Reviews Materials **6**, 226 (2021).
[13] K. Vynck, R. Pierrat, R. Carminati, L. S. Froufe-Pérez, F. Scheffold, R. Sapienza, S. Vignolini, and J. J. Sáenz, Light in correlated disordered media, Reviews of Modern Physics **95**, 045003 (2023).
[14] L. S. Froufe-Pérez, M. Engel, J. J. Sáenz, and F. Scheffold, Band gap formation and Anderson localization in disordered photonic materials with structural correlations, Proceedings of the National Academy of Sciences of the United States of America **114**, 9570 (2017).
[15] R. Monsarrat, R. Pierrat, A. Tourin, and A. Goetschy, Pseudogap and Anderson localization of light in correlated disordered media, Physical Review Research **4**, 033246 (2022).
[16] S. Torquato, Hyperuniform states of matter, Physics Reports **745**, 1 (2018).
[17] M. Florescu, S. Torquato, and P. J. Steinhardt, Designer disordered materials with large, complete photonic band gaps, Proceedings of the National Academy of Sciences of the United States of America **106**, 20658 (2009).
[18] W. Man, M. Florescu, K. Matsuyama, P. Yadak, G. Nahal, S. Hashemizad, E. Williamson, P. Steinhardt, S. Torquato, and P. Chaikin, Photonic band gap in isotropic hyperuniform disordered solids with low dielectric contrast, Optics Express **21**, 19972 (2013).
[19] N. Muller, J. Haberko, C. Marichy, and F. Scheffold, Silicon hyperuniform disordered photonic materials with a pronounced gap in the shortwave infrared, Advanced Optical Materials **2**, 115 (2014).
[20] S. Tsitrin, E. P. Williamson, T. Amoah, G. Nahal, H. L. Chan, M. Florescu, and W. Man, Unfolding the band structure of non-crystalline photonic band gap materials, Scientific Reports **5**, 13301 (2015).
[21] M. A. Klatt, P. J. Steinhardt, and S. Torquato, Wave propagation and band tails of two-dimensional disordered systems in the thermodynamic limit, Proceedings of the National Academy of Sciences of the United States of America **119**, e2213633119 (2022).
[22] L. Siedentop, G. Lui, G. Maret, P. M. Chaikin, P. J. Steinhardt, S. Torquato, P. Keim, and M. Florescu, Stealthy and hyperuniform isotropic photonic bandgap structure in 3D, Arxiv Preprint , 2403.08404 (2024), arXiv:2403.08404.
[23] M. Florescu, S. Torquato, and P. J. Steinhardt, Complete band gaps in two-dimensional photonic quasicrystals, Physical Review B - Condensed Matter and Materials Physics **80**, 155112 (2009).
[24] Y. Zheng, L. Liu, H. Nan, Z. X. Shen, G. Zhang, D. Chen, L. He, W. Xu, M. Chen, Y. Jiao, and H. Zhuang, Disordered hyperuniformity in two-dimensional amorphous silica, Science Advances **6**, eaba0826 (2020).
[25] L. S. Froufe-Pérez, G. J. Aubry, F. Scheffold, and S. Magkiriadou, Bandgap fluctuations and robustness in two-dimensional hyperuniform dielectric materials, Optics Express **31**, 18509 (2023).
[26] J. K. Yang, C. Schreck, H. Noh, S. F. Liew, M. I. Guy, C. S. O'Hern, and H. Cao, Photonic-band-gap effects in two-dimensional polycrystalline and amorphous structures, Physical Review A - Atomic, Molecular, and Optical Physics **82**, 053838 (2010).
[27] S. F. Liew, J. K. Yang, H. Noh, C. F. Schreck, E. R. Dufresne, C. S. O'Hern, and H. Cao, Photonic band gaps in three-dimensional network structures with short-range order, Physical Review A - Atomic, Molecular, and Optical Physics **84**, 063818 (2011).
[28] K. Djeghdi, U. Steiner, and B. D. Wilts, 3D Tomographic Analysis of the Order-Disorder Interplay in the Pachyrhynchus congestus mirabilis Weevil, Advanced Science **9**, 2202145 (2022).
[29] L. S. Froufe-Pérez, M. Engel, P. F. Damasceno, N. Muller, J. Haberko, S. C. Glotzer, and F. Scheffold, Role of Short-Range Order and Hyperuniformity in the Formation of Band Gaps in Disordered Photonic Materials, Physical Review Letters **117**, 1 (2016).
[30] S. R. Sellers, W. Man, S. Sahba, and M. Florescu, Local self-uniformity in photonic networks, Nature Communications **8**, 14439 (2017).
[31] M. A. Klatt, P. J. Steinhardt, and S. Torquato, Phoamtonic designs yield sizeable 3D photonic band gaps, Proceedings of the National Academy of Sciences of the United States of America **116**, 23480 (2019).
[32] Y. S. Chan, C. T. Chan, and Z. Y. Liu, Photonic band gaps in two dimensional photonic quasicrystals, Physical Review Letters **80**, 956 (1998).
[33] P. L. Hagelstein and D. R. Denison, Nearly isotropic photonic bandgap structures in two dimensions, Optics Letters **24**, 708 (1999).
[34] A. Della Villa, S. Enoch, G. Tayeb, V. Pierro, V. Galdi, and F. Capolino, Band gap formation and multiple scattering in photonic quasicrystals with a penrose-type lattice, Physical Review Letters **94**, 183903 (2005).
[35] A. Shih, M. Casiulis, and S. Martiniani, Fast Generation of Spectrally-Shaped Disorder, Physical Review E **110**, 034122 (2024).
[36] D. Levine and P. J. Steinhardt, Quasicrystals: A new class of ordered structures, Physical Review Letters **53**, 2477 (1984).
[37] See Supplemental Material at `URL_will_be_inserted_by_publisher` for a comparison between structure factors of known bandgap formers and gyromorphs, detailed numerical methods including a characterization of the nature and variety of structures reached by our algorithm, measurements of the effect of random kicks on gyromorphs, further discussions about the differences between gyromorphs and quasicrystals, a brief description of the sum of cosine function that approximates $g(r)$, a reminder of the derivation of relevant quantities and equations within the coupled dipoles method, additional scalings for the bandgap quality against physical parameters, the equivalent of the main text results for $2d$ and $3d$ scalar waves, and a short comparison between coupled dipoles and finite-difference methods.
[38] N. De Bruijn, Algebraic theory of Penrose's non-periodic tilings of the plane . I , II : dedicated to G. Pólya, Inda-

gationes Mathematicae **43**, 39 (1981).
[39] N. de Bruijn, Quasicrystals and their Fourier transform, Indagationes Mathematicae (Proceedings) **89**, 123 (1986).
[40] M. Lax, Multiple Scattering of Waves, Reviews of Modern Physics **23**, 287 (1951).
[41] M. Lax, Multiple scattering of waves. II. the effective field in dense systems, Physical Review **85**, 621 (1952).
[42] R. Carminati and J. C. Schotland, *Principles of Scattering and Transport of Light* (Cambridge University Press, 2021).
[43] P. J. Steinhardt, D. R. Nelson, and M. Ronchetti, Bond-orientational order in liquids and glasses, Physical Review B **28**, 784 (1983).
[44] Y. F. Chen, H. C. Liang, Y. C. Lin, Y. S. Tzeng, K. W. Su, and K. F. Huang, Generation of optical crystals and quasicrystal beams : Kaleidoscopic patterns and phase singularity, Physical Review A **83**, 053813 (2011).
[45] P.-H. Tuan and L.-Q. Huang, Optical vector fields with kaleidoscopic quasicrystal structures by multiple beam interference, Optics Express **31**, 33077 (2023).
[46] Y. Rosenfeld, Free-energy model for the inhomogeneous hard-sphere fluid in D dimensions: Structure factors for the hard-disk (D=2) mixtures in simple explicit form, Physical Review A **42**, 5978 (1990).
[47] P. P. Ewald, Die Berechnung optischer und elektrostatischer Gitterpotentiale, Annalen der Physik **369**, 253 (1921).
[48] C. Kittel, *Introduction to Solid-state Physics* (John Wiley & Sons, New York, 1953).
[49] A. F. Oskooi, D. Roundy, M. Ibanescu, P. Bermel, J. D. Joannopoulos, and S. G. Johnson, Meep: A flexible free-software package for electromagnetic simulations by the FDTD method, Computer Physics Communications **181**, 687 (2010).
[50] A. Yamilov, S. E. Skipetrov, T. W. Hughes, M. Minkov, Z. Yu, and H. Cao, Anderson localization of electromagnetic waves in three dimensions, Nature Physics **19**, 1308 (2023).
[51] M. Casiulis, A. Shih, and S. Martiniani, Materials Analysis via Greene Tensors (MAGreeTe) (2024).
[52] O. Leseur, R. Pierrat, J. J. Sáenz, and R. Carminati, Probing two-dimensional Anderson localization without statistics, Physical Review A - Atomic, Molecular, and Optical Physics **90**, 053827 (2014).
[53] O. Leseur, R. Pierrat, and R. Carminati, High-density hyperuniform materials can be transparent, Optica **3**, 763 (2016).
[54] The reason for not measuring the transmission in the far field is that the monochromatic Gaussian beam is not in fact a physical laser beam, in the sense that its intensity does not decay according to the Rayleigh-Sommerfeld boundary condition in the far field [42].
[55] R. Pierrat and R. Carminati, Spontaneous decay rate of a dipole emitter in a strongly scattering disordered environment, Physical Review A - Atomic, Molecular, and Optical Physics **81**, 063802 (2010).
[56] V. H. Lutfalla, An effective construction for cut-and-project rhombus tilings with global n-fold rotational symmetry, in *27th IFIP WG 1.5 International Workshop on Cellular Automata and Discrete Complex Systems (AUTOMATA 2021)*, 9, edited by A. Castillo-Ramirez, P. Guillon, and K. Perrot (Schloss Dagstuhl – Leibniz-Zentrum für Informatik, Dagstuhl Publishing, Germany, 2021) pp. 9:1–9:12.
[57] S. E. Skipetrov, Finite-size scaling analysis of localization transition for scalar waves in a three-dimensional ensemble of resonant point scatterers, Physical Review B **94**, 064202 (2016).
[58] S. E. Skipetrov, Finite-size scaling of the density of states inside band gaps of ideal and disordered photonic crystals, European Physical Journal B **93**, 70 (2020).
[59] M. Burresi, L. Cortese, L. Pattelli, M. Kolle, P. Vukusic, D. S. Wiersma, U. Steiner, and S. Vignolini, Bright-white beetle scales optimise multiple scattering of light, Scientific Reports **4**, 1 (2014).
[60] B. D. Wilts, X. Sheng, M. Holler, A. Diaz, M. Guizar-Sicairos, J. Raabe, R. Hoppe, S. H. Liu, R. Langford, O. D. Onelli, D. Chen, S. Torquato, U. Steiner, C. G. Schroer, S. Vignolini, and A. Sepe, Evolutionary-Optimized Photonic Network Structure in White Beetle Wing Scales, Advanced Materials **30**, 201702057 (2018).
[61] E. van der Velden, CMasher: Scientific colormaps for making accessible, informative and 'cmashing' plots, Journal of Open Source Software **5**, 2004 (2020).
[62] A. Shih, M. Casiulis, and S. Martiniani, Fast Reciprocal-Space Correlator (FReSCo) (2023).
[63] M. Casiulis, rusted_core (2023).
[64] A. Pilleboue, G. Singh, D. Coeurjolly, M. Kazhdan, and V. Ostromoukhov, Variance analysis for Monte Carlo integration, ACM Transactions on Graphics **34**, 124 (2015).
[65] E. P. Bernard, W. Krauth, and D. B. Wilson, Event-chain Monte Carlo algorithms for hard-sphere systems, Physical Review E - Statistical, Nonlinear, and Soft Matter Physics **80**, 5 (2009).
[66] A. Cazé, R. Pierrat, and R. Carminati, Strong coupling to two-dimensional Anderson localized modes, Physical Review Letters **111**, 053901 (2013).

Gyromorphs are not hyperuniform– In the main text, we claim that gyromorphs are not hyperuniform based on results presented in Figs. 1 and 2. We present further

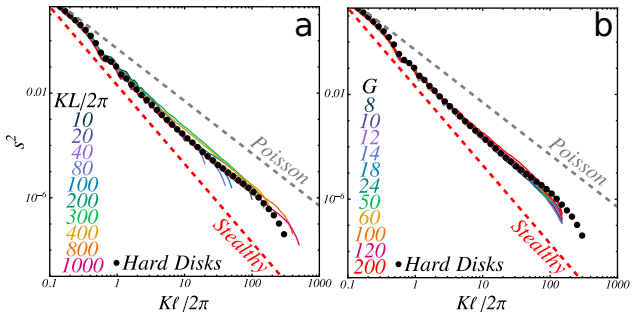


FIG. A1. **Gyromorphs are not hyperuniform.** (*a*) Reduced number variance from randomly drawn disks with radii ℓ in 60-fold gyromorphs with various $KL/2\pi$ from 10 to 1000 (solid colored lines), against $K\ell/2\pi$, in log-log scale. A dashed gray line indicates Poisson scaling, $s^2 \sim \ell^{-d}$, and a dashed red line the stealthy scaling $s^2 \sim \ell^{-d-1}$. Black disks indicate data from equilibrium hard disks with a $\phi = 0.6$ filling fraction, for which the x axis has been rescaled using the location of the first peak as a K value. (*b*) Similar plot but varying the order of rotational symmetry G for $KL/2\pi$.

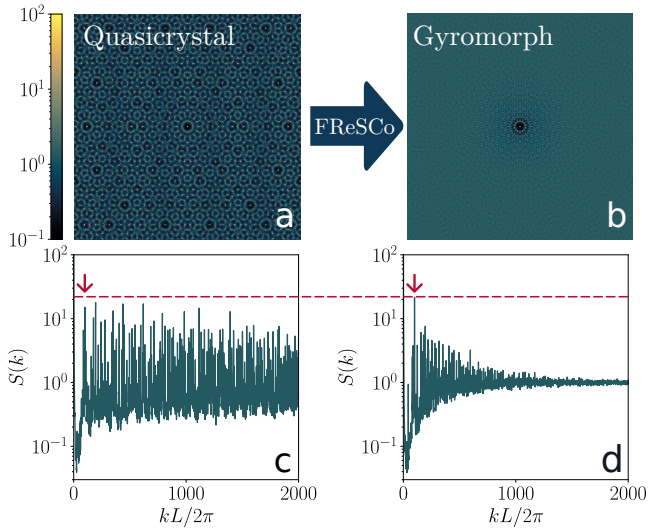


FIG. A2. **Gyromorph generated from a Quasicrystal.** $2d$ structure factors of (a) a 14-fold quasicrystal and (b) a 14-fold gyromorph generated using the quasicrystal as an initial condition. $(c), (d)$ depict radial structure factors of the quasicrystal and gyromorph respectively.

evidence of this in Fig. A1, where we perform discrepancy measurements for disks [16, 35, 64]. To do so, we draw random disks with radius ℓ at uniform positions within 60-fold gyromorphs and count the number of points that each disk contains. We then measure the mean number μ and the variance σ^2 of this number using $10,000$ disks, and compute the reduced variance $s^2 \equiv \sigma^2/\mu^2$ for each ℓ. The output is shown when varying K for $G = 60$ in Fig. A1(a), where s^2 is plotted against $K\ell/2\pi$ in logarithmic scales. We show that gyromorphs display number fluctuations close to Poissonian ($s^2 \sim \ell^{-d}$) at small length scales, then feature sub-Poissonian fluctuations at ranges larger than $1/K$. While the behaviour is non-Poissonian, the slope is much weaker than that of stealthy hyperuniform systems ($s^2 \sim \ell^{-d-1}$). In fact, we show that gyromorphs are near-indistinguishable from equilibrium hard disk liquids, using data from an $N \sim 10^5$ equilibrium configuration obtained by Event-Chain Monte Carlo [65]. This conclusively shows that gyromorphs are *not* hyperuniform, even in the largest systems we test, $N \sim 10^6$. We show in Fig. A1(b) that this result holds when scanning values of G at a fixed K, even at rotational symmetries of order as low as 8-fold, where gyromorphs may more easily be confused [35] with quasicrystals (which follow the stealthy scaling [16]).

Gyromorphs and Quasicrystals – Here, we further discuss the differences and commonalities between gyromorphs and quasicrystals. First, we produce a 14-fold quasicrystal by de Bruijn's method [38, 39], and report its $S(k)$ in Fig. A2$(a), (c)$, respectively as an intensity map in k-space and as a radially-averaged function of k. The structure factor is patterned up to very large k, resulting in peaks with near-constant (but slowly decaying) intensity in the radial plot. We use this structure as an initial condition for our algorithm, aiming to enhance the height of the existing first ring of high quasicrystalline peaks (indicated by the arrow in Fig. A2(b)). The result, whose $S(k)$ is shown in Fig. A2$(b), (d)$ is indistinguishable from what we obtain from random initial conditions. In particular, note that the large-k structure in S is completely destroyed: the far-away pattern has been "pumped" into the peaks to make them (about 3 times) higher, as highlighted by a red dashed line. This experiment shows that gyromorphs, the minima of our loss function, are not simply noisy quasicrystals but do in fact display stronger peaks even at small G. Furthermore, gyromorphs are not simply entropically more favorable than quasicrystals, they actually better minimize our loss function.

This difference becomes starker at larger orders of rotational symmetry, as the height of the $S(k)$ peaks of de Bruijn quasicrystals decays fast with G [10]. However, we highlight an interesting link between gyromorphs and quasicrystals in Fig. A3, where we show side-by-side comparisons of these two quantities for $G = 100$ in panels Fig. A3(a),(c), and $G = 14$ in panels Fig. A3(b),(d). All systems were made using $N \approx 10^4$ points. The quasicrystals are constructed using de Bruijn's multigrid and dual method [38, 39, 56]. The panels show near-perfect agreement between the real (resp. reciprocal) features of gyromorphs and the reciprocal (resp. real) features of quasicrystals. In other words, gyromorphs look like duals

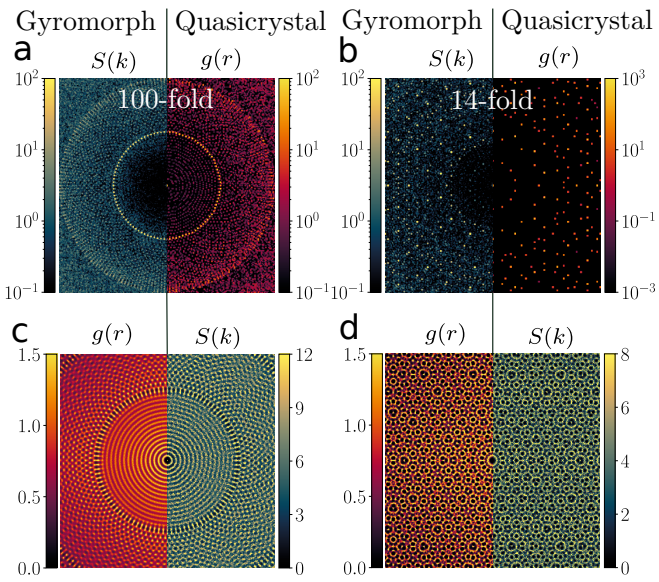


FIG. A3. **Gyromorphs as duals of Quasicrystals.** Comparisons between the $S(k)$ (resp. $g(r)$) of $2d$ gyromorphs and the $g(r)$ (resp. $S(k)$) of quasicrystals for $(a), (c)$ $G = 100$ and $(b), (d)$ $G = 14$. The plot ranges and intensity scales are adjusted to match images.

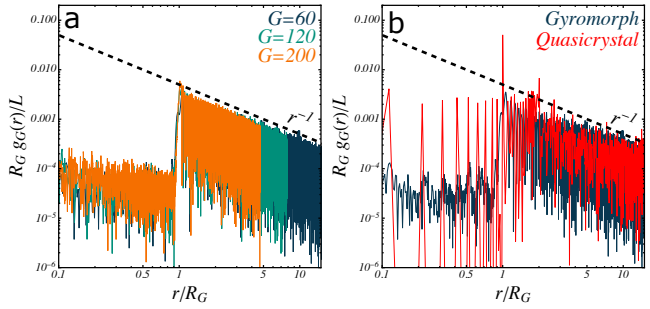


FIG. A4. **Rotational order in gyromorphs.** Gyromorphic correlation function g_G, rescaled by R_G/L, against r/R_G, for $G = 60$ (dark blue), $G = 120$ (green), $G = 200$ (orange). A dashed black line shows a r^{-1} power law as a guide for the eye. Here, $KL/2\pi = 300$.

of quasicrystals. This is because the $S(k)$ of gyromorphs (resp. the $g(r)$ of quasicrystals) is dominated by one ring of high peaks, so that its Fourier transform is well approximated by a sum of cosines – although $g(r) = 0$ at short range in gyromorphs by design.

To highlight that gyromorphs display quasi-long-range rotational order, in Fig. A4(a), we plot a gyromorphic correlation function, g_G, defined as

$$g_G(r) \equiv \left| \frac{L^d}{N^2} \frac{1}{2\pi} \sum_{p \neq q} e^{iG\theta_{pq}} \delta(r - r_{pq}) \right|, \qquad \text{(A1)}$$

where the sum runs over all pairs of particles, that are separated by a distance vector $\boldsymbol{r}_{pq}$ with polar components (r_{pq}, θ_{pq}). That is essentially the value of the modulus of the G-th Fourier mode of a shell of $g(r)$ at distance r. When suitably rescaled by R_G, this function collapses across values of G, and displays a power-law decay with an exponent close to -1. We show in Fig. A4(b) a comparison of that function between a $G = 60$ gyromorph and the corresponding quasicrystal, with R_G taken as the location of the strongest peak. The difference is mainly that quasicrystals display strong rotational order with nearest neighbors, as they lie on a discrete set of orientations along a rhombic tiling, while gyromorphs are isotropic at short range. The long-range behavior, however, is nearly the same. Thus, gyromorphs display quasi-long-range rotational order, that extends throughout the system [35, 37].

Coupled dipoles in a nutshell – If $\boldsymbol{r}_i$ represents the position of scatterer i, $\boldsymbol{E}_{inc}(\boldsymbol{r}_i;\omega)$ is the ω-component of the Fourier representation of an arbitrary incident field at $\boldsymbol{r}_i$ and $\boldsymbol{E}(\boldsymbol{r}_i;\omega)$ is the total exciting field at scatterer i, this system can be written as

$$\mathcal{M}(\{\boldsymbol{r}_{ij}\};\omega) \cdot \mathcal{E}(\{\boldsymbol{r}_j\};\omega) = \mathcal{E}_{inc}(\{\boldsymbol{r}_i\};\omega), \qquad \text{(A2)}$$

where we introduced rank-2 tensor notations for the values of both kinds of fields so that for instance $\mathcal{E}_{i,a} = \boldsymbol{E}(\boldsymbol{r}_i;\omega) \cdot \hat{\boldsymbol{e}}_a$ with $a \in \{x, y, z\}$, and $\mathcal{M}(\{\boldsymbol{r}_{ij}\};\omega)$ is rank-4 with elements

$$\mathcal{M}_{ijab} = \begin{cases} \delta_{ab}(1 - k_0^2 \alpha(\omega)\Sigma) & \text{if } i = j \\ -k_0^2 \alpha(\omega) \hat{\boldsymbol{e}}_a \cdot \overline{\overline{G}}_0(\boldsymbol{r_i}, \boldsymbol{r}_j;\omega) \cdot \hat{\boldsymbol{e}}_b & \text{otherwise.} \end{cases} \qquad \text{(A3)}$$

In this last expression, $\alpha(\omega) \equiv V\delta\varepsilon$ is the polarizability of a scatterer with volume V, Σ is a self-interaction term that ensures energy conservation and $\overline{\overline{G}}_0$ is the Green tensor of free propagation with the desired boundary conditions (here, Rayleigh-Sommerfeld ones [42]). Solving Eq. 2 for vector waves with p components reduces to a $pN \times pN$ linear solve yielding $\mathcal{E} = \mathcal{W} \cdot \mathcal{E}_{inc}$ where $\mathcal{W} = \mathcal{M}^{-1}$. From that solution, the full electromagnetic field at any position $\boldsymbol{r}$ outside of scatterers can be reconstructed as

$$\boldsymbol{E}(\boldsymbol{r};\omega) = \boldsymbol{E}_{inc}(\boldsymbol{r};\omega) + k_0^2 \alpha(\omega) \mathcal{G}_0(\boldsymbol{r}, \{\boldsymbol{r}_i\};\omega) \cdot \mathcal{E}(\{\boldsymbol{r}_i\};\omega), \qquad \text{(A4)}$$

where $\mathcal{G}_0$ is a rank-3 tensor with elements $\mathcal{G}_{0,iab} = \hat{\boldsymbol{e}}_a \cdot \overline{\overline{G}}_0(\boldsymbol{r}, \boldsymbol{r}_i;\omega) \cdot \hat{\boldsymbol{e}}_b$. In practice, we use

$$\boldsymbol{E}_{inc}(\boldsymbol{r};\omega) \equiv \boldsymbol{E}_0 \exp\left[-i\boldsymbol{k}_0 \cdot \boldsymbol{r}_{\parallel} - \frac{r_{\perp}^2}{w^2} \right], \qquad \text{(A5)}$$

with $\boldsymbol{r}_{\parallel}, \boldsymbol{r}_{\perp}$ the components of $\boldsymbol{r}$ parallel and perpendicular to a beam with width $w = L/5$, respectively. Finally, to assert the presence of bandgaps, we compute the local density of optical states (LDOS)

$$\varrho(\boldsymbol{r};\omega) \equiv \frac{2\omega}{\pi c^2} \mathrm{Im}\mathrm{Tr}_p \overline{\overline{G}}(\boldsymbol{r}, \boldsymbol{r};\omega). \qquad \text{(A6)}$$

The coupled dipoles method lets us compute the relative change of LDOS compared to the vacuum value, $\delta\varrho = \varrho/\varrho_0 - 1$, as the trace of a tensor product.

$$\delta\varrho(\boldsymbol{r};\omega) = C_p \mathrm{Im}\left[\alpha \mathrm{Tr}_p \left[\mathcal{G}_0(\boldsymbol{r};\{\boldsymbol{r}_i\}) \cdot \mathcal{W} \cdot {}^t\mathcal{G}_0(\boldsymbol{r};\{\boldsymbol{r}_j\}) \right] \right], \qquad \text{(A7)}$$

where we dropped the ω dependence from the tensor notations for compactness and $C_p = (2\omega^3)/[\pi c^4 \varrho_0(\omega)]$. Following past works [14, 55, 66], we estimate the DOS of the medium at points at least $2a$ away from scatterer centers, and average the result over random points in the medium. We remind the standard [42] derivation of these equations and the precise definitions of every term in $2d$ and $3d$ in SM [37].

arXiv:2410.09023v2 [cond-mat.stat-mech] 10 Mar 2025

Supplementary Material for: "Gyromorphs: a new class of disordered functional materials"

Mathias Casiulis,[1,2,*] Aaron Shih,[3,1,*] and Stefano Martiniani[3,1,2,†]

[1] *Center for Soft Matter Research, Department of Physics, New York University, New York 10003, USA*
[2] *Simons Center for Computational Physical Chemistry, Department of Chemistry, New York University, New York 10003, USA*
[3] *Courant Institute of Mathematical Sciences, New York University, New York 10003, USA*

(Dated: March 11, 2025)

I. STRUCTURE FACTORS OF BANDGAP FORMERS

We argue in main text that all previously proposed aperiodic bandgap formers had one specific commonality: the presence of a feature in $S(k)$ at $k = 2k_{gap}$, where k_{gap} is the wavevector of the bandgap, such that $S(k) > 1$

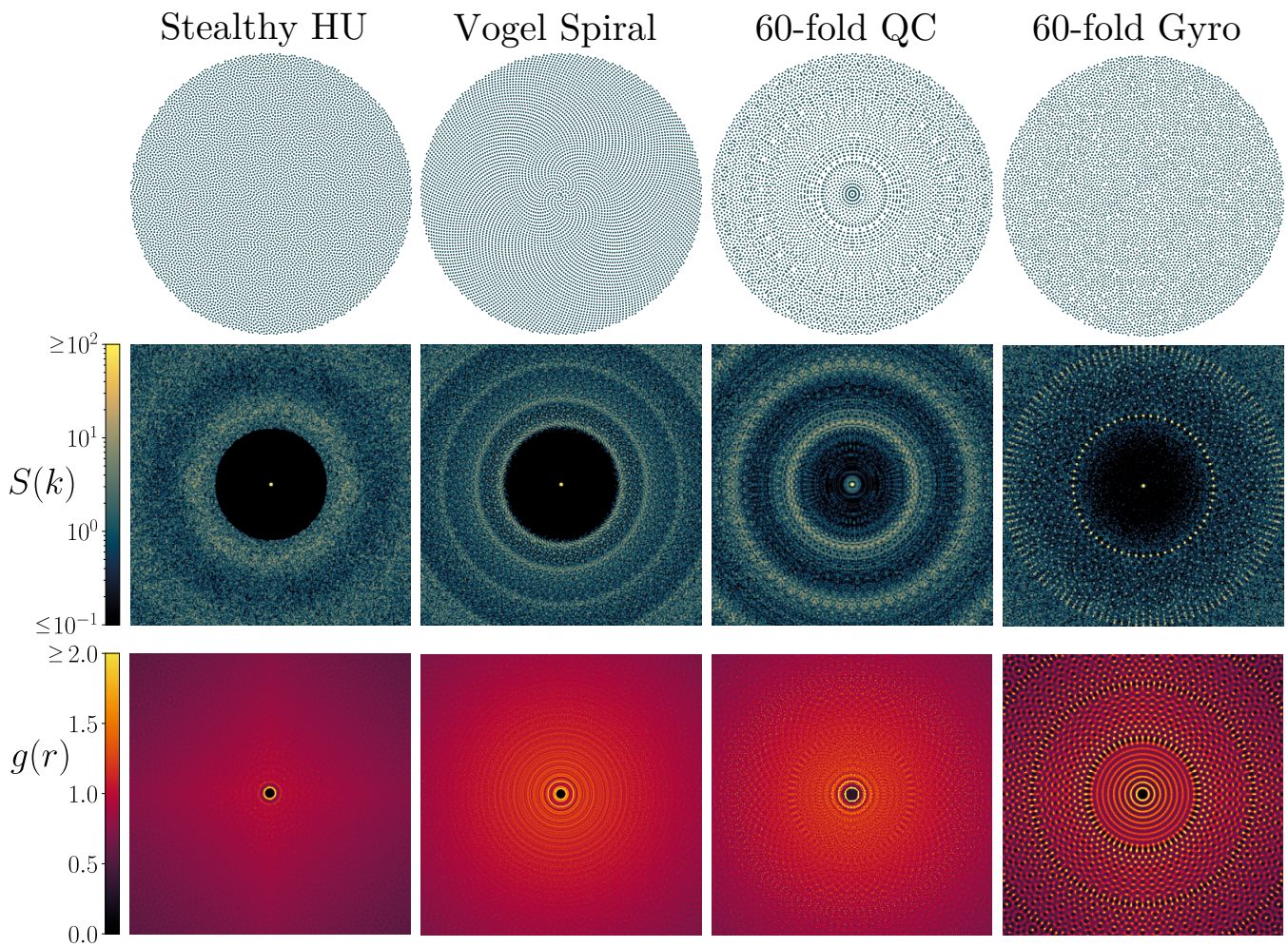


FIG. S1. **Structure factors of bandgap formers.** Point patterns $\rho(\boldsymbol{r})$ (top row), structure factors $S(\boldsymbol{k})$(middle row) and $2d$ pair correlation functions $g(\boldsymbol{r})$ (bottom row) of the systems considered in the main text, from left to right, a stealthy hyperuniform point pattern, a Vogel spiral, a 60-fold de Bruijn quasicrystal, and a 60-fold gyromorph.

* Equal contribution.
† sm7683@nyu.edu

surrounded by lower values. In Fig. S1 we show complete evidence supporting this fact. The middle row shows intensity maps of the $2d$ structure factors, and the bottom row intensity maps of the $2d$ $g(\boldsymbol{r})$ of the systems studied in main text: a stealthy hyperuniform system, a Vogel spiral, a 60-fold de Bruijn quasicrystal, and a 60-fold gyromorph. In this figure, all systems contain $N \sim 10^4$ points, filling up a circular volume with diameter L homogeneously (top row). The stealthy hyperuniform configuration was prepared using FReSCo [1], at a "degree of stealthiness" $\chi \equiv \mathcal{N}_K/(2d(N-1)) = 0.5$, where $\mathcal{N}_K$ is the number of modes constrained to have low structure factor values. This value was reported to display a pseudogap in past works [2–4].

The structure factor, both here and in the main text, is computed using a type-I transform from the FINUFFT [5, 6] library, which avoids explicitly discretizing the point pattern to compute its FFT (and periodicizes the system for these plots). The transform is here computed for 200 modes on either side of the origin and on each axis. Note that for the sake of comparison, we cap the log-scale intensity map on both ends. The $g(\boldsymbol{r})$, both here and in the main text, is computed independently in real space by binning distance vectors between particles, using square bins with sidelength $\delta \equiv 0.05 * L/(2\sqrt{N})$ (1/20 of the typical distance between points). The result is here plotted in the range $[-L/4; L/4]^2$. To better show the structure, the top of the intensity map is capped.

The figure clearly shows commonalities between all considered systems in both real and reciprocal spaces. In $S(\boldsymbol{k})$, all these systems display a near-isotropic low-high-low feature in their intensity when moving away from the center radially. The ring of high values assumes different maximal intensities, degrees of isotropy, and typical widths depending on the system under consideration: gyromorphs are a proposed way to maximize intensity, remain close to isotropic, and minimize width for that feature. Note that the values of the $S(\boldsymbol{k})$ near zero are generally smaller, but not generically stealthy. Quasicrystals, while they are stealthy in the limit of infinite system size, have a dense set of finite-width peaks in finite size, leading to many non-zero values in the measured $S(\boldsymbol{k})$, and gyromorphs achieve low but clearly non-zero values near the center, as discussed in the main text.

Note that the ring of higher values in the stealthy hyperuniform system is not a consequence of being stealthy in general, but is known to systematically appear at high χ ($\chi \gtrsim 0.5$). It has been proposed that this ripple could be understood as a Fourier-space analogue to the appearance of secondary peaks in the $g(r)$ of hard spheres [7]. Coincidentally, bandgaps in stealthy hyperuniform systems prepared using reciprocal-space optimization like FReSCo [8–10] only ever display bandgaps at $\chi \approx 0.5$; the ripple is likely the feature responsible for it. This is also why the bandgap in stealthy hyperuniform systems is in fact very similar to those seen in equilibrium hard sphere configurations [1, 11], or in networked structures with only short-range order [12, 13].

The pair correlation functions, in the bottom row of Fig. S1, also show some similarities (as they should, since they are simply the Fourier transforms of $S(k)$). The first similarity is that all systems display an isotropic exclusion radius near $\boldsymbol{r} = \boldsymbol{0}$, a feature not trivially seen from the structure factor, but argued to be important for bandgaps in the past [13]. Next, notice that there is a typical lengthscale between rings of neighbors appearing in fine, often weak features of the pair correlation. In fact, this feature is particularly strong in gyromorphs: points have extremely regular spacings up to large distances. Note that a shape reminiscent of the gyromorph's $g(\boldsymbol{r})$ structure is also present, but much weaker, in the de Bruijn quasicrystal. This is because the quasicrystal has many peaks of comparable heights, at very different length scales, creating a more complicated superposition of cosines in the $g(\boldsymbol{r})$. Gyromorphs, on the other hand, are by definition structures that amplify just one ring of peaks in $S(\boldsymbol{k})$, and as few other features as possible, resulting in a much less "harmonic-rich" $g(\boldsymbol{r})$.

Note that the comparison between the $S(\boldsymbol{k})$ of quasicrystals and the $g(\boldsymbol{r})$ of gyromorphs (and vice-versa) presented in the main text is performed at very different scales: the rings shown in the $S(\boldsymbol{k})$ of the quasicrystal in Fig. S1 are the innermost rings in the $g(\boldsymbol{r})$ of the gyromorph. Likewise, it is the nearest-neighbor ring in the $g(\boldsymbol{r})$ of the quasicrystal that matches the ring of peaks of the gyromorph.

II. NUMERICAL METHODS

A. Gyromorph generation

To generate gyromorphs, we use the Fast Reciprocal-Space Correlator (FReSCo) [1], an optimization method that imposes arbitrary features into the structure factor of a point pattern. Specifically, we use a variant of the NUwNU (non-uniform real space with non-uniform k-space constraints) routine, which imposes constraints at continuous reciprocal space positions, assuming free boundary conditions for the point pattern. The usual NUwNU amounts to minimizing a loss function, defined as

$$L_{\mathrm{NUwNU}}(\boldsymbol{r}_1, \ldots, \boldsymbol{r}_N) \equiv \sum_{p=1}^{G/2} (S(\boldsymbol{k}_p) - S_0(\boldsymbol{k}_p))^2, \tag{S1}$$

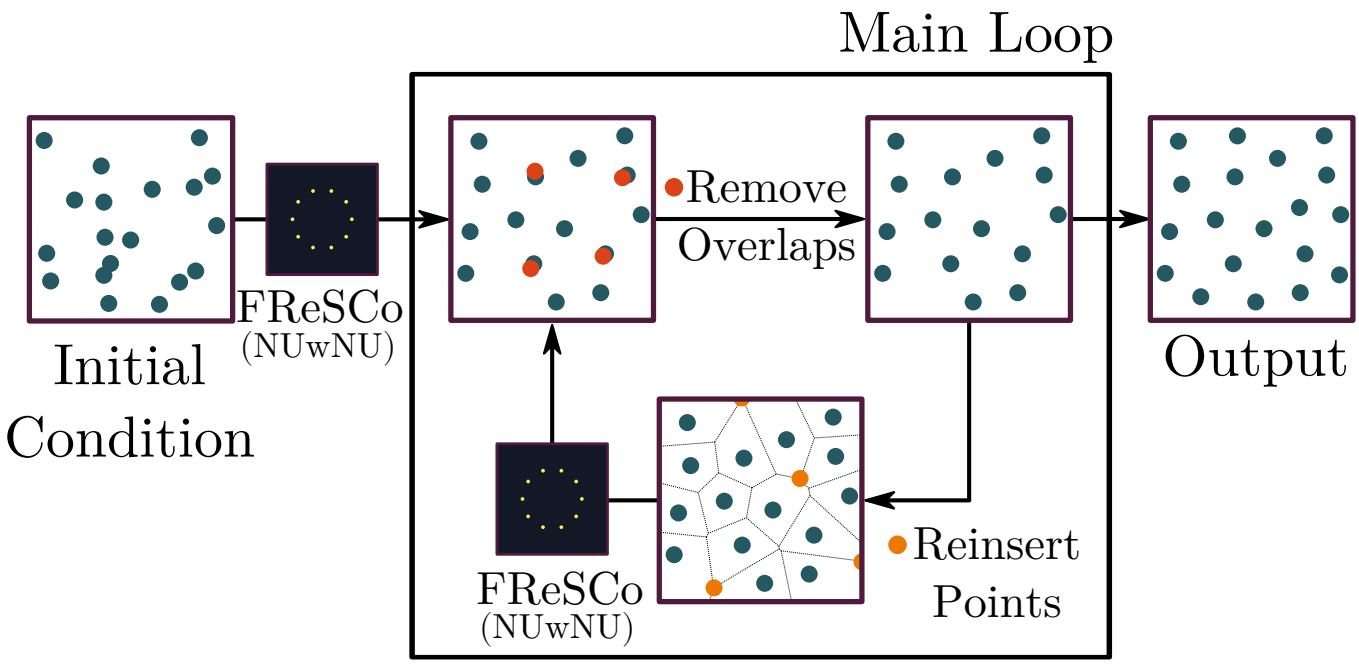


FIG. S2. **Algorithm: generation of a gyromorph.** Sketch of the generation procedure for a 10-fold gyromorph.

where the sum runs over $G/2$ peaks placed at locations $\boldsymbol{k}_p$ of a continuum Fourier space, and S_0 is a target value at these specific locations. Assuming that all $\boldsymbol{k}_p$ are distinct and belong to the same half-space, the $G/2$ peaks at $-\boldsymbol{k}_p$ are implicitly constrained since the point pattern is a real-valued field [1, 14, 15]. Within this paper, we set $\boldsymbol{k}_p$ to be regularly spaced on a circle in $2d$, and on a sphere in $3d$, with a modulus K. Furthermore, we set the target to height $S_0(\boldsymbol{k}_p) = N \sim K^2$. To ensure that peaks are about equal heights throughout the minimization, which prevents the emergence of lower-symmetry configurations, we also add an extra term to the loss that controls the variance across peaks,

$$L_{var} \equiv \frac{C_{var}}{G} \sum_{p=1}^{G} \left(S(\boldsymbol{k}_p) - \overline{S_G} \right)^2 , \tag{S2}$$

where C_{var} is an arbitrary scaling factor that weighs this term against the main FReSCo term, and

$$\overline{S_G} \equiv \frac{1}{G} \sum_{p=1}^{G} S(\boldsymbol{k}_p). \tag{S3}$$

Using that, for $\rho(\boldsymbol{r}) = \sum_{n=1}^{N} c_n \delta(\boldsymbol{r} - \boldsymbol{r}_n)$ with $c_n \in \mathbb{C}$,

$$\frac{\partial S}{\partial \boldsymbol{r}_n}(\boldsymbol{k}) = \frac{2}{N} \mathrm{Re}\left[\widehat{\rho}(\boldsymbol{k}) \frac{\partial \widehat{\rho}^{\dagger}}{\partial \boldsymbol{r}_n}(\boldsymbol{k}) \right] = 2Re\left[-\frac{i\boldsymbol{k} c_n^{\dagger}}{N} \widehat{\rho}(\boldsymbol{k}) e^{-i\boldsymbol{k}\cdot\boldsymbol{r}_n} \right]. \tag{S4}$$

The gradient of the variance component of the loss may then be written explicitly as

$$\frac{\partial L_{var}}{\partial \boldsymbol{r}_n} = -\frac{2C_{var}}{NG} \sum_{p=1}^{G} \left[\frac{\partial S}{\partial \boldsymbol{r}_n}(\boldsymbol{k}_p) - \frac{\partial \overline{S_G}}{\partial \boldsymbol{r}_n} \right] \left(S(\boldsymbol{k}_p) - \overline{S_G} \right). \tag{S5}$$

which, noticing that

$$\sum_{p=1}^{G} \frac{\partial \overline{S_G}}{\partial \boldsymbol{r}_n} \left(S(\boldsymbol{k}_p) - \overline{S_G} \right) = \boldsymbol{0} \tag{S6}$$

eventually yields

$$\frac{\partial L_{var}}{\partial \boldsymbol{r}_n} = -\frac{2C_{var}}{NG}\mathrm{Re}\left[\sum_{p=1}^{G}\left(S(\boldsymbol{k}_p) - \overline{S_G}\right) i\boldsymbol{k}_p\hat{\rho}(\boldsymbol{k}_p)c_n^\dagger e^{-i\boldsymbol{k}_p\cdot\boldsymbol{r}_n}\right]. \tag{S7}$$

Like the FReSCo loss [1], this can be read as an inverse Fourier transform, $\frac{\partial L_{var}}{\partial \boldsymbol{r}_n} = \mathrm{Re}[\widehat{g}_{var}(\boldsymbol{r}_n)]$ with $g_{var}(\boldsymbol{k})$ defined as

$$g_{var}(\boldsymbol{k}) = -\frac{2C_{var}}{NG}\left(S(\boldsymbol{k}) - \overline{S_G}\right) i\boldsymbol{k}\hat{\rho}(\boldsymbol{k})c_n^\dagger. \tag{S8}$$

This expression conveniently uses only values that are already computed to evaluate the usual FReSCo gradient [1]: this extra loss and its gradient may both be computed within the same Fourier transforms as those used to compute the FReSCo loss and gradient. Starting from an initially uncorrelated random point pattern, we minimize the total loss $L = L_{NUwNU} + L_{var}$. In practice, throughout this work, we set $C_{var} = 1$.

Interestingly, we show in main text that after minimizing, $S(\boldsymbol{k}_p) \propto N/G$ (the largest achievable peak height scaling, see argument in Sec. III B), so that $S(\boldsymbol{k}_p) \ll S_0(\boldsymbol{k}_p)$ at the imposed peaks. As a result, the loss in Eq. 1 is well approximated by:

$$L(\boldsymbol{r}_1, \ldots, \boldsymbol{r}_N) \sim -\sum_{p=1}^{G/2} S(\boldsymbol{k}_p). \tag{S9}$$

This simpler asymptotic expression is useful to get intuition about the effective interaction between particles. Indeed, recalling the definition of $S(k)$ from the Fourier transform of the density field, and introducing $\boldsymbol{r}_{mn} \equiv \boldsymbol{r}_n - \boldsymbol{r}_m$ one may write

$$S(\boldsymbol{k}) = \frac{1}{N}\sum_{m,n=1}^{N} e^{i\boldsymbol{k}\cdot\boldsymbol{r}_{mn}} \tag{S10}$$

$$= 1 + \frac{2}{N}\sum_{1\le m<n\le N} \cos\boldsymbol{k}\cdot\boldsymbol{r}_{mn}. \tag{S11}$$

As a result, for $G \gg 1$, gyromorphs can be thought of as minima of an energy landscape, built up by pairwise interactions given by a potential

$$V_G(\boldsymbol{r}) \propto -\sum_{p=1}^{G/2} \cos(K\hat{\boldsymbol{e}}(\theta_p)\cdot\boldsymbol{r}), \tag{S12}$$

where $\theta_p = 2\pi p/G$. This effective pairwise interaction is long-ranged, and very peculiar in that it depends on externally defined directions. In fact, it assumes a shape similar to the $g(\boldsymbol{r})$ we report in the main text and in the gyromorph column of Fig. S1, as obtained from an inverse Fourier transform of $S(k)$. Note however that, unlike in holographic techniques used to trap colloids along a similar function [16] or in kaleidoscopic fields [17, 18] used to etch into materials [19, 20], this function here acts as a pair potential between points, not just as an external field, making our gyromorphs distinct from both categories of systems. Also note that our full loss also contains a 4-point potential term due to the $S(k)^2$ term, which is not captured by this approximation, and the variance component of the loss that also affects interactions.

The optimization is performed by feeding the configuration and gradient to L-BFGS [21], a quasi-Newton method, with a maximal step size and a backtracking line-search [22]. During minimization, points are neither precluded from exiting the box where they started, nor from overlapping exactly. We thus periodically remove points that drifted outside of the box, as well as points closer than π/K, the first maximum of the effective potential in Eq. 12, and reinsert as many points as we removed, then minimize again. To limit the number of overlaps at the next cycle, the reinsertion sites are chosen as the Voronoi sites lying furthest from their neighboring points (farthest-first batch insertion [23]). Each minimization step is run either until 10^4 steps have been computed, or until the gradient of the loss becomes smaller than 10^{-20}, whichever comes first. We thus create a G-fold gyromorph.

B. Structure factor calculations

Throughout the paper, we plot a number of structure factors. To plot them in spite of the finite size of systems and of the fact that they have free boundary conditions, we perform the following operations.

First, the point pattern is rescaled so that its points are in the support $[-L/2; L/2]$. Then, we cut the system into a disk with radius $L/2$, the largest disk inscribed in the square, which is the system we use for optical measurements in practice. Then, we window the density function using a Hamming window, meaning that the effective density field fed into Fourier transforms is

$$\rho_w(\boldsymbol{r}) = \sum_{n=1}^{N} c_n(r)\delta(\boldsymbol{r} - \boldsymbol{r}_n), \tag{S13}$$

where

$$c_n(r) \equiv \frac{1}{\mathcal{N}}\left(a_0 + a_1 \cos\frac{2\pi r}{\sqrt{2}L}\right) \tag{S14}$$

and $a_0 = 0.54$, $a_1 = 0.46$, following standard conventions for the coefficients of the Hamming window [24], and setting the zero at the maximal distance in the initial square. The normalization $\mathcal{N}$ is set so as to preserve the total mass in the field, $\sum_{n=1}^{N} c_n = N$.

We emphasize that these operations are strictly performed to avoid periodicization artifacts in $2d$ intensity maps, which are computed with non-uniform to uniform Fourier transforms (Type 1 transforms in fiNUFFT [5, 6]), and are *not* affecting the gyromorph generation algorithm, which only relies on non-uniform to non-uniform transforms (Type 3 transforms in fiNUFFT [5, 6]). Likewise, they do not affect any $g(\boldsymbol{r})$, as these are computed in real space by binning pair distances. Likewise, when reporting the profile and height of peaks, we use Type 3 transforms to evaluate points around the peak.

III. STRUCTURE OF GYROMORPHS

A. Scalings of $3d$ gyromorphs' peaks

In the main text, we show evidence that peak heights scale like $S(\boldsymbol{k}_p) \sim N/G$ at peak locations $\boldsymbol{k}_p$ in $2d$. Here, we show that the same result is recovered in $3d$ gyromorphs. We generate a set of $3d$ gyromorphs with various K and G values, and report results in Fig. S3. In the main panel, we show the profile of the peak at $(KL/2\pi, 0)$, normalized by its height, as a function of the distance $|k - k_p|L/2\pi$ to the maximum, across system sizes for $G = 1212$. As N grows, the profile converges to $\prod_{a\in x,y,z} \mathrm{sinc}^2(k_a L/2)$, implying that the linear width of the peaks in k-space decays like $1/L$. Note that the convergence is slower with N than in $2d$, as it depends on the number of particles per sidelength, $N^{1/d}$, rather than the number of points. The inset shows that, for different values of G, the peak heights grow like $\mathcal{O}(GN)$, indicating that the peaks are extensive for any fixed order symmetry. Altogether, the peaks have extensive height while their area decays like $1/L^3 \sim 1/N$: they approach Dirac deltas as N increases, like in the $2d$ case discussed in main text.

B. Real-space structure

In this section, we discuss the real-space structure of gyromorphs in more detail, in particular the radius at which a gear forms and the relation between gyromorphs, Moiré patterns, and quasicrystals.

First, we give a simple argument to evaluate the value of R_G and the number of rings in the isotropic part of the $g(r)$ of gyromorphs. In a nutshell, we note that G-fold order can only be supported on a ring large enough that it may contain G points. In other words, since the distance between two neighboring points on the ring is the nearest-neighbor distance $a = 2\pi/K$, the perimeter of the gear has to be such that $2\pi R_G \geq Ga$. Thus, $R_G \gtrsim G/K$. Furthermore, since rings are located at radii multiple of a, $R_G = N_G a$ and the ring carrying the rotational order is the $N_G \equiv \lceil G/(2\pi)\rceil$-th one. For instance, in the example $G = 60$ that we focus on in the main text, $N_G = 10$. Note that for small G, we recover the square ($G = 4$) and triangular ($G = 6$) lattices ($N_G = 1$) [1].

We now turn our attention to the structure of gyromorphs as we tune the value of G. To do so, in Fig. S4, we show intensity maps of the $S(\boldsymbol{k})$ and $g(\boldsymbol{r})$ for a few different values of G, namely $8, 10, 14, 24, 50, 100$, all of them for $K = 100$. The intensity maps highlight that as G grows, the extent of peaked $S(\boldsymbol{k})$ features decreases. While at low G we find structure factors with many peaks other than the ones we imposed, in a way that is reminiscent of quasicrystals, at high G only a small region has peaks. Furthermore, even these peaks have intensities that are noticeably lower than on the ring we constrained. In real space, at low G the $g(\boldsymbol{r})$ displays very sharp anisotropic features (high values surrounded by very low values) up to large distances. However, at large G, the long-distance

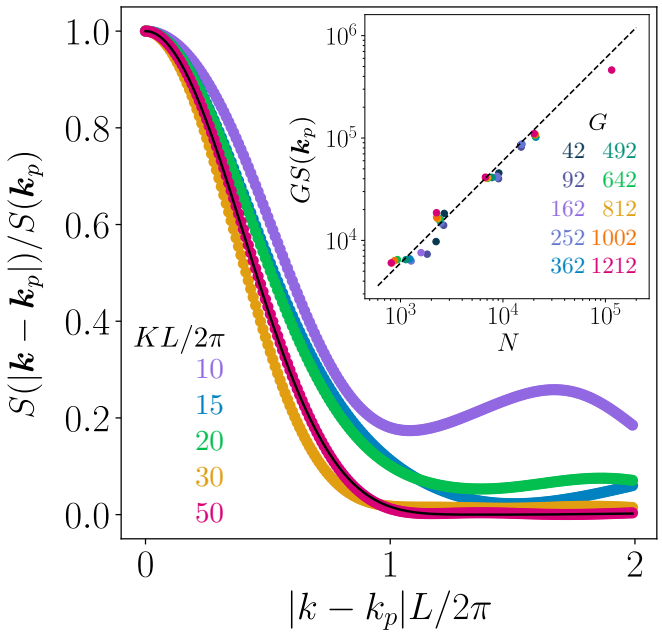


FIG. S3. **Scaling of peak height in** $3d$ **gyromorphs.** Radially averaged profile of peaks across K values, rescaled by peak height (colored lines) a solid black line indicates the radial profile of $\mathrm{sinc}^2(k_xL/2)\mathrm{sinc}^2(k_yL/2)\mathrm{sinc}^2(k_zL/2)$. Inset: Rescaled peak height $GS(\boldsymbol{k}_p)$ against N, in log scales, across G (colored symbols). A dashed black line shows $GS(\boldsymbol{k}_p) = N$.

region becomes less contrasted, with broader features. Furthermore, note that the number of isotropic rings near the center grows following $N_G \equiv \lceil G/(2\pi) \rceil$ as we proposed: $N_8 = N_{10} = 1$, $N_{14} = 2$, $N_{24} = 4$, $N_{50} = 8$ and $N_{100} = 16$.

As the structure factor becomes better and better approximated by one ring of peaks surrounded by a flat background, the $g(\boldsymbol{r})$ actually approaches a Moiré pattern (save near 0, as $g(0) = 0$ by construction). Indeed, if S approaches the shape

$$S(\boldsymbol{k}) = 1 + (2\pi)^d \rho_0 \delta(\boldsymbol{k}) + C(2\pi)^d \rho_0 \sum_{p=1}^{G} \delta(\boldsymbol{k} - \boldsymbol{k}_p) \tag{S15}$$

with $C > 0$ a real constant and $\rho_0 = N/L^2$ the average number density (the constant multiplying C being chosen in the same way as for usual Bragg peaks [15]), and the central peak ensures that the point pattern contains N points. One may write $g(\boldsymbol{r})$ as the Fourier transform [25],

$$g(\boldsymbol{r}) = \frac{1}{\rho_0} \int_{\mathcal{F}} \frac{d^d\boldsymbol{k}}{(2\pi)^d} (S(\boldsymbol{k}) - 1) e^{-i\boldsymbol{k}\cdot\boldsymbol{r}}, \tag{S16}$$

which immediately yields

$$g(\boldsymbol{r}) = 1 + C \sum_{p=1}^{G} \cos \boldsymbol{k}_p \cdot \boldsymbol{r}. \tag{S17}$$

Note in particular that non-negativity of g already suggests $C \propto 1/G$ at most, as empirically observed in gyromorphs.

Examples of this function are shown in Fig. S5 for a subset of the symmetries of Fig. S4. Notice how close to the observed $g(\boldsymbol{r})$ of gyromorph this function becomes as G becomes large – the main difference being that due to the exclusion of perfect overlaps the g of gyromorphs does not feature a central peak. This is an indication that gyromorphs actually do approach the maximal possible height for the constrained peaks. Note that this Moiré shape is however distinct from the point pattern itself: one may not simply subselect all local maxima of the $g(\boldsymbol{r})$ and recover the gyromorph. Finally, note that the replacement of the central peak by hardcore exclusion in gyromorphs qualitatively explains the presence of a hard-sphere-like smooth variation of S at small k.

To complete the picture, we compute the angularly averaged versions of both the structure factors and pair correlation functions of Fig. S4. The results are shown in Fig. S6, for the same set of systems, showing the structure

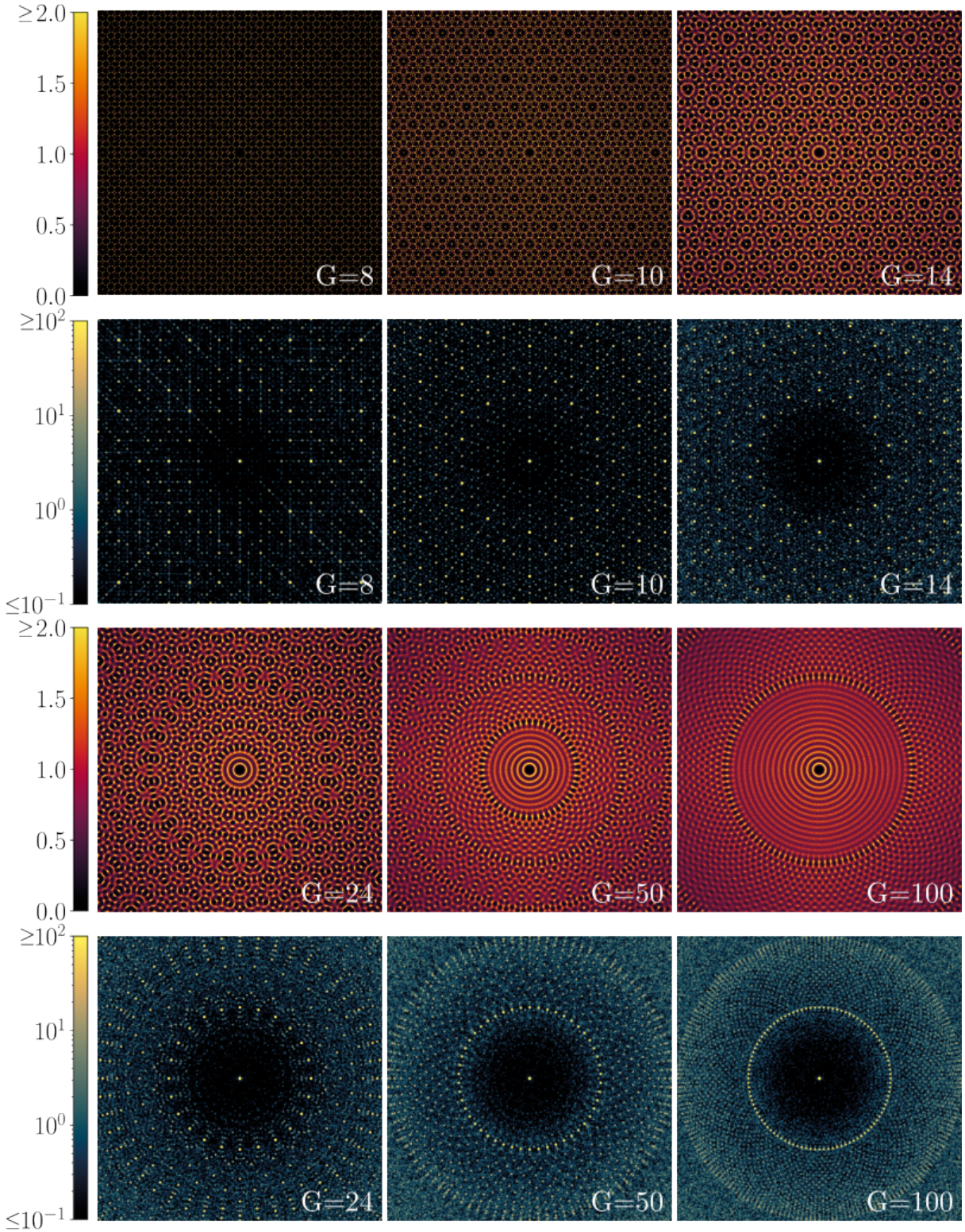


FIG. S4. **Structure of gyromorphs.** $g(\boldsymbol{r})$ (first and third rows) and $S(\boldsymbol{k})$ (second and fourth rows) of gyromorphs for $G = 8$, 10, 14, 24, 50, 100 and $KL/2\pi = 100$. $S(\boldsymbol{k})$ are plotted up to $2K$ in both directions, and $g(\boldsymbol{r})$ up to $L/4$.

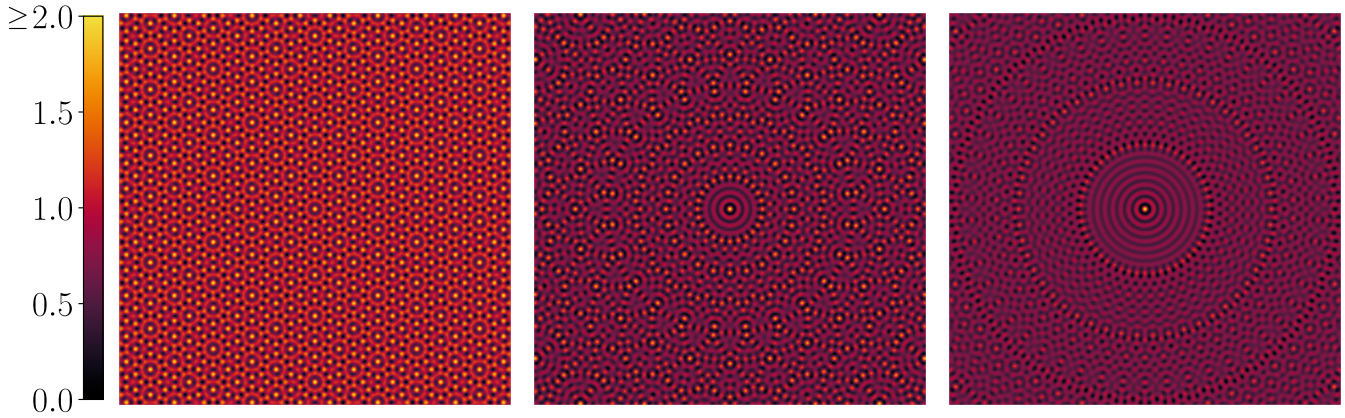


FIG. S5. **Moiré patterns.** Example intensity plots of analytical Moiré patterns for $G = 10$, $G = 24$, and $G = 50$ from left to right. We choose $C = 1/G$, $K = 2\pi$ and the plotting range is $[-50; 50]^2$.

factor in lin-log scales and the radial correlation function in linear scale. For these plots, as well as the angularly averaged curves in the main text: $S(\boldsymbol{k})$ is computed like in the intensity map of Fig. S4 then pixel distances to the origin are binned with a binsize equal to the pixel size, while the RDF is directly binned into radial distances. These curves show, as argued in the main text, and in the discussion of Fig. S4, that at low G the $S(k)$ retains peaks of high intensity reminiscent of a quasicrystal up to large values of k. Note however that these peaks are attenuated much faster than in a finite quasicrystal, and that the first peak is systematically higher (see Appendix of the main text). As G increases, fewer and fewer extra peaks are visible in $S(k)$, to the point that the system essentially becomes radially Poisson-like for $k \gtrsim 2K$ at $G = 100$. As for $g(r)$, the low-G structures display very sharp and high angularly averaged peaks but, as G increases, the oscillations of $g(r)$ become smoother and smoother.

Importantly, the rate of decay of $g(r)$ can be characterized from such radial measurements. As noted in main text, the decay is power-law at large distances like that of $g_G(r)$. We show additional evidence of that fact in Fig. S7. In Fig. S7(a), we plot rescaled versions of $|h|$ in log-log so as to collapse a few values of G together. The curve shows that for $r > R_G$, the decay of the envelope is close to a $1/r$ behavior, much like the g_G shown in main text. For $r < R_G$, there is also a slower decay. While it is not clear whether the envelope actually follows a power-law due to the variability of peak heights within that domain, the decay lies close to a $1/\sqrt{r}$ power. Without lending too much credence to that value, it is at the very least clearly slower than the long-range behavior. To go further, in Fig. S7(b), we compare the decay in a gyromorph to that in a quasicrystal with the same typical number of points. While the quasicrystal, as usual, features an extremely high peak at the edge length of its rhombus tiling, it also displays some slow decay. Interestingly, it is closer to the slow, low-r decay of gyromorphs than to their large-r decay, as shown by the dashed line indicating a power $1/\sqrt{r}$. For the sake of completeness in the comparison, in Fig. S7(c), we also reproduce the quasicrystal data, rescaled using the location of its highest peak in $g(r)$ as an R_G, along with the rest of Fig. S7(a). This comparison shows in a clearer way that the quasicrystalline $g(r)$ has a different decay behavior than the gyromorphic ones. Thus, the long-range decay of correlations in gyromorphs, while it appears to be power-law, is notably faster than in quasicrystals.

The decay of rotational order can also be characterized in polygyromorphs. We mention in the main text that they display the same decay of each of their rotational orders as gyromorphs that have a single ring of peaks. We show evidence of that fact for the example polygyromorph used in the main text in Fig. S8. We plot the gyromorphic correlation for each of the imposed rotational orders, rescaling each time both axes by the corresponding R_G. The result is similar to that obtained across G values in distinct gyromorphs: the correlation is low for $r < R_G$, then decays with an exponent close to -1 for $r > R_G$.

It is natural to compare the order of gyromorphs as reported in Figs. S4 and S6 to that of de Bruijn quasicrystals. To do so, we generate quasicrystals with a similar number of points, $N \sim 10^4$ at the same symmetries, and compute the same quantities *over the same ranges of k and using the same intensity scales*, although these are not the most adapted scales to characterize quasicrystalline order. The results for $2d$ intensity maps in Fig. S9. The main take-away is that it is now the $g(r)$ that is Dirac-delta peaked (with peaks one pixel wide in the figure), due to the underlying construction relying on a finite deterministic set of rhombi with a finite number of allowed orientations at each site. As a result, the $g(r)$ contains a ring of Dirac deltas forming a regular G-gon at its center, so that the $S(k)$ features a Moiré pattern structure, as pointed out in the Appendix of the main text. However, note that the correspondence established in that same appendix between $(g(\boldsymbol{r}), S(\boldsymbol{k}))$ of quasicrystals and $(S(\boldsymbol{k}), g(\boldsymbol{r}))$ of gyromorphs is only visible by changing the plotrange of these intensity maps. Indeed, the ring of peaks in the $S(\boldsymbol{k})$ of the gyromorphs corresponds

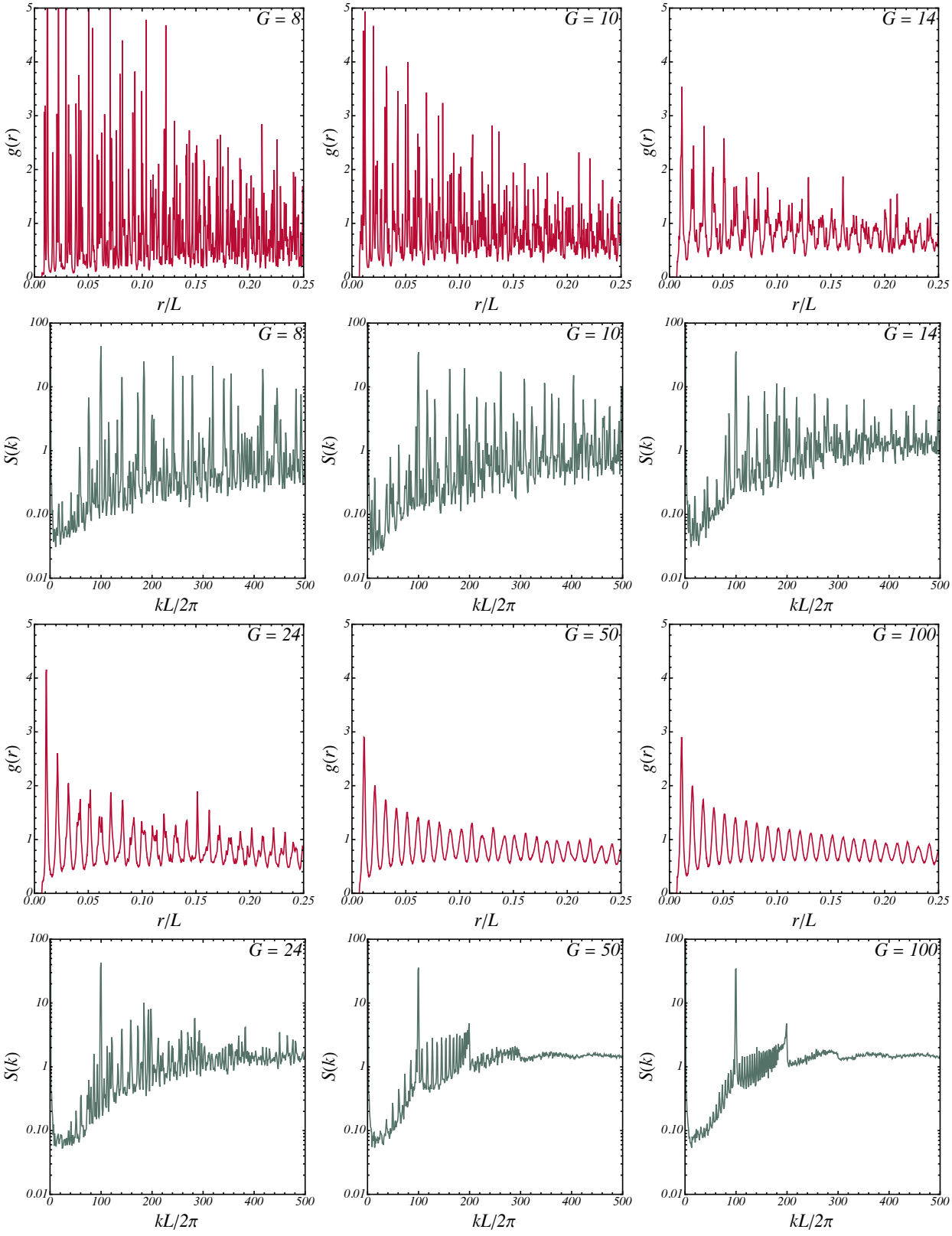


FIG. S6. **Angularly averaged structure of gyromorphs.** $g(r)$ (first and third rows, in linear scales) and $S(k)$ (second and fourth rows, in lin-log scale) of gyromorphs for $G = 8$, 10, 14, 24, 50, 100 and $KL/2\pi = 100$, same as in Fig. S4.

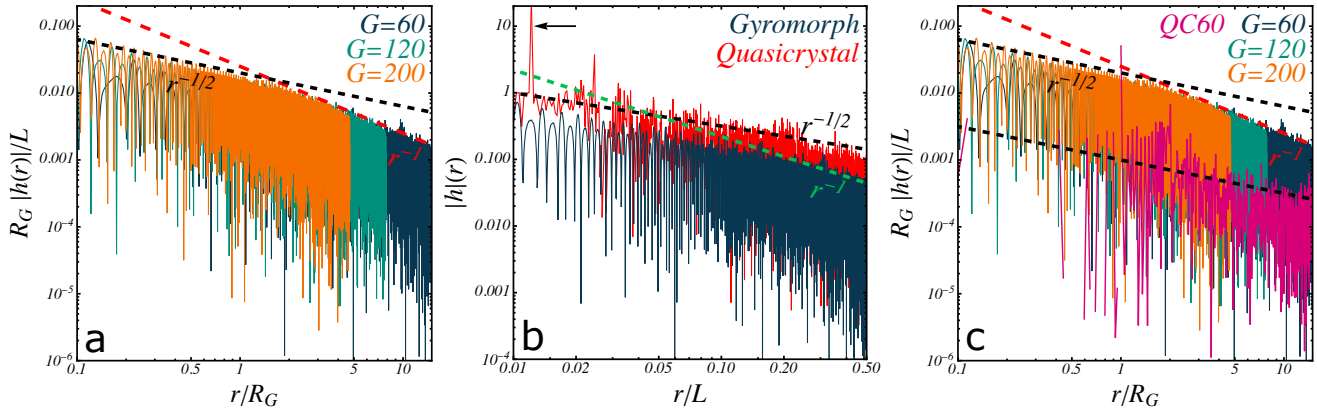


FIG. S7. **Decay of pair correlations in gyromorphs.** (*a*) Log-log plot of the absolute value of the connected radial pair correlation $|h|$ against distance, rescaled by R_G so as to collapse curves for a few G. Dashed lines are guides for the eye, showing powers -0.6 (black dashed line) and power -1 (red long-dashed line). (*b*) Comparison between the $|h|$ of a 60-fold gyromorph (blue) and a 60-fold quasicrystal (red). An arrow indicates the 60-fold (nearest-neighbor) peak of the quasicrystal. The $1/r$ trend is reproduced in green instead of red for readability in this panel. (*c*) Quasicrystal from panel (*b*), rescaled and replotted in the same way (and along with the same data as) panel (*a*), in magenta. To highlight the scaling of its decay off-peak, we copy the $1/\sqrt{r}$ trend lower on the graph.

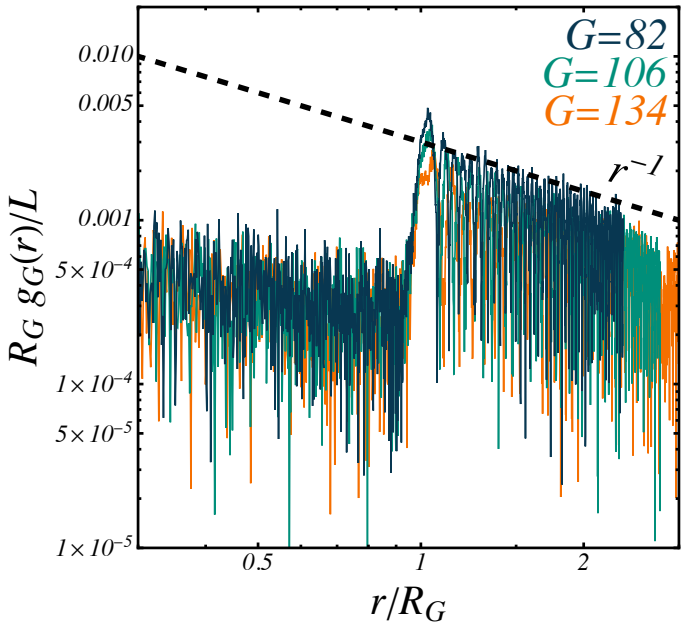


FIG. S8. **Decay of gyromorphic correlations in polygyromorphs.** Log-log plot of the gyromorphic correlation for all 3 imposed rotational orders in the polygyromorph presented in main text. Each correlation is rescaled by the relevant R_G. A dashed line indicates $1/r$ decay.

to the nearest-neighbor peaks of the $g(\boldsymbol{r})$ of quasicrystals (a very small part of the intensity maps of Fig. S9), and consequently the Moiré pattern in the $g(\boldsymbol{r})$ of gyromorphs maps to a very zoomed out version of the $S(\boldsymbol{k})$ shown in Fig. S9. At the largest symmetry, the rings visible in the $S(\boldsymbol{k})$ in Fig. S9 are the equivalent of the isotropic rings at the center of the $g(\boldsymbol{r})$ of gyromorphs.

Likewise, we show in Fig. S10 the corresponding radial profiles of the $g(\boldsymbol{r})$ and $S(\boldsymbol{k})$. Again, these plots are shown using the same plot ranges and axis ranges as Fig. S6, at the cost of losing some information about the height of the peaks in the $g(r)$. We show that the quasicrystalline $S(k)$ are clearly distinct from the gyromorphic ones, especially at high G, where quasicrystals have smooth, broad angularly-averaged features, as opposed to the very peaked features in gyromorphs. As a result, as also justified in the appendix of the main text, the peaks in gyromorphs are higher than in quasicrystals, even at the angularly-averaged level. The real-space structures are also clearly different: while the

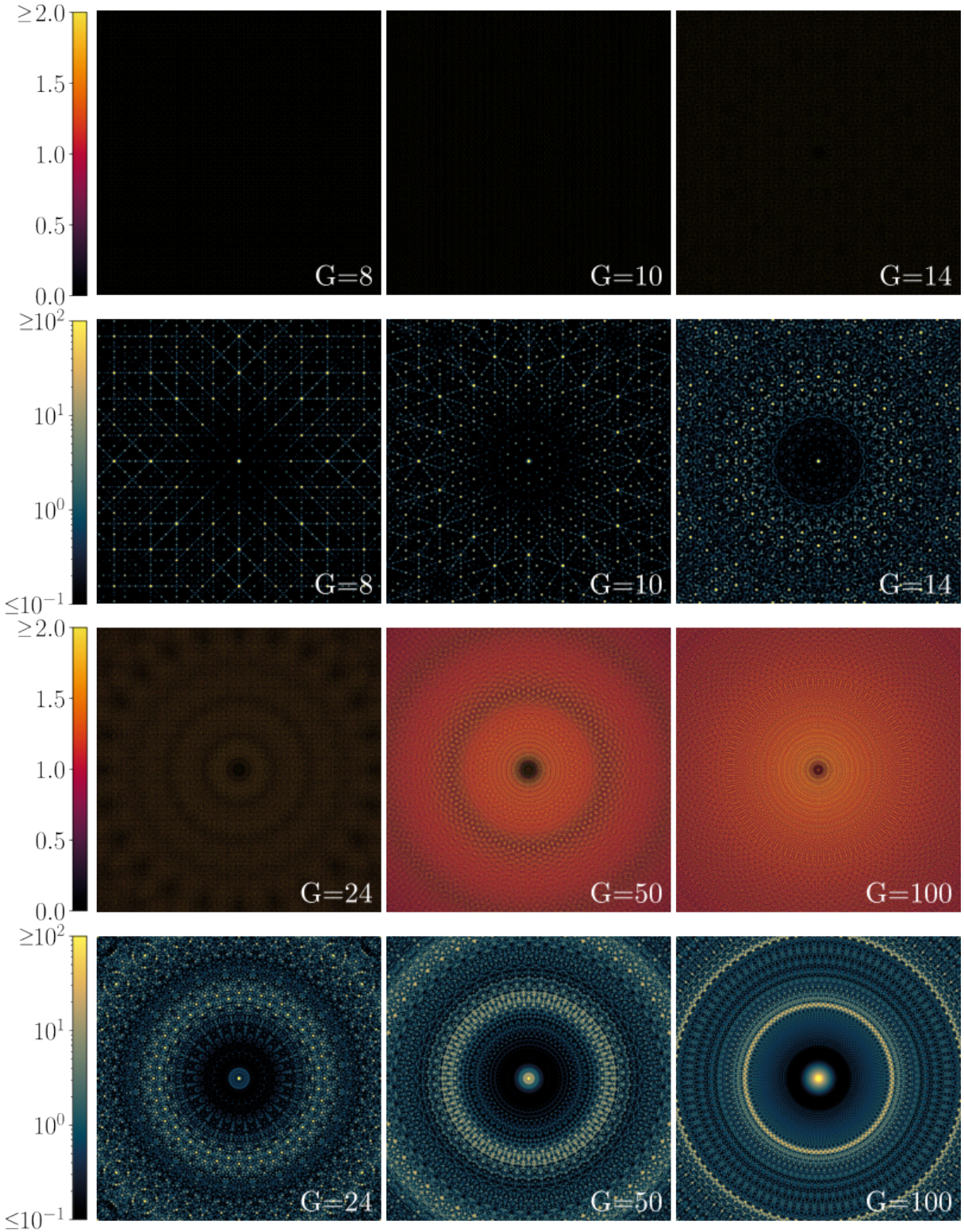


FIG. S9. **Structure of quasicrystals.** $g(\boldsymbol{r})$ (first and third rows) and $S(\boldsymbol{k})$ (second and fourth rows) of de Bruijn quasicrystals for $G = 8$, 10, 14, 24, 50, 100 and $KL/2\pi = 100$. $S(\boldsymbol{k})$ are plotted up to $2K$ in both directions, and $g(\boldsymbol{r})$ up to $L/4$.

$g(r)$ of gyromorphs get consistently smoother as G grows, quasicrystals retain very peaked structures by construction.

Finally, as a last indication that gyromorphs and quasicrystals are clearly different structures, we perform an analysis of the relevant Bond-Orientational Order Parameters [26]. For point n in the point pattern, at a given G, we compute the microscopic observable $\psi_{G,n} \in \mathbb{C}$ defined as

$$\psi_{G,n} \equiv \frac{1}{z} \sum_{m \in \partial n} e^{iG\theta_{mn}}, \tag{S18}$$

with $\theta_{mn} = \measuredangle(\hat{\boldsymbol{e}}_x, \boldsymbol{r}_m - \boldsymbol{r}_n)$ the angle formed between the horizontal and the vector linking point n to one of its z neighbors, here defined by a Delaunay neighborhood. The complex modulus of $\psi_{G,n}$ is close to 1 if a point has neighbors lying on a subset of the regular G-gon, and a lower value otherwise. The argument of $\psi_{G,n}$ encodes for the orientation ϑ of the G-gon on the $2\pi/G$-wide interval it can explore, $\arg \psi_{G,n} = G\vartheta$. In Figs. S11 (gyromorphs) and S12 (quasicrystals), we plot for each G the $2d$ histograms of these quantities in the unit disk, which encode the full variety of local Delaunay environments. In gyromorphs, for small G these histograms show strong directionality along the x axis. This is expected as for these G the orientational order sets in at the level of nearest neighbors, and we impose one of the peaks at $K\hat{\boldsymbol{e}}_x$. The moduli of the microscopic BOOPs shows that there are a few non-equivalent environments (different peaks), and the peaks have finite widths in both the radial and orthoradial directions, indicating some variety in environments. As G grows, however, the orientational order gets imposed at an R_G increasingly far from the nearest-neighbor distance, so that the local BOOPs distribution become isotropic peaks around 0 like in a fluid. This is a stronger indication of local isotropy than $g(\boldsymbol{r})$. Indeed, one could have clear unit-modulus BOOPs but a perfectly isotropic first ring in $g(\boldsymbol{r})$: this is for instance the expected scenario for very large equilibrium hexatic liquids [27] – in that case, while all local environments are hexatic, they also span all possible angles due to soft modes, so that the expected distribution of hexatic vectors in hard disks is an annulus close to 1. Here, instead, we find no BOOP at the relevant G in gyromorphs. By contrast, in quasicrystals, at all orders the distribution of BOOPs is a fine line with finite moduli along positive $\hat{bme}_x$, indicating strong orientational order with the prescribed symmetry at the level of nearest neighbors.

C. Stability against noise

A common source of concern for photonic structures is how resilient they are to fabrication errors, and to random modifications. In particular, it has been argued that disordered structures could be more advantageous than ordered ones because, by virtue of being disordered, they would be less sensitive to extra disorder. We here assess the effect of noise on gyromorphs, as compared to other systems like stealthy hyperuniform patterns. There are essentially 3 kinds of noise that could affect a point pattern: random displacements on the positions, random deletions of points, and random additions of points. The effect of all three has been formalized in the context of stealthy hyperuniform systems [28], we here recall the main results and their implications for gyromorphs.

First, assume that a point pattern is perturbed by independent random kicks of the location of each point. The resulting noised density field reads

$$\rho_{kicked}(\boldsymbol{r}) = \sum_{n=1}^{N} \delta(\boldsymbol{r} - \boldsymbol{r}_n - \boldsymbol{d}_n), \tag{S19}$$

with $\boldsymbol{d}_n$ independent random vector drawn from some distribution. By definition, the Fourier transform of the density field can be written as

$$\widehat{\rho}_{kicked}(\boldsymbol{k}) = \sum_{n=1}^{N} e^{i\boldsymbol{k}\cdot(\boldsymbol{r}_n + \boldsymbol{d}_n)}, \tag{S20}$$

and the ensemble averaged structure factor as

$$\langle S_{kicked}(\boldsymbol{k}) \rangle = \frac{1}{N} \left\langle \left| \sum_{n=1}^{N} e^{i\boldsymbol{k}\cdot(\boldsymbol{r}_n + \boldsymbol{d}_n)} \right|^2 \right\rangle, \tag{S21}$$

where $\langle \cdot \rangle$ represents an average over the distribution of all N displacements. This last expression can be rewritten as

$$\langle S_{kicked}(\boldsymbol{k}) \rangle = \frac{1}{N} \sum_{m,n=1}^{N} e^{i\boldsymbol{k}\cdot\boldsymbol{r}_{mn}} \left\langle e^{i\boldsymbol{k}\cdot\boldsymbol{d}_{mn}} \right\rangle, \tag{S22}$$

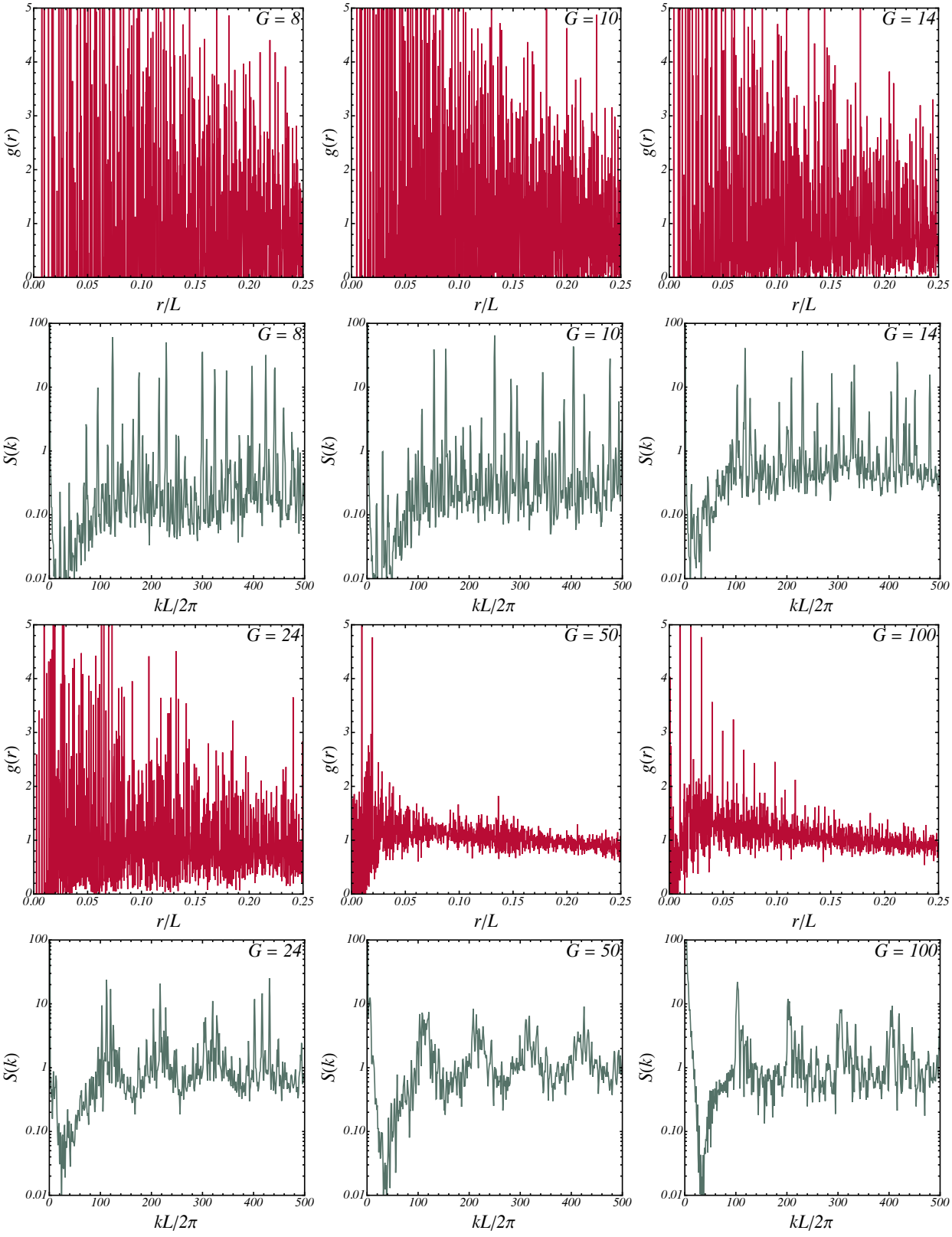


FIG. S10. **Angularly averaged structure of quasicrystals.** $g(r)$ (first and third rows, in linear scales) and $S(k)$ (second and fourth rows, in lin-log scale) of quasicrystals for $G = 8$, 10, 14, 24, 50, 100 and $KL/2\pi = 100$, same as in Fig. S9.

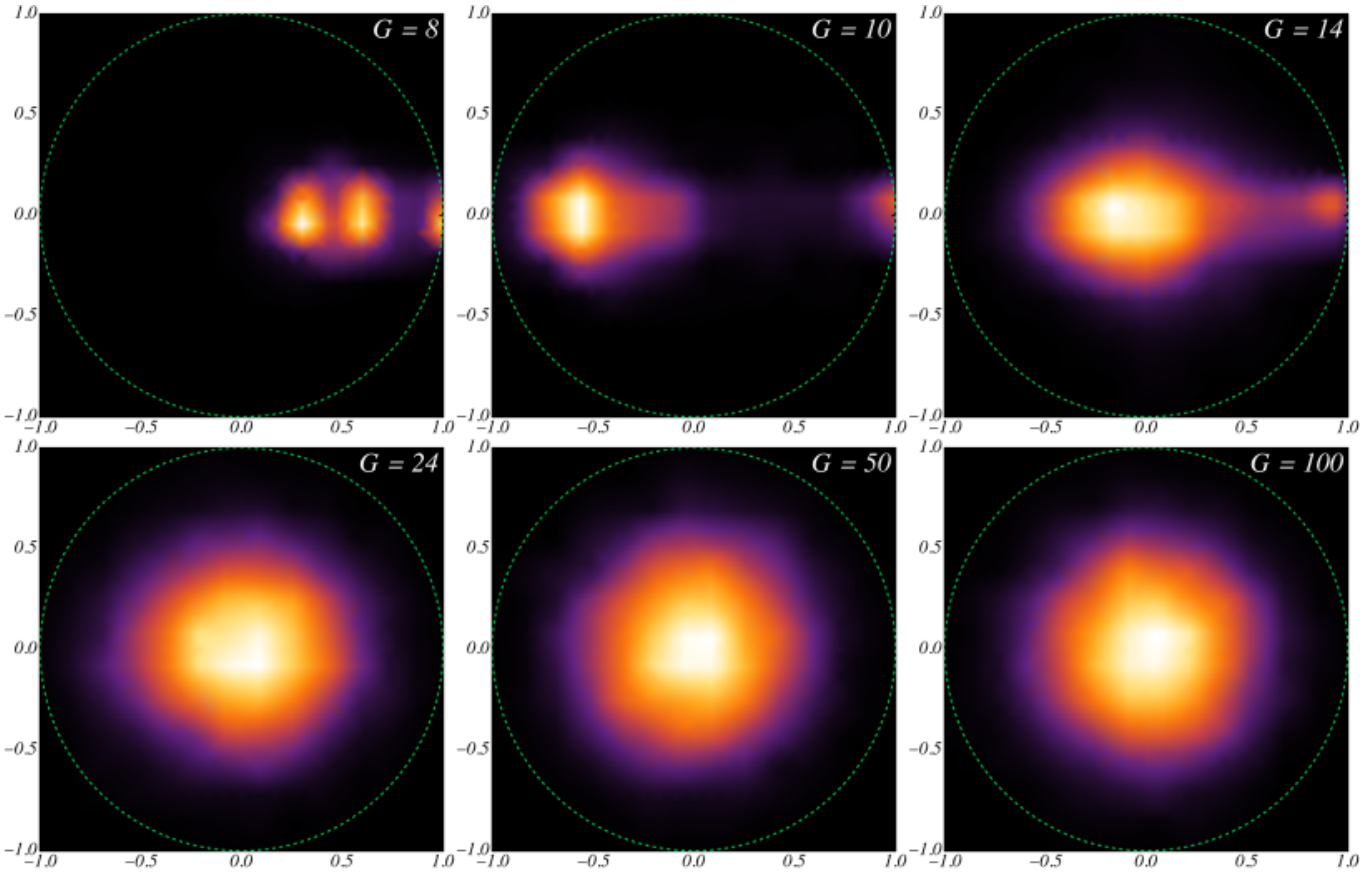


FIG. S11. **BOOPs in Gyromorphs.** Intensity maps of the distribution of $\psi_{G,n}$ in the gyromorphs of Fig. S4. A dashed green circle indicates the border of the unit disk.

where $\boldsymbol{r}_{mn} = \boldsymbol{r}_n - \boldsymbol{r}_m$ and $\boldsymbol{d}_{mn} = \boldsymbol{d}_n - \boldsymbol{d}_m$. Assuming that kicks are are independent random variables, one may write

$$\left\langle e^{i\boldsymbol{k}\cdot\boldsymbol{d}_{mn}} \right\rangle = \left\langle e^{i\boldsymbol{k}\cdot\boldsymbol{d}_n} \right\rangle \left\langle e^{-i\boldsymbol{k}\cdot\boldsymbol{d}_m} \right\rangle = \delta_{m,n} + (1-\delta_{m,n}) \left| F(\boldsymbol{k}) \right|^2 . \tag{S23}$$

in which we identified the square modulus of the characteristic function F of the distribution of displacements, and introduced a Kronecker delta notation. For instance, considering uniform kicks within a $2d$ disk with radius R,

$$F(\boldsymbol{k}) = \frac{1}{\pi R^2} \int_{r=0}^{R} dr \int_{\theta=-\pi}^{\pi} d\theta \, r e^{ikr\cos\theta}, \tag{S24}$$

$$= 2\frac{J_1(kR)}{kR}, \tag{S25}$$

with J_1 a Bessel function of the first kind. Thus, for this example,

$$\langle S_{kicked}(\boldsymbol{k}) \rangle = 1 + \left| F(\boldsymbol{k}) \right|^2 (S_0(\boldsymbol{k}) - 1) = 1 + 4\left(\frac{J_1(kR)}{kR} \right)^2 (S_0(\boldsymbol{k}) - 1), \tag{S26}$$

with S_0 the structure factor before kicking points. As expected, $\langle S_{kicked}(\boldsymbol{k}) \rangle \to 1$ at all k as $R \to \infty$. Furthermore, at finite values, the long-k regime of the structure factor (short range order) is most attenuated. At small kR, one may expand the Bessel function to yield

$$\langle S_{kicked}(\boldsymbol{k}) \rangle \approx 1 + \left(1 - \frac{k^2R^2}{4} \right) (S_0(\boldsymbol{k}) - 1), \tag{S27}$$

$$= \frac{k^2R^2}{4} + \left(1 - \frac{k^2R^2}{4} \right) S_0(\boldsymbol{k}). \tag{S28}$$

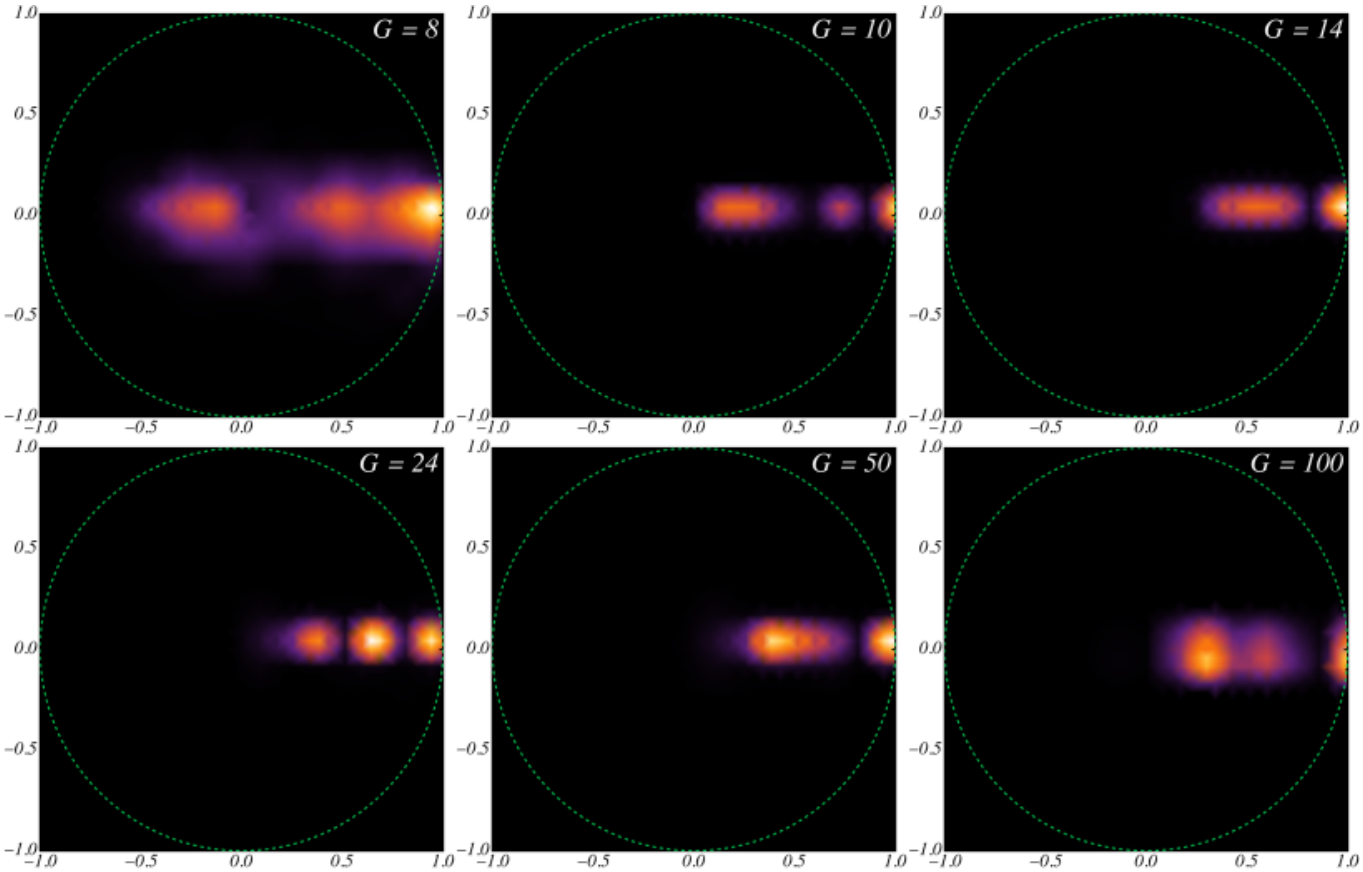


FIG. S12. **BOOPs in Quasicrystals.** Intensity maps of the distribution of $\psi_{G,n}$ in the quasicrystals of Fig. S9. A dashed green circle indicates the border of the unit disk.

This last result is actually fairly generic: for small noise amplitudes, and with most usual noise distributions, a kicked point pattern gains a quadratic term at small k. Now, how does this sort of noise affect the features of the structures we study in this paper? As already noted in past work [1, 28, 29], random kicks quickly deteriorates low features, $S(k) \to 0$, near $k \to 0$, so that stealthiness essentially doesn't survive any amount of noise. As for other features, the larger $|S_0(\boldsymbol{k}) - 1|$, the better they survive. For instance, Bragg peaks in crystals remain visible as long as kicks are not comparable to the lattice spacing [29]. In the example of gyromorphs, we illustrate this in Fig. S13(a), where we show the structure factor of a 200-fold gyromorph where each point has been kicked by independent, random displacements drawn uniformly in a disk with radius R, for a few values of R. The peak remains visible even for a diameter 80% of the typical nearest neighbor distance, but disappears at 100%. Notice that the low-k behavior goes from a plateau to a growing function, as expected.

Next, we consider random additions of uncorrelated points to an existing point pattern. Consider a system starting with $N - p$ points, to which p points are added. The structure factor of that one realization may be written as

$$S_N(\boldsymbol{k}) = \frac{1}{N} \left| \widehat{\rho}_0(\boldsymbol{k}) + \widehat{\rho}_p(\boldsymbol{k}) \right|^2 , \tag{S29}$$

where $\widehat{\rho}_0$ and $\widehat{\rho}_p$ represent the Fourier densities of the initial and additional points, respectively. This expression may be rewritten as

$$S_N(\boldsymbol{k}) = \frac{1}{N} \left| \widehat{\rho}_0(\boldsymbol{k}) \right|^2 + \frac{1}{N} \left| \widehat{\rho}_p(\boldsymbol{k}) \right|^2 + \frac{2}{N} \mathrm{Re} \left[\widehat{\rho}_0(\boldsymbol{k}) \widehat{\rho}_p^\dagger(\boldsymbol{k}) \right] , \tag{S30}$$

$$= (1 - f) S_0(\boldsymbol{k}) + f S_p(\boldsymbol{k}) + \frac{2}{N} \mathrm{Re} \left[\widehat{\rho}_0(\boldsymbol{k}) \widehat{\rho}_p^\dagger(\boldsymbol{k}) \right] . \tag{S31}$$

In the last expression, we introduced S_0 and S_p the structure factors of the initial and additional point patterns taken separately, as well as the fraction of added points $f = p/N$. Assuming that the additional points are a Poisson point

pattern, the average modified structure factor reads, for $\boldsymbol{k} \neq \boldsymbol{0}$,

$$\langle S_N(\boldsymbol{k})\rangle = (1-f)S_0(\boldsymbol{k}) + f, \tag{S32}$$
$$= 1 + (1-f)(S_0(\boldsymbol{k}) - 1), \tag{S33}$$

as $\langle S_p\rangle = 1$ in a Poisson point pattern, and $\langle \widehat{\rho}_p(\boldsymbol{k})\rangle \propto \delta(\boldsymbol{k})$.

Before commenting on this result, we establish the expression of the final structure factor when performing random uncorrelated removals from a point pattern. Consider a point pattern initially containing N points, and assume that a random point is removed, with all points being equiprobably likely to be selected. The new structure factor for one realization of this removal reads

$$S_{N-1}(\boldsymbol{k}) = \frac{1}{N-1}\left|\widehat{\rho}_0(\boldsymbol{k}) - e^{i\boldsymbol{k}\cdot\boldsymbol{r}}\right|^2, \tag{S34}$$

with $\boldsymbol{r}$ the location of the point that was removed. Once again, the square modulus may be expanded as

$$S_{N-1}(\boldsymbol{k}) = \frac{1}{N-1} + \frac{N}{N-1}S_N(\boldsymbol{k}) - \frac{2}{N-1}\mathrm{Re}\left[\widehat{\rho}_0(\boldsymbol{k})e^{-i\boldsymbol{k}\cdot\boldsymbol{r}}\right]. \tag{S35}$$

To average this result over possible realizations of the removal, only the last term needs to be averaged, and for equiprobable removals

$$\left\langle \widehat{\rho}_0(\boldsymbol{k})e^{-i\boldsymbol{k}\cdot\boldsymbol{r}}\right\rangle = \frac{1}{N}\widehat{\rho}_0(\boldsymbol{k})\sum_{p=1}^{N} e^{-i\boldsymbol{k}\cdot\boldsymbol{r}_p} = \frac{1}{N}\left|\widehat{\rho}_0(\boldsymbol{k})\right|^2 = S_0(\boldsymbol{k}). \tag{S36}$$

All in all, for a single removed point,

$$\langle S_{N-1}(\boldsymbol{k})\rangle = \frac{1}{N-1} + \frac{N-2}{N-1}S_N(\boldsymbol{k}). \tag{S37}$$

Treating this expression as a recurrence between average structure factors, one can approximate the structure factor after p removals as

$$\langle S_{N-p}(\boldsymbol{k})\rangle \approx \frac{p}{N-1} + \left(1 - \frac{p}{N-1}\right)S_N(\boldsymbol{k}) \tag{S38}$$
$$= 1 + (1-f')\left(S_N(\boldsymbol{k}) - 1\right), \tag{S39}$$

where $f' \equiv \frac{p}{N-1}$ is close to the fraction of removed points. Note that $S_{N-p} = 1$ for $p = N-1$ as a single point remains, which is why the fraction is offset by 1. This expression should be understood as a sort of mean-field level approximation since it was obtained by treating the relation between the average after one removal and the starting point pattern, rather than the average of a realization with p removals. Nevertheless, this expression is interesting as it assumes nearly the same form as that obtained for the addition of points, and yields the same intuition.

Indeed, for both additions and removals, the result we obtained is that the new structure factor is the weighted arithmetic average of the starting structure factor and that of a Poisson pattern. As a result, features that survive noise best are, again, those that are as distant as possible from 1. This again means that low features like stealthiness are very affected by usual metrics of their quality: if one prepares an $N = 10^6$ point pattern with $S(k) = 10^{-50}$ at small k [10], on average, losing or adding a single point will bounce that value up to $f \approx f' \approx 10^{-6}$, a jump by over 40 orders of magnitude! This illustrates that it is in practice unrealistic to achieve features lower than $1/N$ in $S(\boldsymbol{k})$ if structures are expected to be defective. High values, on the other hand, are qualitatively less affected: a peak that is N-high will remain roughly N-high after a deletion or addition of a fraction $f \ll 1$ of random points. This is illustrated with the example of gyromorphs in Fig. S13 $(b)-(c)$, where the gyromorphic peak remains visible even at large fractions of added or removed points ($f \approx 0.8$), and only asymptotically disappears as $f \to 1$. Note that the low-k behavior also becomes flatter and closer to 1 as expected.

For all 3 types of noise, the observed peak height in an example realization is compared to the corresponding analytical prediction in Fig. S13$(d)-(f)$, highlighting good agreement throughout.

All in all, for all forms of possible uncorrelated defects on the point pattern, we show that the features that survive best are features with $S(k) \gg 1$. As a result, gyromorphs are, in a sense, the best possible structures to resist noise. Furthermore, note that all types of uncorrelated noises level the structure factor back to the Poisson value. This is an extra indication that gyromorphs are not, as one might fear from their large-k behavior, "just" noisy quasicrystals: if they were, their peaks would necessarily be lower than those of quasicrystals, and we showed in main text that they are in fact higher.

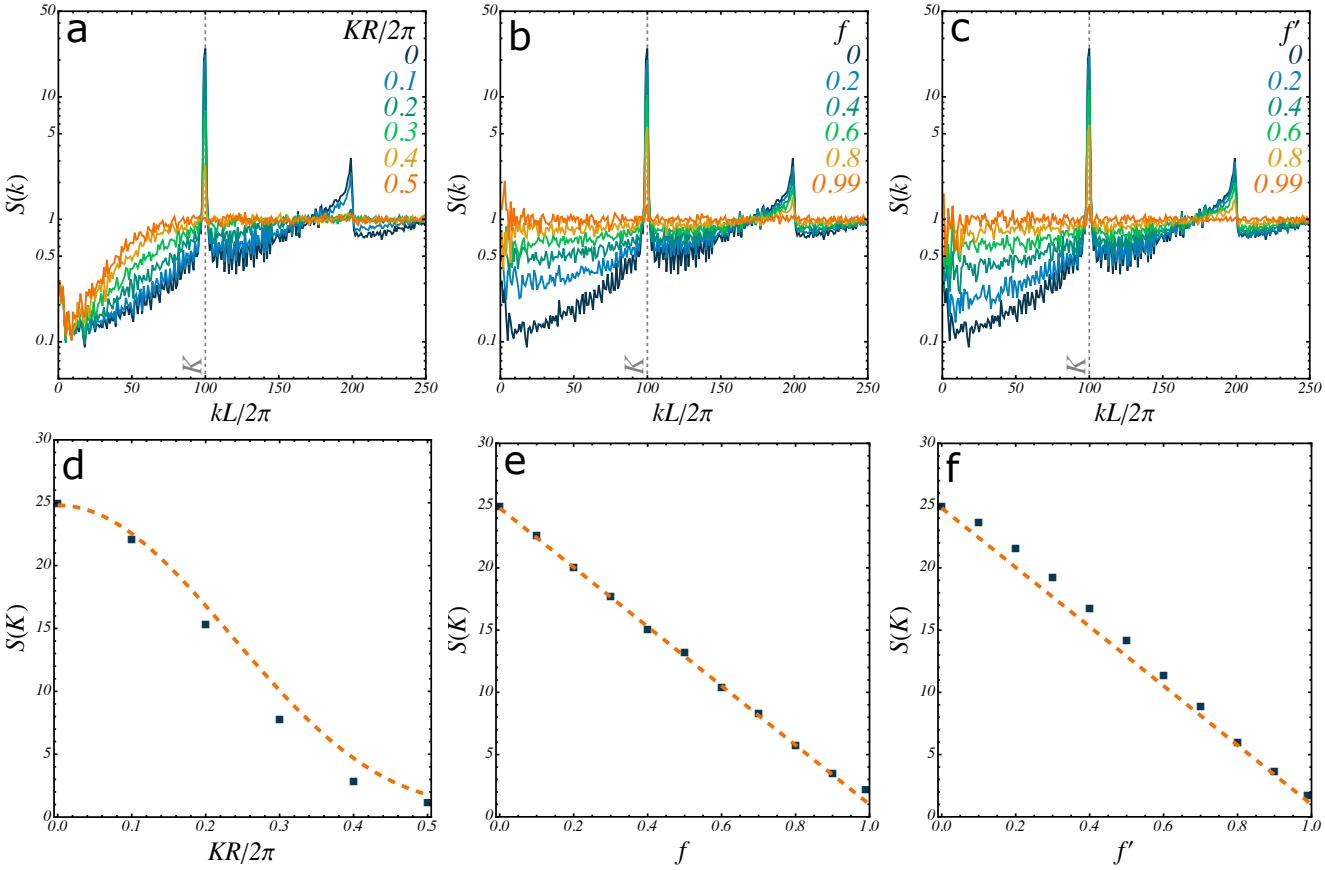


FIG. S13. **Noisy gyromorphs.** Evolution of the structure factor of a 200-fold gyromorph with $K = 100$ ($N \sim 10^4$) when subjected to noise. (a) Points are kicked at random uniformly within a disk with radius R. The kick size grows from 0 (dark blue) to $R = K/2$ (orange), corresponding to a disk with a diameter equal to the typical interparticle spacing. (b) Poisson-distributed points are added to the same gyromorph, with a final fraction f of added points. (c) Random uncorrelated deletions are performed, with a fraction of deletions f' (d) – (f) Corresponding evolutions of the peak height. Measured values in single realizations (dark blue squares) are compared to predictions for the average (dashed orange lines).

D. Diversity of solutions

In this section, we discuss the differences between solutions reached by our algorithm. To quantify the similarity between point patterns, we introduce an overlap metric

$$O[\rho_1, \rho_2] \equiv \frac{\langle \rho_1 | \rho_2 \rangle}{\sqrt{\langle \rho_1 | \rho_1 \rangle \langle \rho_2 | \rho_2 \rangle}}, \tag{S40}$$

where we introduced a scalar product

$$\langle \rho_1 | \rho_2 \rangle \equiv \int_{\mathbb{R}^d} d^d \boldsymbol{r} \widetilde{\rho}_1(\boldsymbol{r}) \widetilde{\rho}_2(\boldsymbol{r}), \tag{S41}$$

that involves the density fields convolved by a narrow Gaussian

$$\widetilde{\rho}(\boldsymbol{r}) \equiv \sum_{n=1}^{N} c_n e^{(\boldsymbol{r}-\boldsymbol{r}_n)^2/2\sigma^2}. \tag{S42}$$

The overlap O can be evaluated efficiently by performing the convolution of the point pattern by a Gaussian in Fourier space. By construction, O is non-negative and becomes asymptotically 0 for point patterns with no overlapping points, and 1 for identical point patterns. In practice, we use FINUFFT and, for a gyromorph with peaks at K, compute the FFT up for $N_k = 50 * KL/2\pi$ modes, and set σ such that $\sigma = 1/(10K)$.

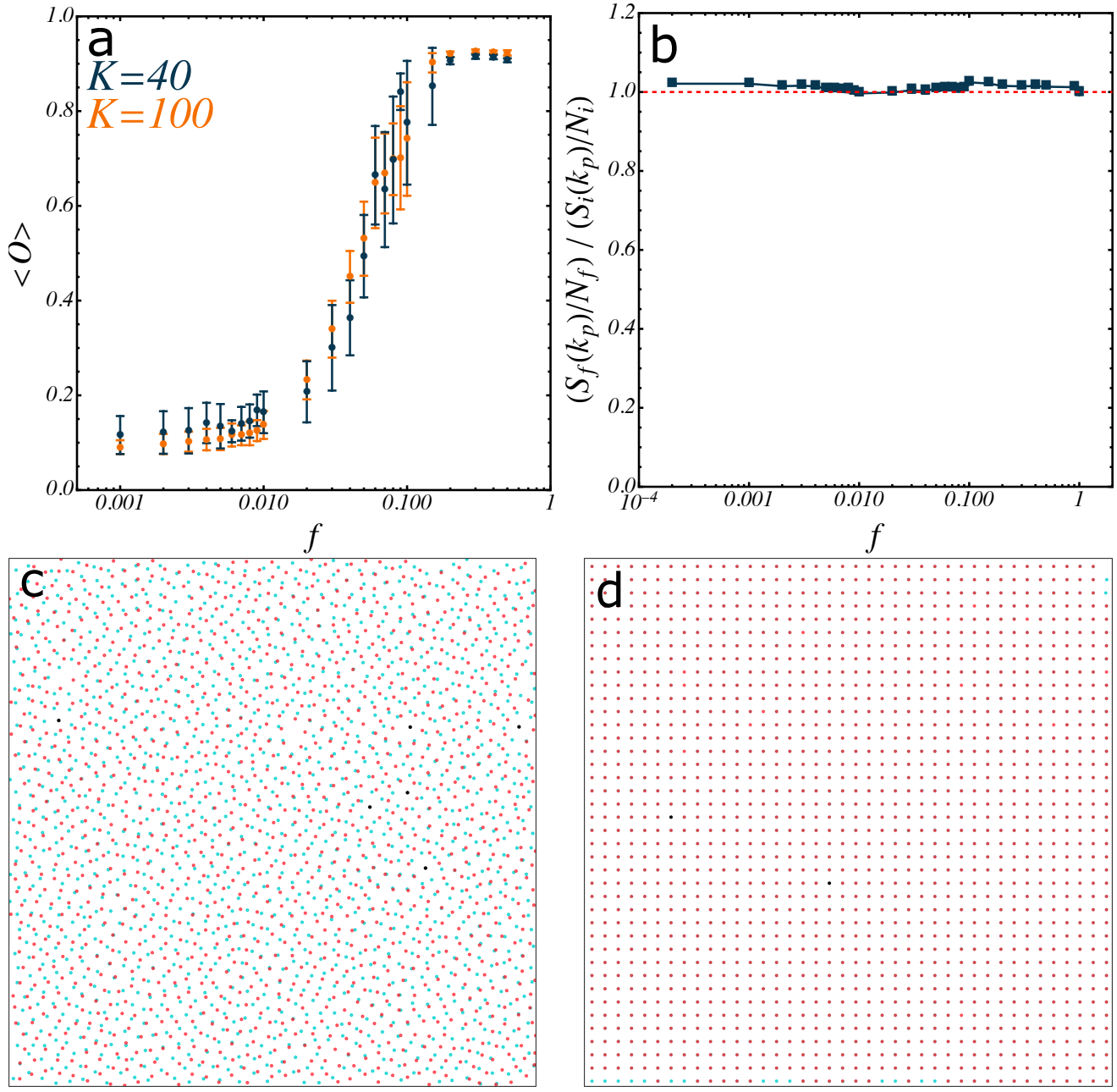


FIG. S14. **Similarity across minima.** (*a*) Averaged overlap across minimizations against fraction of pinned points, in log-linear scales, for $G = 60$. The overlap is averaged over 10 realizations using the same initial configuration but random sets of pinned points. The same operation is performed for $K = 40$ ($N \sim 1000$) and $K = 100$ ($N \sim 10^4$). Error bars are Student 95% confidence intervals. (*b*) Ratio of the final peak heights to initial peak heights, normalized by the ratio of number of points before and after repopulation. A dashed red line indicates 1. (*c*) Example realization for $K = 40$, $G = 60$, pinning $f = 5 \times 10^{-3}$ points. The pinned points are shown in black, the starting gyromorph in blue and the final gyromorph in red. (*d*) Example realization following the same recipe for $G = 4$ (square lattice) and pinning only 2 random points.

In order to obtain comparable point patterns and measure a meaningful overlap, we consider the following experiment: we generate a gyromorph for a given G and K. Then, we pin a randomly selected fraction f of the points and freeze their positions, but redraw the complementary fraction $1-f$ uniformly at random in the system and reminimize loss by adjusting the positions of these points only, using the same algorithm. We thus obtain collections of different gyromorphs with a set of fixed points, and we compute O using only the density field $\rho_f(\boldsymbol{r})$ containing the set of $(1-f)N$ points that were free to move. The reported quantity therefore quantifies how similar the final reminimized positions of the free points are across realizations, in the spirit of point-to-set measurements of configurational entropy

in glasses [30]. We show the results in Fig. S14(a) for 60-fold gyromorphs at two sizes, $K = 40$ ($N \sim 10^3$) and $K = 100$ ($N \sim 10^4$). Starting from a unique gyromorph, for each value of f the overlap is averaged over 10 realizations with different random pinned points. In panel (b), we show the ratios of the final peak heights S_f to initial peak heights S_i, normalized by the ratio of number of points before and after repopulation, N_i and N_f respectively. We show that the peak height is essentially not affected throughout, so that every repopulated configuration is a gyromorph as good as the starting one. An example realization for $K = 40$, $f = 5 \times 10^{-3}$ is shown in Fig. S14(c), highlighting the differences between the old (blue) and new (red) configurations for a set of pinned (black) points. The curves show that the overlap is low at small fractions of pinned particles, and grows to values close to 1 later on. Note that they do not finish strictly at 1 as there can be equivalent sites after point removals even at rather large f. The overlap value at a given f does not seem to change significantly when the system size is changed, meaning that one needs to fix a subset $\mathcal{O}(N)$ of the points to obtain a similar configuration, as opposed to a fixed number of points independent of L. This is in contrast with lattices, as illustrated in Fig. S14(d) by using our algorithm in the case $G = 4$, which yields perfect square lattices – by pinning only 2 points, thus removing translational invariance from the problem, the whole lattice is perfectly recovered up to boundary effects.

All in all, this experiment shows that gyromorphs are not simply deterministic patterns like crystals or de Bruijn quasicrystals, as these would be perfectly determined by a fixed number of points. Instead, a variety of gyromorphs can be obtained even when setting an extensive fraction of the points to the same locations.

E. Gyromorphs do not form continuous families

Looking at Fig. S14, one may wonder whether the configurations found by pinning subsets of the particles could be linked by continuous deformations of the point patterns that would not affect the peak heights. In other words, considering the minimization part of our algorithm only, one may wonder whether the Hessian of the loss has non-trivial flat directions at minima. In order to check, we first derive the expression of the Hessian of the FReSCo part of the loss, Eq. 1. Each $d \times d$ block H_{mn} of the Hessian matrix is defined by

$$\overline{\overline{H}}_{mn}(\boldsymbol{r_1}, \dots, \boldsymbol{r}_N) \equiv \frac{\partial^2 L_{\mathrm{NUwNU}}}{\partial \boldsymbol{r}_m \otimes \partial \boldsymbol{r}_n}(\boldsymbol{r_1}, \dots, \boldsymbol{r}_N), \tag{S43}$$

where $\otimes$ represents an outer product and we introduce a short-hand notation for the double outer derivative. Using the expression of the loss, a $d \times d$ tensor element of the Hessian can be written at any point as

$$\overline{\overline{H}}_{mn} = 2 \sum_{p=1}^{G/2} \left[\frac{\partial^2 S(\boldsymbol{k}_p)}{\partial \boldsymbol{r}_m \otimes \partial \boldsymbol{r}_n} (S(\boldsymbol{k}_p) - S_0(\boldsymbol{k}_p)) + \frac{\partial S(\boldsymbol{k}_p)}{\partial \boldsymbol{r}_m} \otimes \frac{\partial S(\boldsymbol{k}_p)}{\partial \boldsymbol{r}_n} \right]. \tag{S44}$$

The relevant derivatives of S can be written in terms of the Fourier transform of the density field, $\widehat{\rho}$ and its complex conjugate $\widehat{\rho}^\dagger$, recalling that $S \equiv |\widehat{\rho}|^2/N$,

$$\frac{\partial S(\boldsymbol{k})}{\partial \boldsymbol{r}_n} = \frac{2}{N} \mathrm{Re} \left[\widehat{\rho}(\boldsymbol{k}) \frac{\partial \widehat{\rho}^\dagger}{\partial \boldsymbol{r}_n}(\boldsymbol{k}) \right], \tag{S45}$$

$$\frac{\partial^2 S(\boldsymbol{k})}{\partial \boldsymbol{r}_m \otimes \partial \boldsymbol{r}_n} = \frac{2}{N} \mathrm{Re} \left[\frac{\partial \widehat{\rho}}{\partial \boldsymbol{r}_m}(\boldsymbol{k}) \otimes \frac{\partial \widehat{\rho}^\dagger}{\partial \boldsymbol{r}_n}(\boldsymbol{k}) + \widehat{\rho}(\boldsymbol{k}) \frac{\partial^2 \widehat{\rho}^\dagger}{\partial \boldsymbol{r}_m \otimes \partial \boldsymbol{r}_n}(\boldsymbol{k}) \right]. \tag{S46}$$

Finally, we introduce a general form for the density field like in Ref. 1,

$$\rho(\boldsymbol{r}) \equiv \sum_{n=1}^{N} c_n \delta(\boldsymbol{r} - \boldsymbol{r}_n) \tag{S47}$$

with $c_n \in \mathbb{C}$, and define our Fourier transform such that

$$\widehat{\rho}(\boldsymbol{k}) = \sum_{n=1}^{N} c_n e^{i\boldsymbol{k}\cdot\boldsymbol{r}_n}. \tag{S48}$$

Injecting the expression of $\widehat{\rho}$ into the derivatives of S leads to

$$\frac{\partial S(\boldsymbol{k})}{\partial \boldsymbol{r}_m} \otimes \frac{\partial S(\boldsymbol{k})}{\partial \boldsymbol{r}_n} = \frac{-2\boldsymbol{k} \otimes \boldsymbol{k}}{N^2} \mathrm{Re} \left[\widehat{\rho}^2 c_m^\dagger c_n^\dagger e^{-i\boldsymbol{k}\cdot(\boldsymbol{r}_m + \boldsymbol{r}_n)} - |\widehat{\rho}|^2 c_m^\dagger c_n e^{-i\boldsymbol{k}\cdot(\boldsymbol{r}_m - \boldsymbol{r}_n)} \right], \tag{S49}$$

$$\frac{\partial^2 S(\boldsymbol{k})}{\partial \boldsymbol{r}_m \otimes \partial \boldsymbol{r}_n} = \frac{2\boldsymbol{k} \otimes \boldsymbol{k}}{N} \mathrm{Re} \left[c_m^\dagger c_n e^{-i\boldsymbol{k}\cdot(\boldsymbol{r}_m - \boldsymbol{r}_n)} - \delta_{m,n} \widehat{\rho}\, c_n^\dagger e^{-i\boldsymbol{k}\cdot\boldsymbol{r}_n} \right], \tag{S50}$$

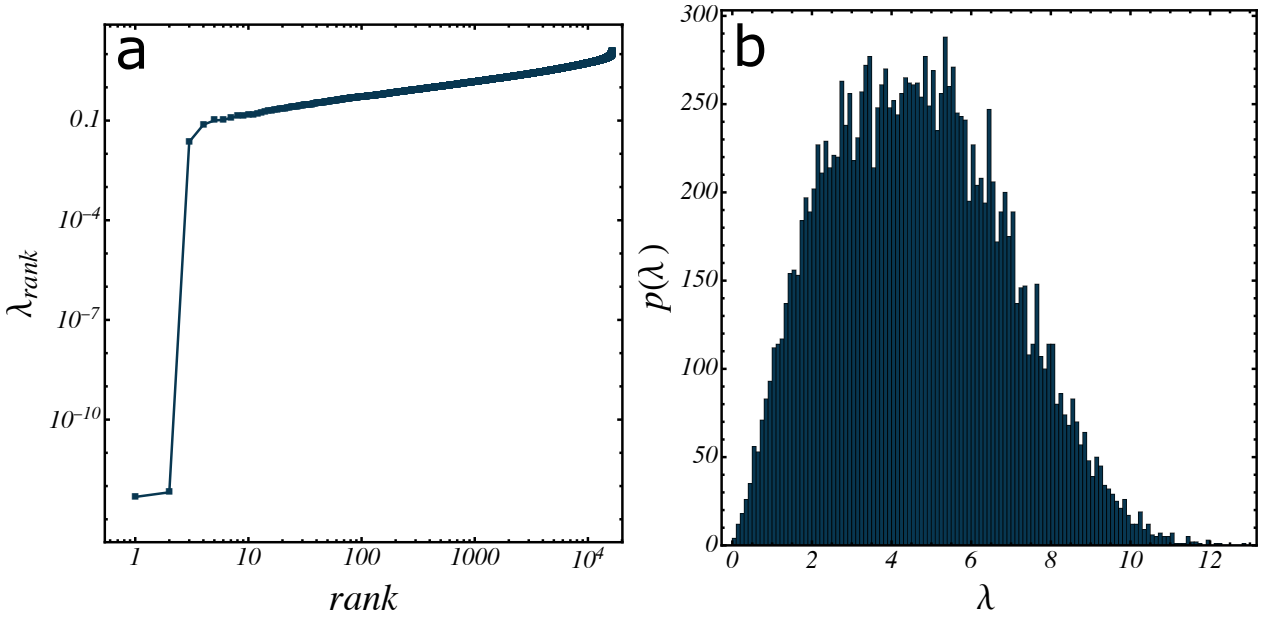


FIG. S15. **Spectrum of the FReSCo Hessian at a minimum.** (*a*) Value of sorted eigenvalues against their rank, in log-log. (*b*) Histogram of eigenvalues. Both plots are obtained for a $G = 60$ gyromorph with $N \sim 8000$ points.

where we dropped the argument of $\widehat{\rho}$, S, and S_0 to avoid clutter. Just like the gradient in FReSCo [1], the Hessian may then be written as Fourier series,

$$\overline{\overline{H}}_{mn} = \mathrm{Re}\left[\delta_{m,n}\widehat{D}_n(\boldsymbol{r}_n) + \widehat{S}_{mn}(\boldsymbol{r}_m + \boldsymbol{r}_n) + \widehat{A}_{mn}(\boldsymbol{r}_m - \boldsymbol{r}_n)\right], \tag{S51}$$

with $\widehat{D}_n$ a "diagonal" term, $\widehat{S}_{mn}$ a term that depends only on a symmetric combination of $\boldsymbol{r}_m$ and $\boldsymbol{r}_n$, and $\widehat{A}_{mn}$ one that depends only on their difference, and the hat indicates that any of the three terms is of the form

$$\widehat{T}(\boldsymbol{r}) = \sum_{\boldsymbol{k}_p} \overline{\overline{T}}(\boldsymbol{k}_p) e^{-i\boldsymbol{k}_p\cdot\boldsymbol{r}}. \tag{S52}$$

The expressions of the corresponding Fourier coefficents (analogues of $T(\boldsymbol{k}_p)$) read

$$\overline{\overline{D}}_n(\boldsymbol{k}) \equiv -\frac{4\boldsymbol{k}\otimes\boldsymbol{k}}{N}\widehat{\rho}(\boldsymbol{k})c_n^\dagger(S(\boldsymbol{k}) - S_0(\boldsymbol{k})), \tag{S53}$$

$$\overline{\overline{S}}_{mn}(\boldsymbol{k}) \equiv -\frac{4\boldsymbol{k}\otimes\boldsymbol{k}}{N^2}\widehat{\rho}^2(\boldsymbol{k})c_m^\dagger c_n^\dagger, \tag{S54}$$

$$\overline{\overline{A}}_{mn}(\boldsymbol{k}) \equiv \frac{4\boldsymbol{k}\otimes\boldsymbol{k}}{N}c_m^\dagger c_n(2S(\boldsymbol{k}) - S_0(\boldsymbol{k})). \tag{S55}$$

The algorithm of Fig. S2 is not just a minimization, as it contains cycles of particle removals and reinsertions. Thus, to compute the Hessian at a meaningful point, we start from a configuration generated by our algorithm, then we reminimize the FReSCo part of the loss alone (without the variance part), remove overlapping points, and repeat the procedure until N stabilizes, then evaluate the Hessian there. Note that this is *not* our usual recipe as this one, while it generates true minima of a loss function, also has more short-range density fluctuations, which is often argued to be bad for optics [13]. The relevant part of the obtained Hessian is its spectrum. We perform an eigendecomposition and report the eigenvalues for $G = 60$ and $K = 100$ in Fig. S15(*a*), where they are sorted by increasing order. The relevant information is that 2 eigenvalues are much smaller than the rest – we check that they correspond to global translations, which leave the loss invariant. The next eigenvalues are orders of magnitude larger, and form the first bin of a smooth distribution of positive values, whose histogram is shown in Fig. S15(*b*). This shows that gyromorphs may not be obtained from each other via smooth deformations without making the gyromorph worse in intermediate stages.

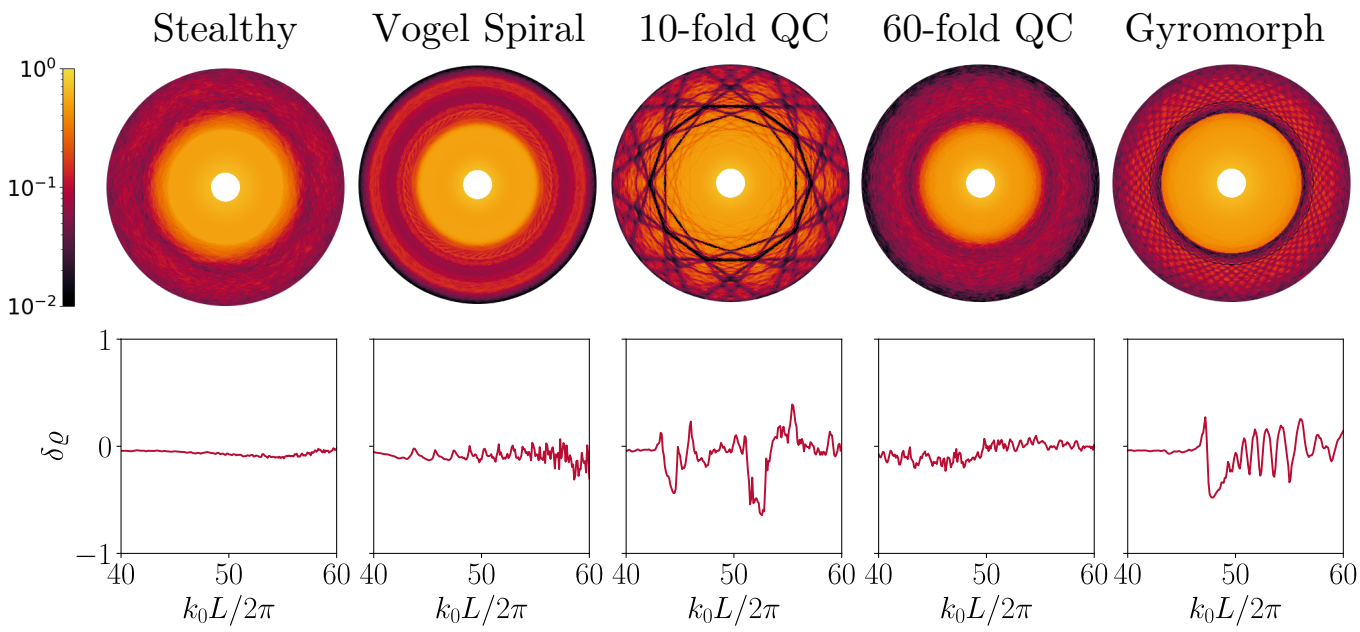


FIG. S16. **Scalar-wave results** Transmission plots (top) and density of states (bottom) of incident scalar-waves for five $2d$ systems. In the whole figure, $\phi = 5\%$, $n = 1.5$.

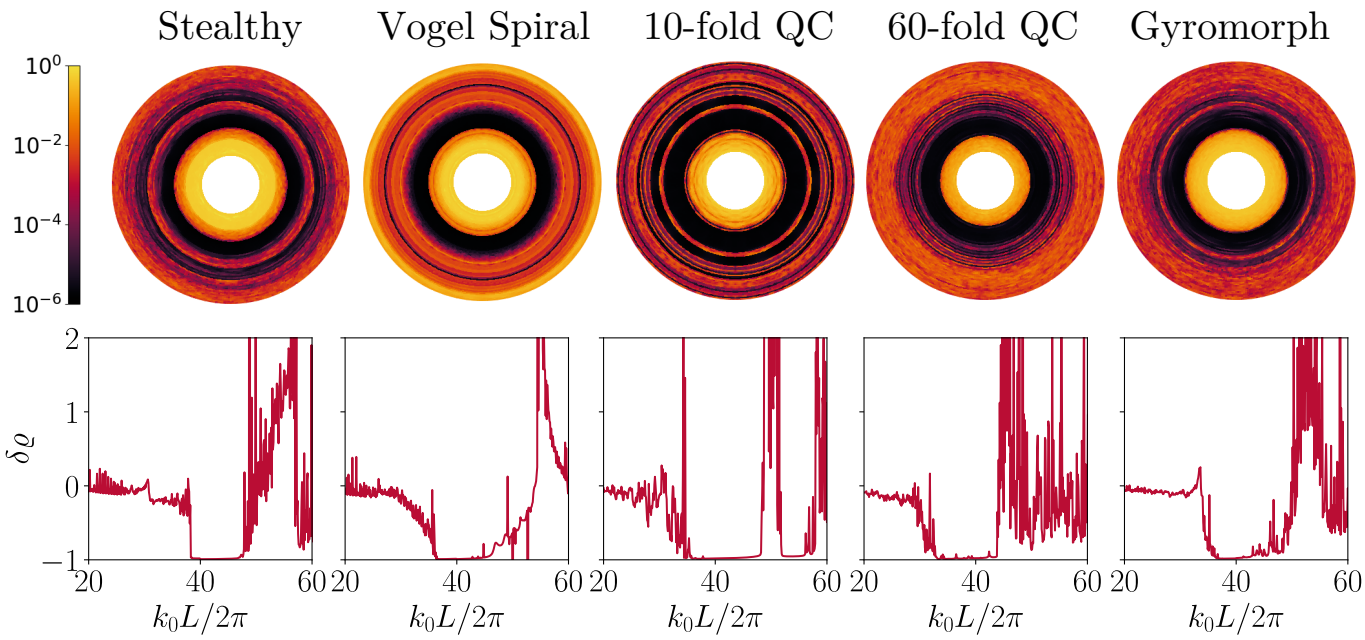


FIG. S17. **Scalar-wave results** Transmission plots (top) and density of states (bottom) of incident scalar-waves for five $2d$ systems. In the whole figure, $\phi = 5\%$, $n = 3$.

IV. ADDITIONAL DATA ON OPTICAL BEHAVIOR

A. Scalar-wave results

In the main text, we focus on vector wave results. We here show corresponding results for scalar waves, which have been the focus of most past works as bandgaps are much easier to achieve in scalar waves [2, 3, 11, 31]. First, in Fig. S16, we show results for $2d$ scalar waves ("TM polarization") for parameters leading to curves with a similar

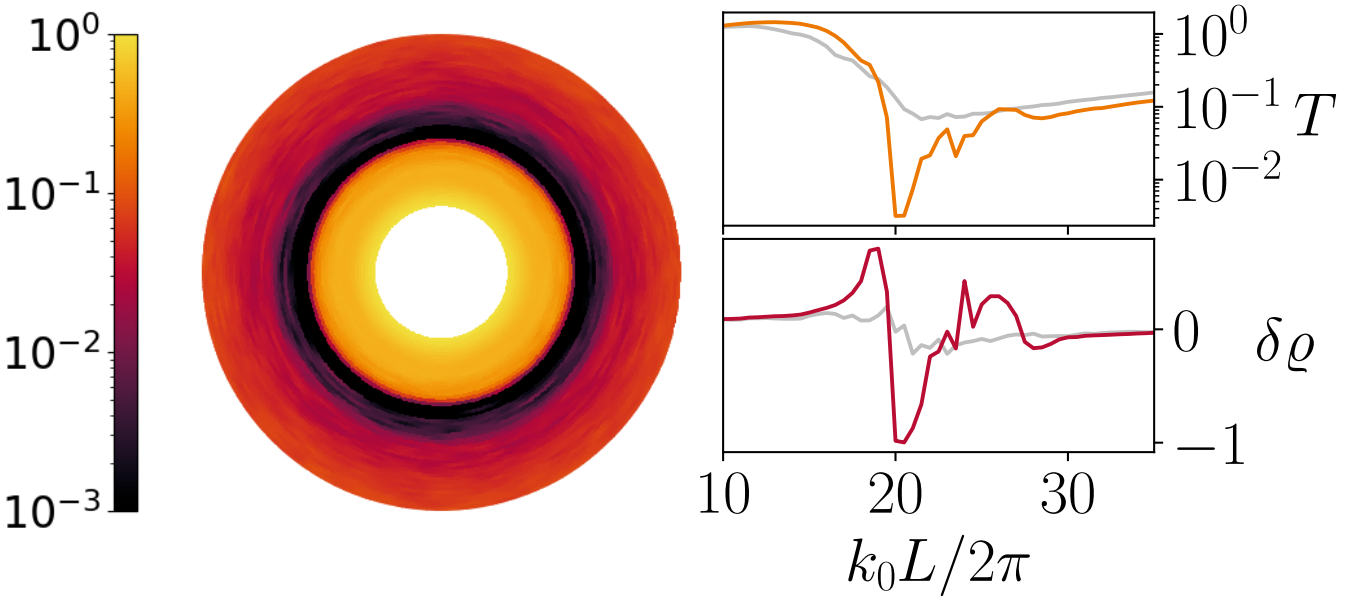


FIG. S18. **Scalar-wave results for 3d gyromorph** Transmission plot (left) for the 3d gyromorph. Radially averaged transmission (upper right) and density of states (lower right) of incident scalar-waves for the 3d gyromorph (orange, red lines) and a 3d poisson point pattern (gray lines). In the whole figure, $n = 3$ and $\phi = 10\%$.

aspect compared to the vector waves ("TE polarization") of the main text, namely $\phi = 5\%$ and $n = 1.5$, for the same systems as in the main text. The results closely resemble the TE ones: the deeper features in transmission and LDOS variation are for gyromorphs and low-order quasicrystals, and gyromorphs are more isotropic than the latter. In Fig, S17, we show the same quantities, but this time for the same parameters as in the main text, namely $\phi = 5\%$ and $n = 3$. This time, because the TM response is typically stronger than the TE one, a clear deep gap develops for all systems, as expected from past works. The transmission gap is wider, and has weaker extra features, than its counterparts. The DOS displays strong depletion to near-zero amounts of modes, like other systems. Finally, note that this measurement indicates "completeness" with respect to polarization of the mode depletion in gyromorphs.

In Fig. S18, we show scalar-wave results for the 3d gyromorph from the main text, again choosing the same packing fraction, but a lower index contrast than in the main text (here, $n = 3$). This response is again much stronger than in the vector-wave case.

B. Scaling of bandgap depth with physical parameters

To assess the quality of the bandgaps formed by gyromorphs, we measure the absolute DOS $\varrho = \varrho_0(1+\delta\varrho)$, averaged over points away from scatterers, for both vector and scalar waves, when varying physical parameters, L, ϕ, and n, keeping the other fixed to the values used in the main text. To vary L, following Ref. 2, we subsample from one bigger configuration with a radius that we tune. The 2d results are shown in Fig. S19. We show that the mode depletion indeed gets stronger for both polarizations as the medium gets thicker. In fact, following Refs [32, 33], we show that the decay with L is consistent with the expected $\varrho \sim 1/L$ for scalar waves, as expected in crystalline bandgaps for the TM polarization. We also report a (weaker) decay for the TE component, with an exponent $\varrho \sim 1/L^{1/4}$. The changes with ϕ and n are more subtle, but we do observe a deepening of the gap with both ϕ and n. We show nearby power laws as guides for the eyes in Fig. S19.

The same measurements are performed in 3d gyromorphs and reported in Fig. S20. We emphasize that the vector-wave results almost do not move, probably suggesting that a larger variety of L would be needed to catch any clear tendency. On the scalar side though, the DOS decreases extremely fast with L (a nearby power is L^{-7}). That fast decay could be a sign of an exponential decay, as suggested in similar measurements in a stealthy hyperuniform system in past work [2].

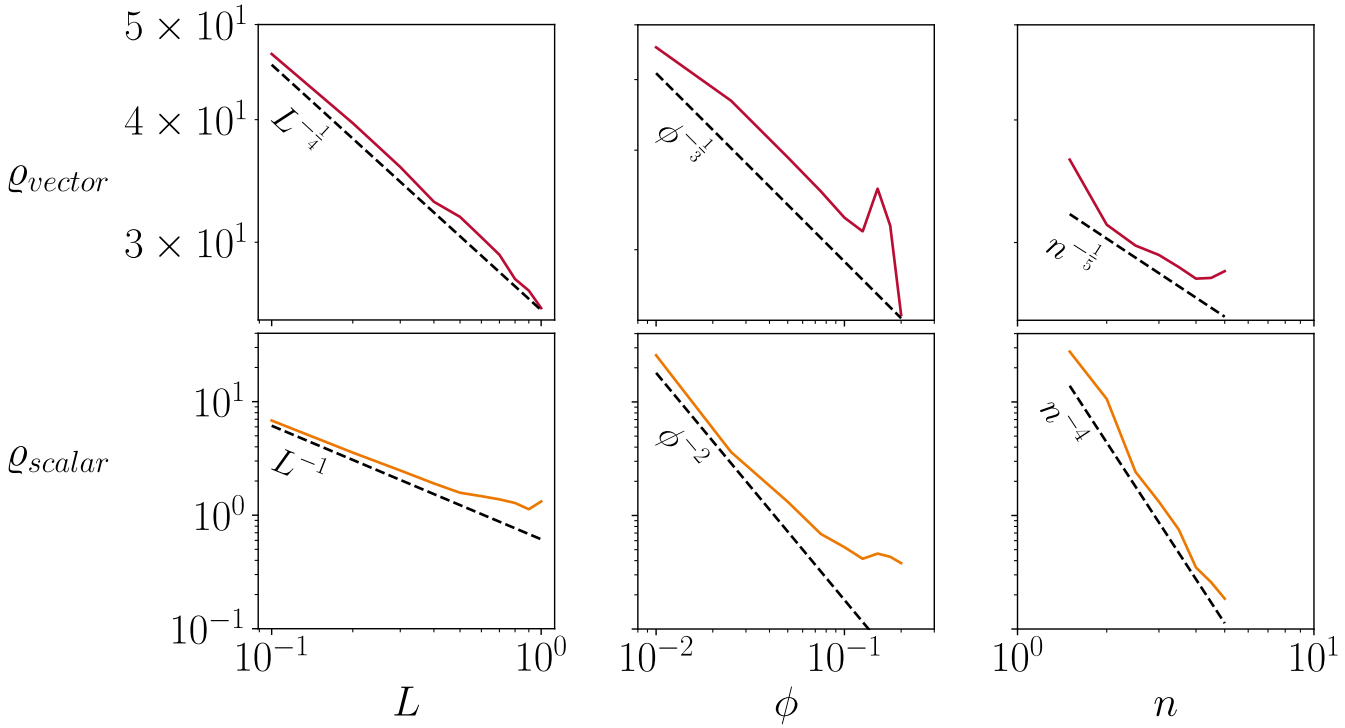


FIG. S19. **Scalings of the bandgap in the 2d 60-fold gyromorph** Absolute DOS at the deepest point of the bandgap, $\varrho = \varrho_0(\delta\varrho_{min} + 1)$, against the diameter of the subsampled medium L, the filling fraction ϕ, and the refractive index n, in log scales, for TE (red) and TM (orange) polarizations. Dashed lines indicate power-law tendencies. In the whole figure, $n = 3$ and $\phi = 5\%$ if not otherwise specified.

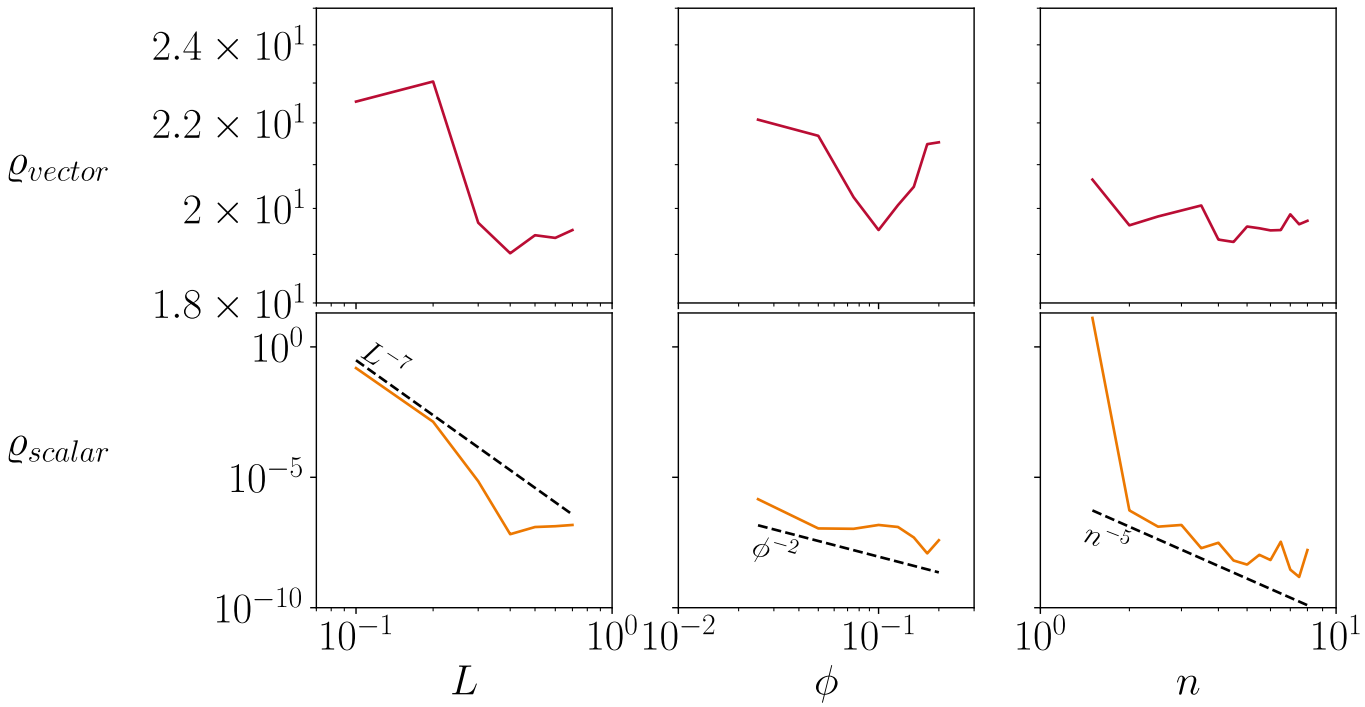


FIG. S20. **Scalings of gap in the 3d gyromorph** Absolute DOS at the deepest point of the bandgap, $\varrho = \varrho_0(\delta\varrho_{min} + 1)$, against the diameter of the subsampled medium L, the filling fraction ϕ, and the refractive index n, in log scales, for TE (red) and TM (orange) polarizations. Dashed lines indicate power-law tendencies. Dashed lines indicate results for typical bandgap forming candidates. In the whole figure, $n = 6.5$ for vector waves, $n = 3$ for scalar waves and $\phi = 10\%$ if not otherwise specified.

V. COUPLED DIPOLES METHOD

A. General Definitions

In the main text, we rely on the Coupled Dipoles Method (CDM) to describe the optical properties of gyromorphs. As the paper is aimed at a general audience that may not be familiar with light scattering, we give a pedagogical reminder of the thoery and definitions below. The starting point of the calculation is the $3d$ monochromatic Maxwell-Helmholtz equation for the electric field $\boldsymbol{E}$, at pulsation ω in a non-magnetic heterogeneous system characterized by an isotropic relative dielectric constant field $\varepsilon(\boldsymbol{r};\omega)$ [34, 35]

$$\boldsymbol{\nabla}\times\boldsymbol{\nabla}\times\boldsymbol{E}(\boldsymbol{r};\omega)-\frac{\omega^2}{c^2}\varepsilon(\boldsymbol{r};\omega)\boldsymbol{E}(\boldsymbol{r};\omega)=i\mu_0\omega\boldsymbol{j}_{ext}(\boldsymbol{r};\omega), \tag{S56}$$

where c is the speed of light in vacuum, μ_0 is the magnetic permeability of vacuum and $\boldsymbol{j}_{ext}$ is the externally imposed charge current density, that results in light sources. Following usual conventions [36], we define the incident field $\boldsymbol{E}_{inc}(\boldsymbol{r})$ as the solution of the wave equation for the same sources, but in vacuum,

$$\boldsymbol{\nabla}\times\boldsymbol{\nabla}\times\boldsymbol{E}_{inc}(\boldsymbol{r};\omega)-\frac{\omega^2}{c^2}\boldsymbol{E}_{inc}(\boldsymbol{r};\omega)=i\mu_0\omega\boldsymbol{j}_{ext}(\boldsymbol{r};\omega), \tag{S57}$$

as well as the scattered field $\boldsymbol{E}_s=\boldsymbol{E}-\boldsymbol{E}_{inc}$. The latter obeys the equation

$$\boldsymbol{\nabla}\times\boldsymbol{\nabla}\times\boldsymbol{E}_s(\boldsymbol{r};\omega)-\frac{\omega^2}{c^2}\boldsymbol{E}_s(\boldsymbol{r};\omega)=\frac{\omega^2}{c^2}\delta\varepsilon(\boldsymbol{r};\omega)\boldsymbol{E}(\boldsymbol{r};\omega), \tag{S58}$$

in which we introduced the relative dielectric contrast $\delta\varepsilon=\varepsilon-1$. To go further, we introduce the *dyadic Green's function* [36, 37], $\overline{\overline{G}}_0(\boldsymbol{r},\boldsymbol{r'};\omega)$, associated to propagation in free space. This 3×3 rank-2 tensor is defined as the solution of the free-space Maxwell-Helmholtz equation when the source is replaced by a Dirac delta in each direction,

$$\boldsymbol{\nabla}\times\boldsymbol{\nabla}\times\overline{\overline{G}}_0(\boldsymbol{r},\boldsymbol{r'};\omega)-\frac{\omega^2}{c^2}\overline{\overline{G}}_0(\boldsymbol{r},\boldsymbol{r'};\omega)=\delta(\boldsymbol{r}-\boldsymbol{r'})\overline{\overline{I}}, \tag{S59}$$

with $\overline{\overline{I}}$ the identity tensor. Defining the Green tensor enables to write any field propagating in vacuum as an integral equation over the source term. For instance, the incident field defined in Eq. 57 verifies

$$\boldsymbol{E}_{inc}(\boldsymbol{r};\omega)=i\mu_0\omega\int d^3\boldsymbol{r'}\,\overline{\overline{G}}_0(\boldsymbol{r},\boldsymbol{r'};\omega)\boldsymbol{j}_{ext}(\boldsymbol{r'};\omega). \tag{S60}$$

More importantly, writing the analogue equation for the scattered field, Eq. 58, leads to the Lippman-Schwinger equation [36],

$$\boldsymbol{E}(\boldsymbol{r};\omega)=\boldsymbol{E}_{inc}(\boldsymbol{r};\omega)+\frac{\omega^2}{c^2}\int d^3\boldsymbol{r'}\,\overline{\overline{G}}_0(\boldsymbol{r},\boldsymbol{r'};\omega)\delta\varepsilon(\boldsymbol{r'};\omega)\boldsymbol{E}(\boldsymbol{r'};\omega). \tag{S61}$$

In this paper, we study propagation through media composed of N discrete scatterers, each with homogeneous dielectric contrasts $\delta\varepsilon_i$, placed at positions $\boldsymbol{r}_i$, in a homogeneous medium that can be assumed to be vacuum, leading to

$$\boldsymbol{E}(\boldsymbol{r};\omega)=\boldsymbol{E}_{inc}(\boldsymbol{r};\omega)+\frac{\omega^2}{c^2}\sum_{i=1}^{N}\delta\varepsilon_i(\omega)\int_{V_i}d^3\boldsymbol{r'}\,\overline{\overline{G}}_0(\boldsymbol{r},\boldsymbol{r'};\omega)\boldsymbol{E}(\boldsymbol{r'};\omega), \tag{S62}$$

with V_i the volume of scatterer i. Up until this point, all equations were exact. We henceforth introduce a version of the discrete dipole approximation (DDA) [38]: we assume that each scatterer is smaller than a wavelength, $\omega a/(2\pi c)\ll1$ with a the typical size of scatterers. In this regime, the field component at ω is well approximated by the field at the center of the scatterer, so that

$$\boldsymbol{E}(\boldsymbol{r};\omega)\approx\boldsymbol{E}_{inc}(\boldsymbol{r};\omega)+\frac{\omega^2}{c^2}\sum_{i=1}^{N}\left[\int_{V_i}d^3\boldsymbol{r'}\,\overline{\overline{G}}_0(\boldsymbol{r},\boldsymbol{r'};\omega)\right]\delta\varepsilon_i(\omega)\boldsymbol{E}(\boldsymbol{r}_i;\omega). \tag{S63}$$

This equation is useful in two scenarios [36, 39–42]. First, it can be used to evaluate the field outside of scatterers, which only requires the knowledge of the incident field and of the field at every scatterer. In that case, the expression

above can be further approximated by taking only the leading contribution of the integral in the limit of small scatterers,

$$\boldsymbol{E}(\boldsymbol{r};\omega) \approx \boldsymbol{E}_{inc}(\boldsymbol{r};\omega) + \frac{\omega^2}{c^2}\sum_{i=1}^{N} V_i \delta\varepsilon_i(\omega)\overline{\overline{G}}_0(\boldsymbol{r},\boldsymbol{r_i};\omega)\boldsymbol{E}(\boldsymbol{r}_i;\omega). \tag{S64}$$

Second, the same equation can be applied at the center of a scatterer, yielding a set of equations of the form

$$\boldsymbol{E}(\boldsymbol{r}_j;\omega) \approx \boldsymbol{E}_{inc}(\boldsymbol{r_j};\omega) + \frac{\omega^2}{c^2}\sum_{j\neq i}^{N} V_i \delta\varepsilon_i(\omega)\overline{\overline{G}}_0(\boldsymbol{r}_j,\boldsymbol{r_i};\omega)\boldsymbol{E}(\boldsymbol{r}_i;\omega) + \frac{\omega^2}{c^2}\delta\varepsilon_j(\omega)\left[\int_{V_j} d^3\boldsymbol{r'}\,\overline{\overline{G}}_0(\boldsymbol{r_j},\boldsymbol{r'};\omega)\right]\boldsymbol{E}(\boldsymbol{r}_j;\omega), \tag{S65}$$

where the last term, that encodes a self-induction effect at scatterer j, has to be computed differently from other terms in the sum due to the singularity of the Green's function of free space at $\boldsymbol{r} = \boldsymbol{r'}$. Once this integral is computed, one finds a system of N linear equations between the fields at the centers of scatterers, which can be solved frequency by frequency for any choice of incident field. For future convenience, we introduce $k_0 = \omega/c$ the wave number in free space, $\alpha_i(\omega) = V_i\delta\epsilon_i(\omega)$ the bare polarizability of scatterers, $\mathcal{E}(\{\boldsymbol{r}_i\};\omega) = (\boldsymbol{E}(\boldsymbol{r}_1;\omega),\ldots,\boldsymbol{E}(\boldsymbol{r}_N;\omega))$ the vector of electric fields at scatterers, $\mathcal{E}_{inc}(\{\boldsymbol{r}_i\};\omega)$ the corresponding vector of incident fields, and $\mathcal{M}(\{\boldsymbol{r}_{ij}\};\omega)$ the matrix that verifies

$$\mathcal{M}(\{\boldsymbol{r}_{ij}\};\omega)\cdot\mathcal{E}(\{\boldsymbol{r}_j\};\omega) = \mathcal{E}_{inc}(\{\boldsymbol{r}_i\};\omega), \tag{S66}$$

with $\cdot$ indicating a matrix multiplication. Notice that in our notations, $\mathcal{M}(\{\boldsymbol{r}_{ij}\};\omega)$ is an $N\times N$ matrix of 3×3 tensors, $\mathcal{M}_{ij} \equiv \overline{\overline{M}}(\boldsymbol{r}_i,\boldsymbol{r_j};\omega)$. In the simple cases of identical scatterers, $\alpha_i(\omega) = \alpha(\omega)$, the matrix above can be decomposed by introducing the *Green matrix* [33, 43] $\mathcal{G}$, which verifies

$$\mathcal{M}(\{\boldsymbol{r}_{ij}\};\omega) = \mathcal{I} - k_0^2\alpha(\omega)\mathcal{G}(\{\boldsymbol{r}_{ij}\};\omega), \tag{S67}$$

with $\mathcal{I}$ a diagonal $N\times N$ matrix of 3×3 identity tensors. With these notations, it clearly appears that solving the linear system in Eq. 65 is tantamount to computing the inverse $\mathcal{W}\equiv\mathcal{M}^{-1}$, a task that can be achieved numerically by encoding it as a $3N\times 3N$ matrix. Through Eq. 64, this solution is enough to reconstruct the full electric field in all of space. Note that this approach is not strictly limited to small scatterers: one can approximate any large scatterer by a collection of voxels with a size smaller than the considered lengthscale, and solve the system above [38].

Let us now focus on self-interaction. Consider a single small scatterer centered at $\mathbf{0}$ in an incident field,

$$\boldsymbol{E}(\mathbf{0};\omega) = \boldsymbol{E}_{inc}(\mathbf{0};\omega) + \frac{\omega^2}{c^2}\delta\varepsilon(\omega)\overline{\overline{S}}(\omega)\boldsymbol{E}(\mathbf{0};\omega), \tag{S68}$$

where $\overline{\overline{S}}$ denotes the self-interaction term,

$$\overline{\overline{S}} \equiv \left[\int_V d^3\boldsymbol{r'}\,\overline{\overline{G}}_0(\boldsymbol{r_j},\boldsymbol{r'};\omega)\right] \tag{S69}$$

For scalar dielectric constants such as the ones considered here (*i.e.* non-birefringent media), the self-interaction is a diagonal tensor $\overline{\overline{S}} = S\overline{\overline{I}}$. One may write the value of the polarization field at the center of the particle, defined as α_0 multiplied by the total field there, and express it as a response to the incident field instead,

$$\boldsymbol{P}(\mathbf{0};\omega) \equiv \alpha_0(\omega)\boldsymbol{E}(\mathbf{0};\omega) = \alpha_d(\omega)\boldsymbol{E}_{inc}(\mathbf{0};\omega) \tag{S70}$$

with α_d a *dressed* polarizability that accounts for self-interaction. Using the diagonal nature of $\overline{\overline{S}}$, this yields an expression for the dressed polarizability,

$$\alpha_d(\omega) = \frac{\alpha_0(\omega)}{1 - k_0^2\alpha_0(\omega)S/V}. \tag{S71}$$

This polarizability describes the true response of the scatterer to an incident field, which takes into account its finite size and leads to resonant behaviour. More importantly, neglecting self-interaction, which is equivalent to considering $\alpha_d = \alpha_0$, leads to violations of the optical theorem, which encodes energy conservation at scattering events [36]. In some works [3, 41, 42, 44–46], the self-interaction is not written explicitly into the linear problem that is being solved.

It is because the linear problem can be rewritten in terms of dressed polarizabilities (*i.e.* the vertices of the diagrams in the Born expansion are renormalized),

$$\boldsymbol{E}(\boldsymbol{r}_j;\omega) \approx \boldsymbol{E}_{inc}(\boldsymbol{r_j};\omega) + k_0^2 \sum_{j\neq i}^{N} \alpha_{d,i}(\omega)\overline{\overline{G}}_0(\boldsymbol{r}_j,\boldsymbol{r_i};\omega)\boldsymbol{E}(\boldsymbol{r}_i;\omega), \tag{S72}$$

so that the matrix in Eq. 67 is replaced by

$$\mathcal{M}_d(\{\boldsymbol{r}_{ij}\};\omega) = \mathcal{I} - k_0^2\alpha_d(\omega)\mathcal{G}_d(\{\boldsymbol{r}_{ij}\};\omega), \tag{S73}$$

with $\mathcal{G}_d^{iiab} = 0$, for all particle indices i and coordinate pairs $a, b \in \{x, y, z\}^2$.

It is customary to characterize structured dielectric media by a *density of states* (DOS) for the medium, which quantifies the number of electromagnetic modes that are allowed to propagate through it at a given frequency [2, 31, 47, 48]. The quantity that is easily accessible when using a Green's function formalism is the *local* density of states (LDOS), $\varrho(\boldsymbol{r},\omega)$ at a given position $\boldsymbol{r}$ and around pulsation ω. While its expression is not original to this paper, past works typically resort to a different set of approximations than us to model cold atomic vapors rather than soft materials [3, 33, 36, 37, 41, 49, 50], so that we here reproduce our computation to avoid possible confusions. The starting point of the calculation is that the local density of states of a lossless material placed in a cavity can be written as [36]

$$\varrho(\boldsymbol{r},\omega) = \frac{2\omega}{\pi c^2}\mathrm{Im}\left[\mathrm{Tr}_3\overline{\overline{G}}(\boldsymbol{r},\boldsymbol{r};\omega)\right], \tag{S74}$$

where Im denotes the imaginary part, Tr_3 the trace over the 3 diagonal elements of a rank-2 tensor, and $\overline{\overline{G}}$ is the Green's function of the medium, defined through

$$\boldsymbol{\nabla}\times\boldsymbol{\nabla}\times\overline{\overline{G}}(\boldsymbol{r},\boldsymbol{r'};\omega) - \frac{\omega^2}{c^2}\varepsilon(\boldsymbol{r},\omega)\overline{\overline{G}}(\boldsymbol{r},\boldsymbol{r'};\omega) = \delta(\boldsymbol{r}-\boldsymbol{r'})\overline{\overline{I}}. \tag{S75}$$

This definition ensures that the *full* field obeys the equation

$$\boldsymbol{E}(\boldsymbol{r};\omega) = i\mu_0\omega\int d^3\boldsymbol{r'}\,\overline{\overline{G}}(\boldsymbol{r},\boldsymbol{r'};\omega)\boldsymbol{j}_{ext}(\boldsymbol{r'};\omega). \tag{S76}$$

In particular, one can choose, a point-electric dipole source with moment $\boldsymbol{p}$ placed at $\boldsymbol{r}_d$, corresponding to

$$\boldsymbol{j}_{ext}(\boldsymbol{r};\omega) \equiv -i\omega\boldsymbol{p}\delta(\boldsymbol{r}-\boldsymbol{r}_d). \tag{S77}$$

For this specific choice of source (but without any loss of generality), using Eqs. 57, 76, 64, and $\mu_0\varepsilon_0c^2 = 1$, one can write $\overline{\overline{G}}$ when the observation point $\boldsymbol{r}$ is not inside a scatterer as

$$\overline{\overline{G}}(\boldsymbol{r},\boldsymbol{r'};\omega) = \overline{\overline{G}}_0(\boldsymbol{r},\boldsymbol{r'};\omega) + k_0^2\alpha(\omega)\sum_{j,l=1}^{N}\overline{\overline{G}}_0(\boldsymbol{r},\boldsymbol{r}_j;\omega)\overline{\overline{W}}_{jl}\overline{\overline{G}}_0(\boldsymbol{r}_l,\boldsymbol{r'};\omega), \tag{S78}$$

where we introduced $\overline{\overline{W}}_{jl}$ the jl-th $(d\times d)$-tensor element of matrix $\mathcal{W}\equiv\mathcal{M}^{-1}$. The second term of this equation, which encodes the effect of scatterers on propagation, assumes the shape of a matrix product: defining the $1\times N$ matrix $\mathcal{G}_0^{(1)}(\boldsymbol{r};\{\boldsymbol{r}_i\};\omega) = (\overline{\overline{G}}_0(\boldsymbol{r},\boldsymbol{r}_1;\omega),\ldots,\overline{\overline{G}}_0(\boldsymbol{r},\boldsymbol{r}_N;\omega))$, and the transpose operator ^{t}, one can write

$$\overline{\overline{G}}(\boldsymbol{r},\boldsymbol{r'};\omega) = \overline{\overline{G}}_0(\boldsymbol{r},\boldsymbol{r'};\omega) + k_0^2\alpha(\omega)\,\mathcal{G}_0^{(1)}(\boldsymbol{r};\{\boldsymbol{r}_i\};\omega)\cdot\mathcal{W}(\{\boldsymbol{r}_{ij}\};\omega)\cdot{}^t\mathcal{G}_0^{(1)}(\boldsymbol{r'};\{\boldsymbol{r}_j\};\omega). \tag{S79}$$

As a result, the LDOS of a system of small discrete scatterers, evaluated outside of scatterers, reads

$$\varrho(\boldsymbol{r},\omega) = \varrho_0(\omega) + \frac{2\omega^3}{\pi c^4}\mathrm{Im}\left[\alpha(\omega)\mathrm{Tr}_3\left[\mathcal{G}_0^{(1)}(\boldsymbol{r};\{\boldsymbol{r}_i\};\omega)\cdot\mathcal{W}(\{\boldsymbol{r}_{ij}\};\omega)\cdot{}^t\mathcal{G}_0^{(1)}(\boldsymbol{r};\{\boldsymbol{r}_j\};\omega)\right]\right], \tag{S80}$$

where $\varrho_0(\omega)$ is the LDOS of vacuum, which does not depend on location [36, 49].

One may also define a density of state for the medium as a whole. A straightforward definition from the LDOS is [37]

$$\varrho_{med}(\omega) = \int_{V_{med}} d^3\boldsymbol{r}\varrho(\boldsymbol{r},\omega), \tag{S81}$$

with V_{med} the volume of the region that contains scatterers. In practice, this integral can be evaluated numerically: by defining M measurement points at positions $\{\boldsymbol{r}_n^m\}$, uniformly spaced within the medium but distinct from the positions of scatterers, and $\mathcal{G}_0^{(M)}(\{\boldsymbol{r}_n^m\};\{\boldsymbol{r}_i\};\omega)$ the $M\times N$ matrix of propagators linking the measurement points to the scatterers, one finds

$$\varrho_{med}(\omega)\approx\varrho_0(\omega)V_{med}+\frac{2\omega^3V_{med}}{M\pi c^4}\mathrm{Im}\left[\alpha(\omega)\mathrm{Tr}_{3M}\left[\mathcal{G}_0^{(M)}(\{\boldsymbol{r}_n^m\};\{\boldsymbol{r}_i\};\omega)\cdot\mathcal{W}(\{\boldsymbol{r}_{ij}\};\omega)\cdot{}^t\mathcal{G}_0^{(M)}(\{\boldsymbol{r}_n^m\};\{\boldsymbol{r}_j\};\omega)\right]\right], \tag{S82}$$

where the trace is now computed over all $3M$ diagonal elements of the matrix product. In practice, we compute the relative corrections to the density of states of vacuum, $\delta\varrho(\boldsymbol{r},\omega)=(\varrho(\boldsymbol{r},\omega)-\varrho_0(\omega))/\varrho_0(\omega)$ and $\delta\varrho_{med}(\omega)=(\varrho_{med}(\omega)-\varrho_0(\omega)V_{med})/(\varrho_0(\omega)V_{med})$, which are numbers in $[-1;\infty[$, the sign of which indicate depletion or enrichment in number of states. Note that it is common [36] to define the generalized Purcell factor $F(\omega,\boldsymbol{r})$ such that $\delta\varrho(\boldsymbol{r},\omega)=F(\omega,\boldsymbol{r})-1$.

B. Specific geometries

The previous subsection introduced every quantity in a way that did not specify the geometry of the problem, encoded by propagators, explicitly. We here remind the expressions of every quantity of interest in the 4 cases considered in the paper: $2d$ vector, $2d$ scalar, $3d$ vector, and $3d$ scalar waves, all in free space.

1. *Rayleigh scatterers for vector waves in 3d space*

The most usual context for light propagation is that of free $3d$ space with finite scatterers. In this case, the Green's function associated to free propagation can be written as [34, 36, 37]

$$\overline{\overline{G}}_0(\boldsymbol{r},\boldsymbol{r}';\omega)=PV\left(\frac{e^{ik_0R}}{4\pi R}\left[\overline{\overline{I}}-\hat{\boldsymbol{R}}\otimes\hat{\boldsymbol{R}}-\left(\frac{1}{ik_0R}+\frac{1}{k_0^2R^2}\right)\left(\overline{\overline{I}}-3\hat{\boldsymbol{R}}\otimes\hat{\boldsymbol{R}}\right)\right]\right)-\frac{\delta(\boldsymbol{R})}{3k_0^2}\overline{\overline{I}}, \tag{S83}$$

where PV indicates a Cauchy principal value, $\boldsymbol{R}\equiv\boldsymbol{r}-\boldsymbol{r}'=R\hat{\boldsymbol{R}}$, $k_0=\omega/c$, $\overline{\overline{I}}$ is the identity tensor, and $\otimes$ is the outer product. Note that the Green's function should be understood as a distribution, and consists of a regular part that diverges as $R\to0$ together with a singular part at $\boldsymbol{R}=\boldsymbol{0}$.

From this expression, one may write the expression of the self-interaction for small spherical scatterers. The relevant integral to compute, following Eq. 65, is

$$\overline{\overline{S}}_{3d}(\omega)=\int_{\mathcal{B}(\boldsymbol{0},a)}d^3\boldsymbol{r}'\,\overline{\overline{G}}_0(\boldsymbol{0},\boldsymbol{r}';\omega), \tag{S84}$$

where the integral runs over the volume of the scatterer, the ball $\mathcal{B}(\boldsymbol{0},a)$ centered at $\boldsymbol{0}$ and with radius a. This integral can be rewritten in spherical coordinates as

$$\overline{\overline{S}}_{3d}(\omega)=\int_0^a dr'\int_{-\pi}^{\pi}d\varphi\int_0^{\pi}d\theta\,r'^2\sin\theta\overline{\overline{G}}_0(\boldsymbol{0},\boldsymbol{r}';\omega). \tag{S85}$$

To compute this integral, it is useful to notice that

$$\int_{-\pi}^{\pi}d\varphi\int_0^{\pi}d\theta\,\sin\theta\hat{\boldsymbol{R}}\otimes\hat{\boldsymbol{R}}=\frac{4\pi}{3}\overline{\overline{I}}=\frac{1}{3}\int_{-\pi}^{\pi}d\varphi\int_0^{\pi}d\theta\,\sin\theta\overline{\overline{I}}, \tag{S86}$$

so that substituting Eq. 83 into Eq. 85 yields

$$\overline{\overline{S}}_{3d}(\omega)=-\frac{1}{3k_0^2}\overline{\overline{I}}+\frac{2}{3}\overline{\overline{I}}\int_0^a dr'\,r'e^{ik_0r'}, \tag{S87}$$

$$=-\frac{1}{3k_0^2}\overline{\overline{I}}+\frac{2}{3}\overline{\overline{I}}\left(\frac{e^{ik_0a}}{k_0^2}(1-ik_0a)-\frac{1}{k_0^2}\right) \tag{S88}$$

$$=\frac{1}{k_0^2}\left(\frac{2}{3}e^{ik_0a}(1-ik_0a)-1\right)\overline{\overline{I}} \tag{S89}$$

In this result, the first term is kept separate as it comes from the singular part of the Green's function. Interestingly, this full form is not trivially consistent with energy conservation in the CDM. Indeed, to ensure energy conservation, the renormalization of polarizability by the self-interaction must ensure that

$$\sigma_e = \sigma_a + \sigma_s \tag{S90}$$

where $\sigma_{e,a,s}$ are respectively the extinction, absorption, and scattering cross-sections which, if a scatterer is illuminated by a plane-wave with intensity I_0, yield the extinguished, absorbed, and scattered powers via $P_{e,a,s} = \sigma_{e,a,s} I_0$. One may show that, in $3d$ space and in the (Rayleigh) limit $a \to 0$ [36]

$$\sigma_e = k_0 \mathrm{Im}\left[\alpha_d(\omega)\right], \tag{S91}$$

$$\sigma_s = \frac{k_0^4}{6\pi} \left|\alpha_d(\omega)\right|^2. \tag{S92}$$

For a non-absorbing scatterer, $\alpha_0 \in \mathbb{R}$, Eq. 71 can be rewritten in a way that makes the real and imaginary parts more apparent, and introducing the notation $\overline{\overline{S}}_{3d} = S_{3d}\overline{\overline{I}}$,

$$\alpha_d = \frac{\alpha_0(\omega)}{\left|1 - k_0^2 \alpha_0(\omega) S_{3d}/V\right|^2} \left(1 - k_0^2 \alpha_0(\omega) S_{3d}^\dagger / V\right). \tag{S93}$$

As a result, the extinction cross-section reads

$$\sigma_e = \frac{k_0^3 \alpha_0^2(\omega)}{\left|1 - k_0^2 \alpha_0(\omega) S_{3d}/V\right|^2} \mathrm{Im}\left[S_{3d}\right]/V. \tag{S94}$$

On the other hand, the scattering cross-section reads

$$\sigma_s = \frac{k_0^4}{6\pi} \frac{\alpha_0^2(\omega)}{\left|1 - k_0^2 \alpha_0(\omega) S_{3d}/V\right|^2}. \tag{S95}$$

These two values are equal if:

$$\mathrm{Im}\left[S_{3d}\right] = \frac{k_0 V}{6\pi}. \tag{S96}$$

To meet this condition, one can consider an approximate form [36], which is obtained by Taylor-expanding the regular part of the integral to leading order in $k_0 a$, so that

$$\overline{\overline{S}}_{3d}(\omega) = \left(-\frac{1}{3k_0^2} + \frac{a^2}{3} + \frac{2}{9} i k_0 a^3\right) \overline{\overline{I}} + \mathcal{O}(k_0^2 a^4). \tag{S97}$$

For a single scatterer with radius a and volume $V = 4\pi a^3/3$, this last approximate equation leads to a well-known result,

$$\alpha_d \approx \frac{\alpha_r(\omega)}{1 - \frac{i k_0^3}{6\pi} \alpha_r(\omega)} \tag{S98}$$

where the second term in the denominator is often called the *radiative correction* to the polarizability, as it ensures conservation of the energy of the optical field, and we defined a rescaled polarizability,

$$\alpha_r(\omega) \equiv 3V \frac{\delta\varepsilon(\omega)}{3 + \delta\varepsilon(\omega)(1 - k_0^2 a^2)}. \tag{S99}$$

Note that this last expression is also often used in its so-called quasistatic limit,

$$\alpha_r(\omega) \underset{k_0 a \to 0}{\to} 3V \frac{\varepsilon - 1}{\varepsilon + 2}, \tag{S100}$$

which is known as the Clausius-Mossotti, or Lorentz-Lorenz, equation. Note that, assuming non-absorbing scatterers with a constant dielectric contrast, the real part of the denominator of Eq. 98 diverges at a resonant frequency,

$$\omega_r^2 = \frac{c^2}{a^2} \frac{3 + \delta\varepsilon_s}{\delta\varepsilon_s}. \tag{S101}$$

Finally, let us compute the LDOS of vacuum for $3d$ vector waves. By definition,

$$\varrho_0(\omega) = \frac{2\omega}{\pi c^2}\mathrm{Im}\left[\mathrm{Tr}_3\overline{\overline{G}}_0(\boldsymbol{r},\boldsymbol{r};\omega)\right]. \tag{S102}$$

To compute it, it is useful to first write the trace of the Green's function for any pair of points. Making use of $\mathrm{Tr}_3\hat{\boldsymbol{R}}\otimes\hat{\boldsymbol{R}} = 1$, one gets

$$\mathrm{Tr}_3\overline{\overline{G}}_0(\boldsymbol{r},\boldsymbol{r}';\omega) = PV\left[\frac{e^{ik_0R}}{2\pi R}\right] - \frac{\delta(\boldsymbol{R})}{k_0^2}, \tag{S103}$$

so that

$$\mathrm{Im}\left[\mathrm{Tr}_3\overline{\overline{G}}_0(\boldsymbol{r},\boldsymbol{r}';\omega)\right] = \frac{\sin(k_0R)}{2\pi R} \underset{R\to 0}{\to} \frac{k_0}{2\pi}, \tag{S104}$$

and

$$\varrho_0(\omega) = \frac{\omega^2}{\pi^2c^3}. \tag{S105}$$

A consequence of this result for small scatterers in free $3d$ space is that the LDOS, Eq. 80, of the system can be written with the LDOS of vacuum explicitly factored out:

$$\delta\varrho(\boldsymbol{r},\omega) \equiv \frac{\varrho(\boldsymbol{r},\omega)}{\varrho_0(\omega)} - 1 = 2\pi k_0\mathrm{Im}\left[\alpha(\omega)\mathrm{Tr}_3\left[\mathcal{G}_0^{(1)}(\boldsymbol{r};\{\boldsymbol{r}_i\};\omega)\cdot\mathcal{W}(\{\boldsymbol{r}_{ij}\};\omega)\cdot{}^t\mathcal{G}_0^{(1)}(\boldsymbol{r};\{\boldsymbol{r}_j\};\omega)\right]\right]. \tag{S106}$$

2. 3d scalar waves

In acoustics, but also in simplified optics models, it is common to consider scalar waves in $3d$, *i.e.* a scalar field E that verifies

$$\nabla^2E(\boldsymbol{r};\omega) - \frac{\omega^2}{c^2}\varepsilon(\boldsymbol{r};\omega)E(\boldsymbol{r};\omega) = i\mu_0\omega j_{ext}(\boldsymbol{r};\omega). \tag{S107}$$

This is in spirit equivalent to a linearly polarized field that is unable to couple to other polarizations, like the TM component in the context of $2d$-like propagation, or the remaining component of $1d$-like propagation. Defining $\boldsymbol{R} = \boldsymbol{r} - \boldsymbol{r}'$, one may associate a free-space Green's (scalar) function G_0 to this equation that reads [36]

$$G_0(\boldsymbol{r},\boldsymbol{r}';\omega) = \frac{e^{ik_0R}}{4\pi R}. \tag{S108}$$

From this expression, we compute the other quantities derived in the previous subsection. First, the self-interaction integral for a small spherical scatterer with radius a is defined by

$$S_{3d}^{scalar}(\omega) \equiv \int_{\mathcal{B}(\mathbf{0},a}} d^3\boldsymbol{r}'G_0(\mathbf{0},\boldsymbol{r}';\omega). \tag{S109}$$

Rewriting the integral in spherical coordinates, it may be rewritten as

$$S_{3d}^{scalar}(\omega) = \int_0^a d\rho\,\rho e^{ik_0\rho} \tag{S110}$$

and finally

$$S_{3d}^{scalar}(\omega) = \frac{1}{k_0^2}\left(e^{ik_0a}(1-ik_0a) - 1\right). \tag{S111}$$

The first few terms of the Taylor expansion of this self-interaction read

$$S_{3d}^{scalar}(\omega) = \frac{a^2}{2} + i\frac{k_0a^3}{3} + \mathcal{O}(k_0^2a^3), \tag{S112}$$

so that the dressed polarizability of a single scatterer can be written as

$$\alpha_d = \frac{\alpha_0(\omega)}{1 - k_0^2 \alpha_0(\omega) S_{3d}^{scalar}/V} \tag{S113}$$

which, after injecting the Taylor expansion and some simple algebra, yields

$$\alpha_d \approx \frac{\alpha_r(\omega)}{1 - i\frac{k_0^3}{4\pi}\alpha_r(\omega)} \tag{S114}$$

with

$$\alpha_r(\omega) \equiv \frac{\alpha_0}{1 - \frac{3k_0^2\alpha_0}{8\pi a}}. \tag{S115}$$

Rewriting the bare polarizability as a function of volume and dielectric contrast, the expression becomes

$$\alpha_r(\omega) = V\frac{\delta\varepsilon}{1 - \frac{k_0^2 a^2 \delta\varepsilon}{2}} \underset{k_0\to 0}{\to} \alpha_0. \tag{S116}$$

This is a well-known result [36]: in particular, away from $k_0 = 0$ this expression contains radiative corrections that generate a resonance at

$$k_r a = \sqrt{\frac{8\pi a^3}{3\mathrm{Re}[\alpha_0]}} = \sqrt{\frac{2}{\mathrm{Re}[\delta\varepsilon]}}. \tag{S117}$$

Note that for scalar waves the scattering cross-section in the limit $a \to 0$ is defined via

$$\sigma_s = \frac{k_0^4}{4\pi}\left|\alpha_d(\omega)\right|^2, \tag{S118}$$

so that the optical theorem being valid requires

$$\mathrm{Im}[S] = \frac{k_0}{4\pi}V = \frac{k_0 a^3}{3}. \tag{S119}$$

Finally, the density of state of vacuum in this problem is defined as

$$\rho_0^{3d,scalar}(\omega) \equiv \frac{2\omega}{\pi c^2}\mathrm{Im}\left[G_0(\boldsymbol{r},\boldsymbol{r};\omega)\right]. \tag{S120}$$

Here, the imaginary part of the propagator simply reads

$$\mathrm{Im}\left[G_0(\boldsymbol{r},\boldsymbol{r}';\omega)\right] = \frac{k_0}{4\pi}\mathrm{sinc}(k_0 R) \underset{R\to 0}{\to} \frac{k_0}{4\pi} \tag{S121}$$

so that

$$\rho_0^{3d,scalar}(\omega) = \frac{\omega^2}{2\pi^2 c^3}. \tag{S122}$$

Note that this is half of the vector wave value, Eq. 105. As a result,

$$\delta\varrho(\boldsymbol{r},\omega) \equiv \frac{\varrho(\boldsymbol{r},\omega)}{\varrho_0(\omega)} - 1 = 4\pi k_0 \mathrm{Im}\left[\alpha(\omega)\left[\mathcal{G}_0^{(1)}(\boldsymbol{r};\{\boldsymbol{r}_i\};\omega)\cdot\mathcal{W}(\{\boldsymbol{r}_{ij}\};\omega)\cdot{}^t\mathcal{G}_0^{(1)}(\boldsymbol{r};\{\boldsymbol{r}_j\};\omega)\right]\right]. \tag{S123}$$

3. Infinite, parallel straight rods with small cross-sections

The other case we consider at length is that of a system of scatterers that are well approximated by infinite right cylinders, all parallel to the z axis, with small circular cross-sections. Such a system is invariant in the z direction, so that it is natural to rewrite the Green's function in cylindrical coordinates, $(\boldsymbol{\rho}, z)$ where (for clarity), we now call $\boldsymbol{\rho}$

the polar position in the xy plane. Due to invariance in the z direction, the source imposes the z dependence of the field. Suppose the dependence of the source current is simply plane in the z direction,

$$\boldsymbol{j}_{ext}(\boldsymbol{r}) = \boldsymbol{j}_{ext}(\boldsymbol{\rho})e^{ik_{z,inc}z}. \tag{S124}$$

One may then define the $2d$ Green's function between any two polar coordinates in the xy plane as the integral over z of the full Green's function applied to the z-dependent part of the current:

$$\overline{\overline{G}}_0(\boldsymbol{\rho},\boldsymbol{\rho}';\omega) = \int_{-\infty}^{\infty} dz' \overline{\overline{G}}_0(\boldsymbol{r},\boldsymbol{r}';\omega)e^{ik_{z,inc}z'}. \tag{S125}$$

Using the expression in Eq. 83 of the $3d$ Green's function of free space, rewritten in a convenient way as

$$\overline{\overline{G}}_0(\boldsymbol{r},\boldsymbol{r}';\omega) = \left[\overline{\overline{I}} + \frac{1}{k_0^2}\boldsymbol{\nabla}\otimes\boldsymbol{\nabla}\right]\frac{e^{ik_0R}}{4\pi R}, \tag{S126}$$

as well as the integral definition of the zeroth order Hankel's functions of the first kind $H_0^{(1)}$, here through the expression

$$\int_{-\infty}^{\infty} dz' \frac{e^{ik_0\sqrt{|\boldsymbol{\rho}-\boldsymbol{\rho}'|^2+(z-z')^2}}}{\sqrt{|\boldsymbol{\rho}-\boldsymbol{\rho}'|^2+(z-z')^2}}e^{ik_{z,inc}z'} = i\pi H_0^{(1)}(k_\rho|\boldsymbol{\rho}-\boldsymbol{\rho}'|)e^{ik_{z,inc}z}, \tag{S127}$$

where $k_\rho^2 = k_0^2 - k_{z,inc}^2$, and noticing that the nablas here reduce to $\nabla = (\partial_x, \partial_y, ik_{z,inc})$ one finds

$$\overline{\overline{G}}_0(\boldsymbol{\rho},\boldsymbol{\rho}';\omega) = \begin{pmatrix} 1+\frac{\partial_x^2}{k_0^2} & \frac{\partial_x\partial_y}{k_0^2} & \frac{ik_{z,inc}\partial_x}{k_0^2} \\ \frac{\partial_x\partial_y}{k_0^2} & 1+\frac{\partial_y^2}{k_0^2} & \frac{ik_{z,inc}\partial_y}{k_0^2} \\ \frac{ik_{z,inc}\partial_x}{k_0^2} & \frac{ik_{z,inc}\partial_y}{k_0^2} & \frac{k_\rho^2}{k_0^2} \end{pmatrix} \frac{i}{4}H_0^{(1)}(k_\rho|\boldsymbol{\rho}-\boldsymbol{\rho}'|)e^{ik_{z,inc}z}. \tag{S128}$$

In particular, if the source is assumed to be invariant along z as well, or at least such that $k_{z,inc} \to 0$, this matrix reduces to a block-diagonal one

$$\overline{\overline{G}}_0(\boldsymbol{\rho},\boldsymbol{\rho}') = \begin{pmatrix} \overline{\overline{G}}_0^{TE}(\boldsymbol{\rho},\boldsymbol{\rho}') & \begin{matrix}0\\0\end{matrix} \\ \begin{matrix}0 & 0\end{matrix} & G_0^{TM}(\boldsymbol{\rho},\boldsymbol{\rho}') \end{pmatrix}, \tag{S129}$$

where we introduced the so-called Transverse Electric (TE) and Transverse Magnetic (TM) propagators. In practice, the fact that the matrix is block-diagonal means that the z and (x,y) components of a field, also called TM and TE polarizations, here propagate independently. Using this expression and the relation between the first two Hankel functions,

$$\frac{d}{dx}H_0^{(1)}(x) = -H_1^{(1)}(x), \tag{S130}$$

and now calling $\boldsymbol{R} = \boldsymbol{\rho} - \boldsymbol{\rho}'$ one may write the explicit expressions of both propagators as

$$\overline{\overline{G}}_0^{TE}(\boldsymbol{\rho},\boldsymbol{\rho}';\omega) = \frac{i}{4}\left(\overline{\overline{I}} - \hat{\boldsymbol{R}}\otimes\hat{\boldsymbol{R}}\right)H_0^{(1)}(k_0R) - \frac{i}{4}PV\left[\left(\overline{\overline{I}} - 2\hat{\boldsymbol{R}}\otimes\hat{\boldsymbol{R}}\right)\frac{H_1^{(1)}(k_0R)}{k_0R}\right] - \frac{\delta(\boldsymbol{R})}{2k_0^2}\overline{\overline{I}}, \tag{S131}$$

$$G_0^{TM}(\boldsymbol{\rho},\boldsymbol{\rho}';\omega) = \frac{i}{4}H_0^{(1)}(k_0R). \tag{S132}$$

As a result of the propagator breaking down into two independent parts, all scattering properties can also be decomposed into two independent polarization components.

With this definition for the components of the Green's function, the whole $3d$ calculation can be adapted and the system of equations between scatterers written purely in-plane,

$$\boldsymbol{E}(\boldsymbol{\rho}_j;\omega) \approx \boldsymbol{E}_{inc}(\boldsymbol{\rho}_j;\omega) + \frac{\omega^2}{c^2}\sum_{j\neq i}^{N}\Sigma_i\delta\varepsilon_i(\omega)\overline{\overline{G}}_0(\boldsymbol{\rho}_j,\boldsymbol{\rho}_i;\omega)\boldsymbol{E}(\boldsymbol{\rho}_i;\omega) + \frac{\omega^2}{c^2}\delta\varepsilon_j(\omega)\left[\int_{\Sigma_j} d^2\boldsymbol{\rho}'\,\overline{\overline{G}}_0(\boldsymbol{\rho}_j,\boldsymbol{\rho}';\omega)\right]\boldsymbol{E}(\boldsymbol{\rho}_j;\omega), \tag{S133}$$

where Σ_i is the cross-section area of cylinder i, leading to the $2d$ definition of the bare polarizability $\alpha_i(\omega) \equiv \Sigma_i \delta\epsilon_i(\omega)$.

We first establish the value of the self-interaction integral for both TE and TM polarizations. In the TM case,

$$S_{2d}^{TM}(\omega) = \int_{\mathcal{D}(\mathbf{0},a)} d^2\boldsymbol{r}'\, G_0^{TM}(\mathbf{0},\boldsymbol{r}';\omega), \tag{S134}$$

where $\mathcal{D}(\mathbf{0},a)$ is the disk centered at $\mathbf{0}$ with radius a. This integral is best rewritten in polar coordinates,

$$S_{2d}^{TM}(\omega) = \frac{i}{4}\int_0^a d\rho \int_{-\pi}^{\pi} d\theta\, \rho H_0^{(1)}(k_0\rho), \tag{S135}$$

which yields

$$S_{2d}^{TM}(\omega) = i\frac{\pi a^2}{2}\frac{H_1^{(1)}(k_0 a)}{k_0 a} - \frac{1}{k_0^2}. \tag{S136}$$

Again, this expression can be approximated by its leading order terms in its Taylor expansion [51],

$$S_{2d}^{TM}(\omega) = -\frac{a^2}{4}\left(2\gamma - 1 - i\pi + 2\log\frac{k_0 a}{2}\right) + \mathcal{O}(k_0^2 a^2), \tag{S137}$$

where $\gamma = 0.577216\ldots$ is Euler's gamma constant. Like in $3d$, one may define a dressed TM polarizability,

$$\alpha_d^{TM} = \frac{\alpha_0(\omega)}{1 - k_0^2\alpha_0(\omega)S_{2d}^{TM}/\Sigma}, \tag{S138}$$

with $\Sigma = \pi a^2$ the cross section area of the scatterers. Using the Taylor-expanded version of S_{2d}, one can find the analog of Eq. 98,

$$\alpha_d^{TM} \approx \frac{\alpha_r^{TM}(\omega)}{1 - \frac{ik_0^2}{4}\alpha_r^{TM}(\omega)}, \tag{S139}$$

with

$$\alpha_r^{TM}(\omega) = \frac{\alpha_0}{1 + \frac{\alpha_0 k_0^2}{4\pi}\left(2\gamma - 1 + 2\log\frac{k_0 a}{2}\right)} \underset{k_0\to 0}{\to} \alpha_0. \tag{S140}$$

As for the TE polarization, the self-interaction integral reads

$$\overline{\overline{S}}_{2d}^{TE}(\omega) = \int_{\mathcal{D}(\mathbf{0},a)} d^2\boldsymbol{r}'\, \overline{\overline{G}}_0^{TE}(\mathbf{0},\boldsymbol{r}';\omega). \tag{S141}$$

It is useful to notice that

$$\int_{-\pi}^{\pi} d\theta\, \hat{\boldsymbol{R}}\otimes\hat{\boldsymbol{R}} = \pi\overline{\overline{I}} = \frac{1}{2}\int_{-\pi}^{\pi} d\theta\, \overline{\overline{I}}, \tag{S142}$$

so that

$$\overline{\overline{S}}_{2d}^{TE}(\omega) = \frac{i\pi}{4}\int_0^a d\rho\, \rho H_0^{(1)}(k_0\rho)\overline{\overline{I}} - \frac{1}{2k_0^2}\overline{\overline{I}}, \tag{S143}$$

$$= \left(i\frac{\pi a^2}{4}\frac{H_1^{(1)}(k_0 a)}{k_0 a} - \frac{1}{k_0^2}\right)\overline{\overline{I}}. \tag{S144}$$

Rewriting the last expression as $\overline{\overline{S}}_{2d}^{TE}(\omega) = S_{2d}^{TE}(\omega)\overline{\overline{I}}$, and noticing that the Taylor expansion of the scalar prefactor reads

$$S_{2d}^{TE}(\omega) = -\frac{1}{2k_0^2} - \frac{a^2}{8}\left(2\gamma - 1 - i\pi + 2\log\frac{k_0 a}{2}\right) + \mathcal{O}(k_0^2 a^2). \tag{S145}$$

Once again, we can write the dressed polarizability of a single scatterer as

$$\alpha_d^{TE} = \frac{\alpha_0(\omega)}{1 - k_0^2\alpha_0(\omega)S_{2d}^{TE}/\Sigma}, \tag{S146}$$

which, to leading order, yields

$$\alpha_d^{TE} \approx \frac{\alpha_r^{TE}(\omega)}{1 - \frac{ik_0^2}{8}\alpha_r^{TE}(\omega)}, \tag{S147}$$

where

$$\alpha_r^{TE}(\omega) = \frac{\alpha_0}{1 + \frac{\alpha_0}{2\Sigma} + \frac{\alpha_0 k_0^2}{8\pi}\left(2\gamma - 1 + 2\log\frac{k_0 a}{2}\right)} \underset{k_0\to 0}{\to} 2\Sigma\frac{\delta\varepsilon}{2+\delta\varepsilon} = 2\Sigma\frac{\varepsilon-1}{\varepsilon+1}. \tag{S148}$$

The latter quasi-static limit is a known variation of the Clausius-Mossotti relation for $2d$ vector waves [35, 51].

Note that the expression of α_d as a function of S is different for $2d$ waves. Since the extinction cross-section σ_e is always defined as $\sigma_e = k_0\mathrm{Im}\left[\alpha_d\right]$, this implies that the scattering cross-section has a dimensionality-dependent definition (a conclusion that may also be reached by dimensional analysis). In $2d$, the definition in the limit $a \to 0$ becomes [42, 45]

$$\sigma_s^{TM} = \frac{k_0^3}{4}\left|\alpha_d^{TM}\right|^2, \tag{S149}$$

$$\sigma_s^{TE} = \frac{k_0^3}{8}\left|\alpha_d^{TE}\right|^2. \tag{S150}$$

This implies that the optical theorem being valid requires

$$Im[S^{TM}] = \frac{\Sigma}{4} = \frac{\pi a^2}{4}, \tag{S151}$$

$$Im[S^{TE}] = \frac{\Sigma}{8} = \frac{\pi a^2}{8}. \tag{S152}$$

Finally, let us compute the LDOS of vacuum for TE and TM waves, starting with the latter,

$$\varrho_0^{TM}(\omega) = \frac{2\omega}{\pi c^2}\mathrm{Im}\left[G_0^{TM}(\boldsymbol{\rho},\boldsymbol{\rho};\omega)\right]. \tag{S153}$$

Using the expression of the Green's function, this equation becomes

$$\varrho_0^{TM}(\omega) = \frac{\omega}{2\pi c^2}\lim_{\rho\to 0^+}\mathrm{Re}\left[H_0^{(1)}(k_0\rho)\right]. \tag{S154}$$

To find an explicit expression, it is useful to write the Taylor expansion

$$H_0^{(1)}(x) = 1 + \frac{i}{\pi}\left(2\gamma - 2\log\frac{x}{2}\right) + \mathcal{O}(x^2), \tag{S155}$$

leading to

$$\varrho_0^{TM}(\omega) = \frac{\omega}{2\pi c^2}. \tag{S156}$$

As a result, the TM LDOS, analogous to Eq. 80, reads

$$\varrho(\boldsymbol{\rho},\omega)^{TM} = \varrho_0(\omega)^{TM} + \frac{2\omega^3}{\pi c^4}\mathrm{Im}\left[\alpha(\omega)\left[\mathcal{G}_0^{(1),TM}(\boldsymbol{\rho};\{\boldsymbol{\rho}_i\};\omega)\cdot\mathcal{W}^{TM}(\{\boldsymbol{\rho}_{ij}\};\omega)\cdot{}^t\mathcal{G}_0^{(1),TM}(\boldsymbol{\rho};\{\boldsymbol{\rho}_j\};\omega)\right]\right], \tag{S157}$$

where every matrix with exponent TM is similar to that of the $3dcase$ but with the 3×3 Green's tensor elements replaced by scalar TM Green's functions, can be written with the vacuum contribution factored out

$$\delta\varrho^{TM}(\boldsymbol{\rho},\omega) \equiv \frac{\varrho^{TM}(\boldsymbol{\rho},\omega)}{\varrho_0^{TM}(\omega)} - 1 = 4k_0^2\mathrm{Im}\left[\alpha(\omega)\left[\mathcal{G}_0^{(1),TM}(\boldsymbol{\rho};\{\boldsymbol{\rho}_i\};\omega)\cdot\mathcal{W}^{TM}(\{\boldsymbol{\rho}_{ij}\};\omega)\cdot{}^t\mathcal{G}_0^{(1),TM}(\boldsymbol{\rho};\{\boldsymbol{\rho}_j\};\omega)\right]\right]. \tag{S158}$$

Likewise, the vacuum LDOS for the TE mode reads

$$\varrho_0^{TE}(\omega) = \frac{2\omega}{\pi c^2}\mathrm{Im}\left[\mathrm{Tr}_2\overline{\overline{G}}_0^{TE}(\boldsymbol{\rho},\boldsymbol{\rho};\omega)\right]. \tag{S159}$$

To compute it, it is useful to first write the trace of the Green's function for any pair of points. Making use of $\mathrm{Tr}_2\hat{\boldsymbol{R}}\otimes\hat{\boldsymbol{R}} = 1$, one gets

$$\mathrm{Tr}_2\overline{\overline{G}}_0^{TE}(\boldsymbol{\rho},\boldsymbol{\rho}';\omega) = \frac{i}{4}PV\left[H_0^{(1)}(k_0R)\right] - \frac{\delta(\boldsymbol{R})}{k_0^2}, \tag{S160}$$

so that

$$\mathrm{Im}\left[\mathrm{Tr}_2\overline{\overline{G}}_0^{TE}(\boldsymbol{\rho},\boldsymbol{\rho}';\omega)\right] = \frac{1}{4}\mathrm{Re}\left[H_0^{(1)}(k_0R)\right] \underset{R\to 0}{\to} \frac{1}{4}, \tag{S161}$$

and

$$\varrho_0^{TE}(\omega) = \frac{\omega}{2\pi c^2}. \tag{S162}$$

Consequently, using the definition

$$\varrho^{TE}(\boldsymbol{r},\omega) = \varrho_0^{TE}(\omega) + \frac{2\omega^3}{\pi c^4}\mathrm{Im}\left[\alpha(\omega)\mathrm{Tr}_2\left[\mathcal{G}_0^{(1),TE}(\boldsymbol{\rho};\{\boldsymbol{\rho}_i\};\omega)\cdot\mathcal{W}^{TE}(\{\boldsymbol{\rho}_{ij}\};\omega)\cdot{}^t\mathcal{G}_0^{(1),TE}(\boldsymbol{\rho};\{\boldsymbol{\rho}_j\};\omega)\right]\right], \tag{S163}$$

one may write

$$\delta\varrho^{TE}(\boldsymbol{\rho},\omega) \equiv \frac{\varrho^{TE}(\boldsymbol{\rho},\omega)}{\varrho_0^{TE}(\omega)} - 1 = 4k_0^2\mathrm{Im}\left[\alpha(\omega)\mathrm{Tr}_2\left[\mathcal{G}_0^{(1),TE}(\boldsymbol{\rho};\{\boldsymbol{\rho}_i\};\omega)\cdot\mathcal{W}^{TE}(\{\boldsymbol{\rho}_{ij}\};\omega)\cdot{}^t\mathcal{G}_0^{(1),TE}(\boldsymbol{\rho};\{\boldsymbol{\rho}_j\};\omega)\right]\right]. \tag{S164}$$

Instead of the LDOS of vacuum, one may instead use the LDOS of an infinite medium with dielectric constant ε_m as a normalization, which would read, for both TE and TM,

$$\varrho_0(\omega;\varepsilon_m) = \frac{\omega\varepsilon_m}{2\pi c^2}. \tag{S165}$$

Note that one may write the full LDOS in this geometry using the same definition as in $3d$, which, due to the linearity of the trace, leads to

$$\varrho^{2d}(\boldsymbol{r},\omega) = \varrho^{TM}(\boldsymbol{r},\omega) + \varrho^{TE}(\boldsymbol{r},\omega). \tag{S166}$$

Combining previous expressions, the final result for the relative change of this object compared to vacuum reads

$$\delta\varrho^{2d}(\boldsymbol{\rho},\omega) \equiv \frac{\varrho^{2d}(\boldsymbol{\rho},\omega)}{\varrho_0^{2d}(\omega)} - 1 = 4k_0^2\mathrm{Im}\left[\alpha(\omega)\mathrm{Tr}_3\left[\mathcal{G}_0^{(1),2d}(\boldsymbol{\rho};\{\boldsymbol{\rho}_i\};\omega)\cdot\mathcal{W}^{2d}(\{\boldsymbol{\rho}_{ij}\};\omega)\cdot{}^t\mathcal{G}_0^{(1),2d}(\boldsymbol{\rho};\{\boldsymbol{\rho}_j\};\omega)\right]\right], \tag{S167}$$

where this time matrices with exponent $2d$ refer to matrices of 3×3 block-diagonal tensors containing TE and TM modes.

C. Validation with Finite-Difference methods

In this section, we briefly show that the results we obtain by CDM are consistent with commonly used DOS measurements using finite-difference methods in the frequency domain (FDFD) [52]. In short, the method consists in discretizing a configuration into pixels (or voxels in $3d$) of material, each with a homogeneous dielectric constant, then in solving for eigenvalues of the discretized Maxwell equations in Fourier space. This method relies on a periodicization of real space, so that it is particularly well suited to study crystalline systems. It however scales very badly with the number of pixels needed to describe the system. As a result, its use is limited to rather small systems of scatterers, and it is not clear how periodicized results relate to the properties of finite-size materials with real boundaries. This is precisely why, like a large number of past works on optics in disordered materials [36], we decided to use a coupled dipoles approach.

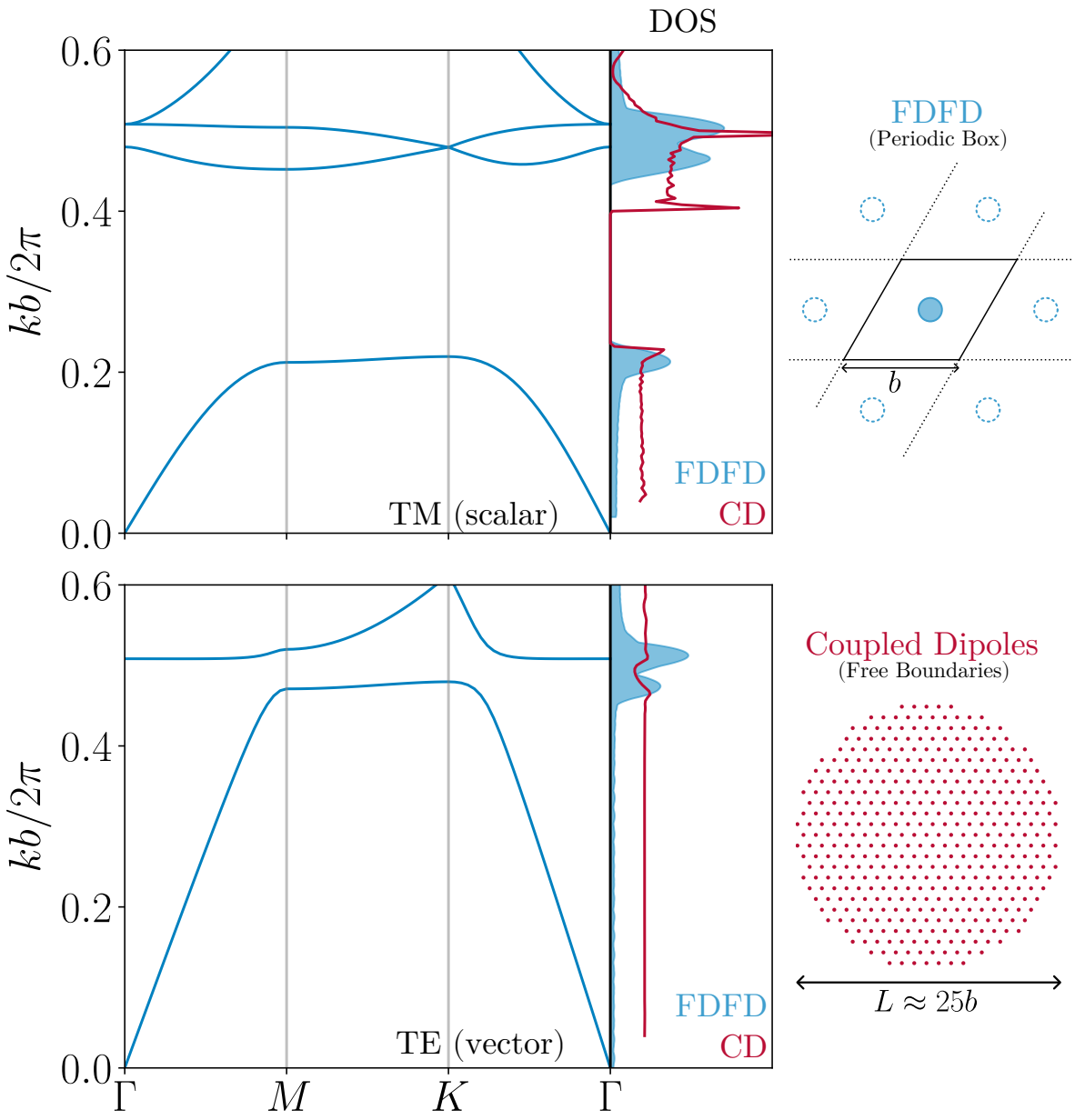


FIG. S21. **FDFD comparison.** FDFD calculation of the low-lying band structure of a triangular lattice for the TM (top) and TE (bottom) polarizations. The band structure is shown (left), and used to compute a DOS (middle, shaded blue curves), which is compared to our coupled dipoles (CD) DOS estimates (red lines). In the right-most column, we remind the geometries considered in both approaches.

Since FDFD measurements are still common in the field of disordered materials, see *e.g.* Refs. 2 and 53, we however give a minimal proof that both approaches give compatible results in a simple example in which FDFD is tractable. We consider a single dielectric rod with $n = 6$ with radius a, within a rhombic unit cell such that periodicity produces an infinite triangular lattice with lattice spacing b, and with a filling fraction $\phi = 5\%$. The system is discretized onto a grid of 256^2 pixels. We then perform an FDFD analysis using the standard MPB package [52], and compare the output with a coupled dipoles approach for a disk-shaped chunk of a triangular lattice with a diameter $L \approx 25b$. The results are reported in Fig. S21, for both TM and TE polarizations. We show band structures in the usual angle-modulus representation. We extract a DOS from these bands in a standard way, by broadening bands by some smooth finite-width kernel (here a quadratic polynomial kernel with finite support, or "Epanechnikov"). As expected,

a gap develops in the region $kb/2\pi \lesssim 1$, and it is much wider in TM than TE. We show that our coupled dipoles calculations reproduce similar features. Note that this is a result, more than a validity check: FDFD approaches essentially consider the infinite perfect lattice for crystals (or introduce costly Perfectly Matched Layers that also stray from experimental conditions [54]), while coupled dipoles consider a finite chunk with an actual boundary in free boundary conditions. As such, one may expect coupled dipoles to follow more closely experimental conditions.

[1] A. Shih, M. Casiulis, and S. Martiniani, Fast Generation of Spectrally-Shaped Disorder, Physical Review E **110**, 034122 (2024).

[2] L. S. Froufe-Pérez, M. Engel, J. J. Sáenz, and F. Scheffold, Band gap formation and Anderson localization in disordered photonic materials with structural correlations, Proceedings of the National Academy of Sciences of the United States of America **114**, 9570 (2017).

[3] R. Monsarrat, R. Pierrat, A. Tourin, and A. Goetschy, Pseudogap and Anderson localization of light in correlated disordered media, Physical Review Research **4**, 033246 (2022).

[4] L. S. Froufe-Pérez, G. J. Aubry, F. Scheffold, and S. Magkiriadou, Bandgap fluctuations and robustness in two-dimensional hyperuniform dielectric materials, Optics Express **31**, 18509 (2023).

[5] A. H. Barnett, J. Magland, and L. Af Klinteberg, A Parallel nonuniform fast Fourier transform library based on an "exponential of semicircle" kernel, SIAM Journal on Scientific Computing **48**, C479 (2019).

[6] A. H. Barnett, Aliasing error of the $\exp(\sqrt{1-z^2})$ kernel in the nonuniform fast Fourier transform, Applied and Computational Harmonic Analysis **51**, 1 (2021).

[7] S. Torquato, G. Zhang, and F. H. Stillinger, Ensemble theory for stealthy hyperuniform disordered ground states, Physical Review X **5**, 021020 (2015).

[8] O. U. Uche, F. H. Stillinger, and S. Torquato, Constraints on collective density variables: Two dimensions, Physical Review E - Statistical Physics, Plasmas, Fluids, and Related Interdisciplinary Topics **70**, 046122 (2004).

[9] O. U. Uche, S. Torquato, and F. H. Stillinger, Collective coordinate control of density distributions, Physical Review E - Statistical, Nonlinear, and Soft Matter Physics **74**, 031104 (2006).

[10] P. K. Morse, J. Kim, P. J. Steinhardt, and S. Torquato, Generating large disordered stealthy hyperuniform systems with ultra-high accuracy to determine their physical properties, Physical Review Research **5**, 033190 (2023).

[11] L. S. Froufe-Pérez, M. Engel, P. F. Damasceno, N. Muller, J. Haberko, S. C. Glotzer, and F. Scheffold, Role of Short-Range Order and Hyperuniformity in the Formation of Band Gaps in Disordered Photonic Materials, Physical Review Letters **117**, 1 (2016).

[12] S. F. Liew, J. K. Yang, H. Noh, C. F. Schreck, E. R. Dufresne, C. S. O'Hern, and H. Cao, Photonic band gaps in three-dimensional network structures with short-range order, Physical Review A - Atomic, Molecular, and Optical Physics **84**, 063818 (2011).

[13] S. R. Sellers, W. Man, S. Sahba, and M. Florescu, Local self-uniformity in photonic networks, Nature Communications **8**, 14439 (2017).

[14] G. Friedel, Sur la diffraction des rayons Röntgen par les cristaux, Bulletin de la Société française de Minéralogie **36**, 211 (1913).

[15] D. Schwarzenbach, *Crystallography* (John Wiley & Sons, 1996).

[16] A. Jagannathan and M. Duneau, The eight-fold way for optical quasicrystals, The European Physical Journal B **87**, 149 (2014).

[17] Y. F. Chen, H. C. Liang, Y. C. Lin, Y. S. Tzeng, K. W. Su, and K. F. Huang, Generation of optical crystals and quasicrystal beams : Kaleidoscopic patterns and phase singularity, Physical Review A **83**, 053813 (2011).

[18] P.-H. Tuan and L.-Q. Huang, Optical vector fields with kaleidoscopic quasicrystal structures by multiple beam interference, Optics Express **31**, 33077 (2023).

[19] M.E.Zoorob, M.D.B.Charlton, G.J.Parker, J.J.Baumberg, and M.C.Netti, Complete photonic bandgaps in 12-fold symmetric quasicrystals, Nature **404**, 740 (2000).

[20] S. M. Lubin, W. Zhou, A. J. Hryn, M. D. Huntington, and T. W. Odom, High-rotational symmetry lattices fabricated by Moiré nanolithography, Nano Letters **12**, 4948 (2012).

[21] D. C. Liu and J. Nocedal, On the limited memory BFGS method for large-scale optimization, Mathematical Programming **45**, 503 (1989).

[22] J. Nocedal and S. Wright, *Numerical Optimization* (Springer, 1999).

[23] D. J. Rosenkrantz, R. E. Stearns, and P. M. I. Lewis, An Analysis of Several Heuristics for the Traveling Salesman Problem, SIAM Journal on Computing **6**, 563 (1977).

[24] S. Mallat, *A Wavelet Tour of Signal Processing* (Academic Press, 1999).

[25] J.-P. Hansen and I. R. McDonald, *Theory of simple liquids* (Elsevier Academic Press, 2006).

[26] P. J. Steinhardt, D. R. Nelson, and M. Ronchetti, Bond-orientational order in liquids and glasses, Physical Review B **28**, 784 (1983).

[27] D. R. Nelson and B. I. Halperin, Dislocation-mediated melting in two dimensions, Physical Review B **19**, 2457 (1979).

[28] J. Kim and S. Torquato, Effect of imperfections on the hyperuniformity of many-body systems, Physical Review B **054105**, 054105 (2018).

[29] M. A. Klatt, J. Kim, and S. Torquato, Cloaking the underlying long-range order of randomly perturbed lattices, Physical Review E **101**, 032118 (2020).

[30] B. Guiselin, G. Tarjus, and L. Berthier, Static self-induced heterogeneity in glass-forming liquids: Overlap as a microscope, The Journal of Chemical Physics **156**, 194503 (2022).

[31] M. Florescu, S. Torquato, and P. J. Steinhardt, Designer disordered materials with large, complete photonic band gaps, Proceedings of the National Academy of Sciences of the United States of America **106**, 20658 (2009).

[32] S. E. Skipetrov, Finite-size scaling analysis of localization transition for scalar waves in a three-dimensional ensemble of resonant point scatterers, Physical Review B **94**, 064202 (2016).

[33] S. E. Skipetrov, Finite-size scaling of the density of states inside band gaps of ideal and disordered photonic crystals, European Physical Journal B **93**, 70 (2020).

[34] M. Morse, Philip and H. Feshbach, *Methods of Theoretical Physics: Part II* (McGraw-Hill series in fundamentals of physics, 1953).

[35] J. D. Jackson, *Classical Electrodynamics* (Wiley, 1999).

[36] R. Carminati and J. C. Schotland, *Principles of Scattering and Transport of Light* (Cambridge University Press, 2021).

[37] E. N. Economou, *Springer Series in Solid-state Sciences* (Springer, Berlin, 2006).

[38] M. I. Mishchenko, J. W. Hovenier, L. D. Travis, W. J. Wiscombe, C. V. M. van der Mee, I. R. Ciric, F. R. Cooray, B. T. Draine, A. Macke, P. Yang, K. N. Liou, K. A. Fuller, D. W. Mackowski, P. Chýlek, G. Videen, D. J. W. Geldart, J. S. Dobbie, H. C. W. Tso, K. Muinonen, B. Å. S. Gustafson, K. Sassen, Y. Takano, K. Aydin, J. L. Haferman, M. S. Quinby-Hunt, P. G. Hull, A. J. Hunt, K. Lumme, A. G. Hoekstra, and P. M. A. Sloot, *Light Scattering by Nonspherical Particles: Theory, Measurements, and Applications*, edited by M. I. Mishchenko, J. W. Hovenier, and L. D. Travis (Academic Press, 2000).

[39] M. Lax, Multiple Scattering of Waves, Reviews of Modern Physics **23**, 287 (1951).

[40] M. Lax, Multiple scattering of waves. II. the effective field in dense systems, Physical Review **85**, 621 (1952).

[41] O. Leseur, R. Pierrat, J. J. Sáenz, and R. Carminati, Probing two-dimensional Anderson localization without statistics, Physical Review A - Atomic, Molecular, and Optical Physics **90**, 053827 (2014).

[42] O. Leseur, R. Pierrat, and R. Carminati, High-density hyperuniform materials can be transparent, Optica **3**, 763 (2016).

[43] L. Dal Negro, R. Wang, and F. A. Pinheiro, Structural and spectral properties of deterministic aperiodic optical structures, Crystals **6**, 38 (2016).

[44] R. Pierrat and R. Carminati, Spontaneous decay rate of a dipole emitter in a strongly scattering disordered environment, Physical Review A - Atomic, Molecular, and Optical Physics **81**, 063802 (2010).

[45] O. Leseur, *Diffusion, localisation et absorption de lumière en milieux désordonnés. Impact des corrélations spatiales du désordre.*, Phd thesis, Université Pierre et Marie Curie (2016).

[46] S. E. Skipetrov and I. M. Sokolov, Absence of anderson localization of light in a random ensemble of point scatterers, Physical Review Letters **112**, 023905 (2014).

[47] W. Man, M. Florescu, K. Matsuyama, P. Yadak, G. Nahal, S. Hashemizad, E. Williamson, P. Steinhardt, S. Torquato, and P. Chaikin, Photonic band gap in isotropic hyperuniform disordered solids with low dielectric contrast, Optics Express **21**, 19972 (2013).

[48] S. Tsitrin, E. P. Williamson, T. Amoah, G. Nahal, H. L. Chan, M. Florescu, and W. Man, Unfolding the band structure of non-crystalline photonic band gap materials, Scientific Reports **5**, 13301 (2015).

[49] V. Prosentsov and A. Lagendijk, The local density of states in finite size photonic structures, small particles approach, Photonics and Nanostructures - Fundamentals and Applications **5**, 189 (2007).

[50] A. Cazé, R. Pierrat, and R. Carminati, Strong coupling to two-dimensional Anderson localized modes, Physical Review Letters **111**, 053901 (2013).

[51] M. G. Silveirinha, Nonlocal homogenization model for a periodic array of -negative rods, Physical Review E - Statistical, Nonlinear, and Soft Matter Physics **73**, 046612 (2006).

[52] S. Johnson and J. Joannopoulos, Block-iterative frequency-domain methods for Maxwell's equations in a planewave basis, Optics Express **8**, 173 (2001).

[53] M. A. Klatt, P. J. Steinhardt, and S. Torquato, Wave propagation and band tails of two-dimensional disordered systems in the thermodynamic limit, Proceedings of the National Academy of Sciences of the United States of America **119**, e2213633119 (2022).

[54] A. F. Oskooi, D. Roundy, M. Ibanescu, P. Bermel, J. D. Joannopoulos, and S. G. Johnson, Meep: A flexible free-software package for electromagnetic simulations by the FDTD method, Computer Physics Communications **181**, 687 (2010).